THE UNIVERSITY OF CAPE TOWN

MASTERS THESIS

A Proper Orthogonal Decomposition-based Inverse Material Parameter Optimization Method with Applications to Cardiac Mechanics

Author:
Kamlin MOODLEY

Supervisor:
Dr. Sebastian SKATULLA

A thesis submitted in fulfillment of the requirements for the degree of Master of Engineering in the field of Structural Engineering

in the

Computational Continuum Mechanics Group
Department of Civil Engineering

August 2016

Declaration of Authorship

I, Kamlin MOODLEY, declare that this thesis titled, "A Proper Orthogonal Decomposition-based Inverse Material Parameter Optimization Method with Applications to Cardiac Mechanics" and the work presented in it are my own. I confirm that:

- This work was done wholly or mainly while in candidature for a research degree at this University.
- Where any part of this thesis has previously been submitted for a degree or any other qualification at this University or any other institution, this has been clearly stated.
- Where I have consulted the published work of others, this is always clearly attributed.
- Where I have quoted from the work of others, the source is always given. With the exception of such quotations, this thesis is entirely my own work.
- I have acknowledged all main sources of help.
- I know the meaning of plagiarism and declare that all the work in the document, except for that which is properly acknowledged, is my own.

Signed: Signed by candidate

Signature Removed

Date: 31 August 2016

"If something is important enough, even if the odds are against you, you should still do it."

Elon Musk

THE UNIVERSITY OF CAPE TOWN

Abstract

Faculty of Engineering and the Built Environment
Department of Civil Engineering

Master of Engineering in the field of Structural Engineering

A Proper Orthogonal Decomposition-based Inverse Material Parameter Optimization Method with Applications to Cardiac Mechanics

by Kamlin MOODLEY

We are currently witnessing the advent of a revolutionary new tool for biomedical research. Complex mathematical models of "living cells" are being arranged into representative tissue assemblies and utilized to produce models of integrated tissue and organ function. This enables more sophisticated simulation tools that allows for greater insight into disease and guide the development of modern therapies. The development of realistic computer models of mechanical behaviour for soft biological tissues, such as cardiac tissue, is dependent on the formulation of appropriate constitutive laws and accurate identification of their material parameters.

The main focus of this contribution is to investigate a Proper Orthogonal Decomposition with Interpolation (PODI) based method for inverse material parameter optimization in the field of cardiac mechanics. Material parameters are calibrated for a left ventricular and bi-ventricular human heart model during the diastolic filling phase. The calibration method combines a MATLAB-based Levenberg Marquardt algorithm with the in-house PODI-based software ORION. The calibration results are then compared against the full-order solution which is obtained using an in-house code based on the element-free Galerkin method, which is assumed to be the exact solution. The results obtained from this novel calibration method demonstrate that PODI provides the means to drastically reduce computation time but at the same time maintain a similar level of accuracy as provided by the conventional approach.

Keywords: *Cardiac Mechanics, Heart Modelling, Computational Mechanics, Reduced Order Method, Proper Orthogonal Decomposition with Interpolation, Inverse Modelling, Meshfree Methods.*

Acknowledgements

It would not have been possible to write this thesis without the help and support of the kind people around me. In particular, I would like to thank and express my appreciation to the following people.

My supervisor, Dr Sebastian Skatulla, for providing the interesting topic and his strong guidance, patience and support during the research. His sharp editorial eye and constructive criticism helped me to do my very best in writing this thesis.

Mr Ritesh Rama, for his assistance in helping me understand the concepts within this research, in particular the Levenberg Marquardt algorithm. He has also been a very good friend to me over the duration of my study, and was always available for advice and guidance.

The resources that were provided by the University of Cape Town and the Centre for High Performance Computing (CHPC). Computations were performed using facilities provided by the University of Cape Town's ICTS High Performance Computing team: http://hpc.uct.ac.za

My parents and siblings, who have always provided me with unconditional support, selfless love and belief in my abilities. I would like to thank my parents for providing me with the solid educational foundation which I now use to pursue my engineering career and life ideas. A special thanks to my sister Seranya for her assistance with some of the graphical editing for the figures within this work.

My charming partner Mayuri for her emotional support, understanding and patience with me during the last stages of my academic work.

Contents

List of Figures

List of Tables

List of Abbreviations

A-V	Atrioventricular
BV	Bi-ventricle
CCM	Computational Continuum Mechanics Group
CHPC	Centre for High Performance Computing
CVD	Cardiovascular disease
EDV	End diastolic volume
EFG	Element-free Galerkin method
ESV	End systolic volume
FEM	Finite Element method
KLD	Karhunen-Loéve Decomposition
LM	Levenberg-Marquardt
LV	Left ventricle
MLS	Moving least squares
MRI	Magnetic resonance imaging
PCA	Principal Component Analysis
PI	Performance Index
POD	Proper Orthogonal Decomposition
PODI	Proper Orthogonal Decomposition with Interpolation
POM	Proper Orthogonal Mode
POV	Proper Orthogonal Value
ROM	Reduced order method
RV	Right ventricle
SVD	Single value decomposition
WHO	World Health Organization

Dedicated to my mother and father for their love and support..

Chapter 1

Introduction

Cardiovascular diseases (CVD) are the number one cause of death globally with more people dying annually from CVDs than from any other cause according to the American Heart Association [47] and the World Health Organization (WHO) [46]. It is estimated that by 2030 more than 23 million people will die annually from CVDs [46] and that Europe alone spends about 196 € billion per year on heart related medical treatment [48]. A dramatic increase in CVD incidences is expected in Africa, in conjunction with improvement of economic wealth and social environment and the emergence of obesity, diabetes and uncontrolled hypertension [68]. Thus there is a vital importance for improved medical treatment methods for the human heart and to decrease the costs of our ageing society.

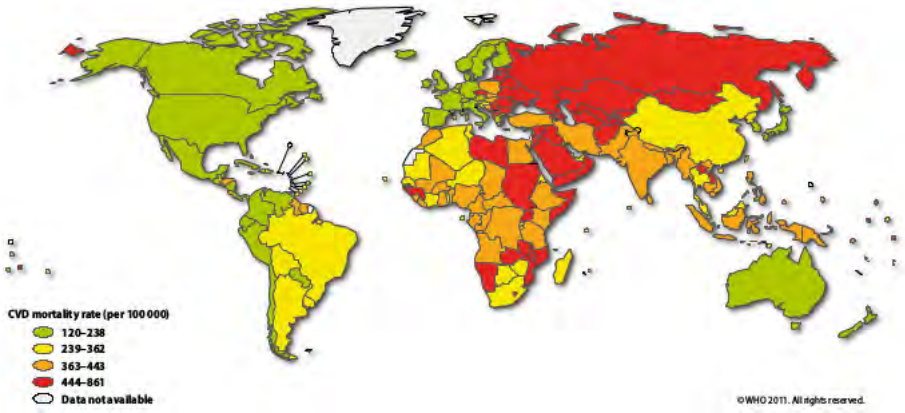

FIGURE 1.1: World map showing the global distribution of CVD mortality rates in males (age standardized, per 100,000) [46]

The heart is the life-giving, ever-beating muscle in a humans chest. The primary function of the heart is to pump blood through the arteries, capillaries, and veins which in turn ensure circulation of blood through the body. This occurs in a cyclic manner by diastolic filling and systolic contraction of the heart. The physics of the heart and other organs are complex. The geometry is often irregular and three dimensional, the structure is non-homogeneous and boundary conditions are time-varying. Constitutive properties and kinematics are typically non-linear and time-dependent.

Beyond mechanical responses, fundamental physiological functions include electrical, chemical, thermal and transport processes in cells and tissues. Each function may be based on more than one constitutive model. Therefore, computational methods are needed to realistically model many of these diverse and multidisciplinary processes encountered in biomechanics and tissue engineering.

The behaviour of myocardial tissue has been a major research focus for clinicians, physiologists, engineers and physical scientists who have sought to develop mathematical models to characterize cardiac mechanics. Structurally based models are usually based on in-vitro measurements of anatomy, tissue architecture and material properties. Their results must be validated with measurements from experiments. This iteration between model and experiment also provides the opportunity for numerical hypothesis testing and in-vivo constitutive parameter estimation. Once validated, the computational models have multidisciplinary applications to problems in medicine, surgery and bioengineering like diagnostic imaging, surgical planning and intervention, medical therapy, and biomedical engineering design for tissue engineering or medical devices [75]. Computational models can also be used to obtain a better understanding of how myocardial infarction affects cardiac function and are therefore potentially useful in the design of suitable therapeutic treatments.

1.1 Computational cardiac modelling

Modelling the mechanical behaviour of the heart has been a scientific endeavour for the last 30 years. There has been increasing interest in the last decade as progress in biology, physics and computer technology made it possible. Different models over time have been introduced and have either been successfully developed or discarded for more accurate or efficient alternatives. What was originally modelled as an elastic or visco-elastic material, lacked the mechanical influences of the complex structure to accurately describe myocardium tissue [57]. Specifically over the last 15 years, models have introduced phenomenological properties as a means to overcome the complex structure on a macro and micro scale. A problem to this approach is the shortage in experimental data suitable for detailed parameter estimation [57].

The following outlines the various model developments for passive material behaviour of myocardial tissue, starting with the first published attempts and concluding with the most recent, relevant and sophisticated

formulations published in the last few years.

Yuan-Cheng Fung is credited in the literature [25] [58] for being one of the first to describe a constitutive relationship for soft tissue behaviour. The interested reader should peruse the papers by Fung in 1967 [15] and in 1973 [14], which represent early efforts to place soft-tissue biomechanics within this framework of finite elasticity. What was initially proposed as a linear isotropic strain energy function was later developed as a quadratic and then an exponential description. The first invariant based constitutive model is credited to Humphrey and Yin [26]. The strain energy function introduced an exponential "fibre specific" term to account for the material anisotropy. The early developments of Fung-type strain energy functions were limited to describing the soft tissue as transversely isotropic [25].

Costa et al. [5] extended the formulation of Fung to an orthotropic formulation by introducing a fibre specific coordinate system and specifying principle material stiffness along the fibre, sheet and normal directions. The orthotropic formulation has varied slightly over time with minor modifications being introduced. Common formulations include those presented in Usyk et al. [74], Kerckhoffs [31], Holzapfel and Ogden [22] among others.

Over the last 10 years, significant progress has been made to achieve larger emphasis on the micro structure with multi-scale modelling. Smith et al. [66] introduced one of the first multi-scale models, by including cellular considerations for calculating the global active tension during contraction. Hussan et al. [27] includes micro mechanical contributions from the myocytes, modelling them as cylinders with mechanical degrees of freedom corresponding to twist, bend and splay.

With regards to experimental mechanical testing of cardiac specimens, Dokos et al. [8] demonstrated with shearing tests on 6 pig hearts that myocardial tissue exhibits a non-elastic response, anisotropy, strain softening and exhibits a laminar structure. The recent results in Sommer et al. [67] confirmed these findings for human left ventricle (LV) myocardial tissue subjected to quasi-static and dynamic multiaxial loading.

1.2 Inverse methods for material parameter identification

The development of realistic computer models of the mechanical behaviour for cardiac tissues is dependent on the formulation of appropriate constitutive laws and accurate identification of their material parameters. These material parameters are usually obtained from experimental mechanical testing, such as tension or shear tests, of the cardiac tissue. However, the availability of such experimental data suitable for the calibration of cardiac tissue is quite limited [57] [67] and it is not feasible to obtain patient-specific material parameters from experimental testing. With the evolution and improvements in computing power, a new technique has come about for the purpose of material parameter estimation. These methods make use of a branch of mathematics known as inverse problems. It is important to note that inverse methods still rely on experimental data for the initial material parameter calibration.

Parameter estimation is the process of fitting a mathematical model to experimental data to determine unknown parameters of the model. The parameters are chosen so that the output of the model match, to a certain degree, the experimental data. To do this, parameter estimation require inverse problem methodology. Inverse problems can be described as problems which may be interpreted as finding the cause of a given effect [17]. Avril et al. [1] describe various inverse methods for material parameter identification, namely the finite element model updating method (FEMU), the constitutive equation gap method (CEGM), the virtual fields method (VFM), the equilibrium gap method (EGM) and the reciprocity gap method (RGM).

This research relies on updating methods of inverse modelling. This involves the computation of simulated fields (such as strain or displacement) numerically using initial estimates for material parameters as defined in the particular constitutive law chosen. The actual constitutive material parameters are iteratively identified by minimizing a cost function, which compares available data measurements from experimental testing, to the corresponding results from the numerical simulation. The advantage of this method is that full-field measurements are useful, but not necessarily required. Fewer measurements distributed across the volume of interest are necessary.

Recently, Dubuis et al. [10] employed such methods to calibrate material parameters for soft tissues of the human leg. This was based on a Neo-Hookean constitutive model and used resultant displacements from MRI images, at various cross sectional heights of the leg. In terms of cardiac mechanics applications, Sun et al. [70] calibrated the mechanical response of bioprosthetic heart valves using biomaterials. This was characterized by a Fung-type constitutive model using in-plane shear data from biaxial testing. More recently, work by Kural et al. [33] involved identification of passive nonlinear elastic material parameters which characterized the behaviour of diseased human coronary and carotid arteries using planar biaxial testing.

Material parameter identification via an inverse approach, usually involves the use of an optimization algorithm [10]. Optimization techniques are generally classified as either local, typically gradient based, or global, typically non-gradient based algorithms. As indicated by the name, gradient-based optimization techniques make use of gradient information to find an optimum solution. Gradient-based techniques are popular because they are efficient, they can solve problems with large numbers of design variables, and they typically require little problem-specific parameter tuning [76]. These algorithms, however, also have several drawbacks which include that they can only locate a local optimum, have difficulty solving discrete optimization problems, are complex algorithms that are difficult to implement efficiently, and they may be susceptible to numerical noise [76]. Examples of gradient-based optimizers include Steepest descent, Gauss-Newton and the Levenberg-Marquardt algorithms. Non-gradient based algorithms tend to display slower convergence towards a parameter set that minimizes a cost function and this is usually attributed to the fact that a large initial population size of different parameter sets is required [76] [11]. These optimizers are reputed to be more adept at handling noisy experimental data, than gradient based optimizers and are also more efficient means of finding a global minima in a search space [76] [11]. Examples of non-gradient based algorithms include Genetic Search, Particle Swarm algorithms, Powell's method and the Nelder-Mead simplex algorithm. In this research, a gradient based optimizer based on the Levenberg-Marquardt algorithm is used in order to obtain desired material parameters. This choice is guided by the fact that the algorithm is robust and devoted to non-linear least squares curve fitting applications [42] [16] [55] [73].

The Levenberg-Marquardt algorithm can be traced back to the work by Levenberg in 1944 [37] and Marquardt in 1963 [44]. Various methods for constrained optimization using the Levenberg-Marquardt algorithm have

been presented in the literature of Guyon and Riche [19] and Kanzowa, Yamashitab, and Fukushimab [28], from which there appears to be three different variations. Kanzowa, Yamashitab, and Fukushimab [28], explored the first two variations for constrained optimization using the Levenberg-Marquardt algorithm. The first of these approaches solves a strictly convex minimization problem at each iteration. Whereas the second method, which is referred to as a projected Levenberg-Marquardt algorithm, only solves one equation system at each iteration. Both methods have been shown to converge near quadratically under an error bound assumption and can be globalized in an easy manner [28]. The last method was employed by Guyon and Riche [19] and proposes that parameter constraints are handled by checking the Kuhn and Tucker condition of the constrained problem. This research will make use of the method employed by Guyon and Riche [19].

1.3 Reduced order method

A reduced order method (ROM) can be thought of as a computationally inexpensive mathematical representation that offers the potential for near real-time analysis. A ROM can be used to decrease the number of equations that need to be solved in the Finite Element method. The main objective behind this method is usually to accelerate the calculation process as the reduced system of equations can now be computationally solved more easily. This is achieved by compressing the whole system to such a point that accuracy is not excessively impacted and that the general behaviour of the problem (for e.g the mechanics) is preserved. One widely used ROM is called the Proper Orthogonal Decomposition (POD).

POD can be described as a powerful and elegant method for data analysis aimed at obtaining low-dimensional approximate values of a high-dimensional process [4], [39]. The POD method was developed by several people, Holmes, Lumley, and Berkooz [21] traced the idea of the POD back to independent investigations by Kosambi (1943) [32], Loéve (1945) [41], Karhunen (1946) [29], Pougachev (1953) [52] and Obukhov (1954) [51]. The POD has been used to obtain approximate, low-dimensional descriptions of turbulent fluid flows [21], structural vibrations [7] [13], hypersonic aerothermoelastics [12] or in damage detection [56], to name a few applications. It has also been extensively used in image processing, signal analysis and data compression [4]. For further details on POD, the reader is encouraged to read Holmes, Lumley, and Berkooz [21](Chapter 3).

Holmes, Lumley, and Berkooz [21] suggests that the properties of POD make it the preferred basis to use in various applications and that the most striking property being its optimality. It provides the most efficient way of capturing the dominant components of an infinite-dimensional process with only finitely many, and often surprisingly few, "modes". POD yields basis functions which are commonly called empirical eigenfunctions, empirical basis functions, empirical orthogonal functions, proper orthogonal modes, or simply basis vectors. The POD basically extracts information from a predefined set of data, obtained from a set of experiments or simulated models, using statistical methods. One of the aims of this research is to create the predefined set of data from simulated models.

The POD is also known as Principal Component Analysis (PCA), the Karhunen-Loéve Decomposition (KLD), and the single value decomposition (SVD) [39]. Even though each of them have different derivations, Wu et al. [80] showed the equivalence between each of the methods and how they can all produce the same solution.

This research will use the Proper Orthogonal Decomposition with Interpolation (PODI) method which is a particular variant of POD.

1.4 Thesis motivation, aims and objectives

There are various fields in medicine and biomedical engineering where accurate computational models of the human heart are needed. Such computational models help to better understand pathological changes due to biomechanical factors and to improve clinical diagnostics, therapeutic interventions, material design for tissue engineering or drug development and medical devices such as pacemakers and heart valve implants. The range of possible applications is huge.

In general it is difficult to measure the mechanical properties of soft tissue materials directly. Some kind of inverse approach is needed, where an experiment has to be simulated and the material parameters are adjusted until the model matches the experiment. But even with this approach the presence of a non-linear system of ordinary and partial differential equations are difficult to solve for and therefore require a lot of computational power which can be extremely expensive. In [34] and [49] it has been found that computational resources can take up to several weeks with a single core processor and a very course mesh of the heart. Models with finer meshes are generally prepared to run on large supercomputers.

The application of this approach is therefore not practical in the clinical field where fast responsive models are required which can run on common desktop or laptop machines. A solution to this problem is to create a cardiac-mechanics database of pre-computed full-heart model simulations and use a PODI-based model reduction method to drastically reduce the time required for material parameter optimization on an ordinary desktop machine.

Motivated by the short term goal of constructing realistic myocardial models capable of capturing the mechanics of the heart as well as aiding the long term goal of improving methods of medical treatment and quality of life for people suffering from heart diseases this work provides a research contribution towards the development of more accurate computational simulations to better understand the fundamental ventricular mechanics of the human heart. The aim of this research is to investigate the suitability of PODI for the purpose of inverse material parameter optimization in the field of cardiac mechanics. This will be done by coupling PODI with the Levenberg Marquardt parameter optimization method. These results will be compared against the full-order solution which is obtained using an in-house code SESKA.

The cardiac mechanics research that will be presented in this work, forms part of an ongoing effort by the Computational Continuum Mechanics Group (CCM), at the University of Cape Town, to understand and quantify the behaviour of the human heart.

1.5 Organization of Thesis

In Chapter 2 the fundamentals of computational mechanics used in cardiac mechanics are reviewed. An outline to classical continuum mechanics is provided. The kinematic measures used to describe deformation and the stress measures needed to relate forces to deformation are introduced. The constitutive laws for a hyperelastic material are introduced to describe materials with isotropic, transversely isotropic and orthotropic properties. The EFG method is briefly described, followed by the variational formulation and assembly of the discrete set of equations.

In Chapter 3 the physiology of the heart is reviewed. The morphology, fibre orientation and cardiac cycle of the heart are discussed. The passive mechanics of the heart is also considered.

Chapter 4 provides an outline on reduced order methods and introduces the POD and PODI methods. PODI makes use of the moving least squares (MLS) concept, so this is also presented.

Chapter 5 outlines the concept of inverse material parameter identification. Furthermore, the Levenberg-Marquardt algorithm is presented to obtain material parameters.

In Chapter 6 the model development for the left ventricle (LV) and biventricle (BV) models used for the simulations of the cardiac function in this dissertation is described.

In Chapter 7 the results are presented for diastolic filling of the LV and BV models.

In Chapter 8 the key results are summarised and their significance discussed. The section closes with comments on potential future investigations.

Chapter 2

Computational mechanics

The constituents of the heart require a continuum mechanics based approach to the modelling of their mechanical behaviour. This chapter will therefore start with presenting the reader to the fundamental principles related to non-linear continuum mechanics. Thereafter, the remaining sections in this chapter will present the constitutive laws, computational mechanics and the key principles required to model and calculate the behaviour of the human heart.

2.1 Introduction to continuum mechanics

Continuum mechanics is a branch of mechanics that deals with the kinematics and mechanical behaviour of deformable materials modelled as a continuous media, as opposed to discrete particles. Continuum mechanics principles are vital for the analysis and study of cardiac mechanics.

As mentioned previously, the fundamental assumption in continuum mechanics assumes the material exists as a continuum, meaning the matter in the body is continuously distributed and fills the entire region of space it occupies. Additionally it is asserted that the matter may be divided indefinitely into smaller and smaller portions, each of which retains all of the physical properties of the parent body.

For a detailed treatment on continuum mechanics the reader is referred to the book by Lai, Rubin, and Krempl [35].

2.2 Kinematics

Consider a body, $\mathcal{B}$, in a three dimensional Euclidean vector space characterized as the reference configuration, which is the undeformed configuration. $\mathcal{B}$ is parametrized by the Cartesian coordinates X_1, X_2 and X_3, where the associated basis vectors are denoted by $\mathbf{e}_1$, $\mathbf{e}_2$ and $\mathbf{e}_3$, respectively. After

being subjected to certain boundary conditions, the body at time t, in its deformed state (or current configuration), is referred to as $\mathcal{B}_t$. To describe the transformation from the reference to the current configuration, a non linear deformation mapping, $\phi : \mathcal{B} \rightarrow \mathcal{B}_t$, is introduced, enabling one to define the relation of a material point in the reference configuration, $\mathbf{X} \in \mathcal{B}$, to that in the current configuration $\mathbf{x} \in \mathcal{B}_t$ as

$$\mathbf{x} = \phi\left(\mathbf{X}, t\right). \tag{2.1}$$

The deformation gradient, $\mathbf{F}$, can be obtained as the gradient of ϕ_t. Next, the Jacobian, defined as the determinant of $\mathbf{F}$, can be related to the deformation mapping, ϕ_t, using

$$J = \det \mathbf{F} = \det\left(\text{Grad}\, \phi_t\right) \tag{2.2}$$

where $J > 0$. The operators with respect to the reference and current configuration are shown in the Table 2.1.

TABLE 2.1: Gradient and divergence operation in the reference and current configuration

Operator	Reference Configuration	Current Configuration
Gradient	$\text{Grad}(\bullet) = \boldsymbol{\nabla}(\bullet) = \frac{\partial}{\partial \mathbf{X}}(\bullet)$	$\text{grad}(\bullet) = \boldsymbol{\nabla}_t(\bullet) = \frac{\partial}{\partial \mathbf{x}}(\bullet)$
Divergence	$\text{Div}(\bullet) = \boldsymbol{\nabla} \cdot (\bullet) = \frac{\partial}{\partial \mathrm{X}_i}(\bullet) \cdot \mathbf{e}_i$	$\text{div}(\bullet) = \boldsymbol{\nabla}_t \cdot (\bullet) = \frac{\partial}{\partial \mathrm{x}_i}(\bullet) \cdot \mathbf{e}_i$

The displacement field is given by, $\mathbf{u}(\mathbf{X}, t) = \mathbf{x}(\mathbf{X}, t) - \mathbf{X}$. Hence, the deformation gradient, $\mathbf{F}$, can be formulated in terms of $\mathbf{u}(\mathbf{X}, t)$ as

$$\mathbf{F} = \mathbf{1} + \boldsymbol{\nabla}(\mathbf{u}(\mathbf{X}, t)). \tag{2.3}$$

Next, any change in time is termed the local rate of change expressed as

$$\frac{\partial}{\partial t}(\bullet). \tag{2.4}$$

and the overall time rate of change is

$$\frac{D}{Dt}(\bullet) = \frac{\partial}{\partial t}(\bullet) + \frac{\partial}{\partial x_i}(\bullet)\frac{dx_i}{dt}. \tag{2.5}$$

Consequently, the Jacobian, which defines the change of volumes from different configuration states, can also vary with respect to time according to

$$\dot{J} = J\, \text{div}\, \dot{\mathbf{x}}. \tag{2.6}$$

For the later usage, we also take into account that a surface element in the

reference configuration, dA, with its unit normal, $\mathbf{n}$, is related to its counterpart in the current configuration, da, with its unit normal, $\boldsymbol{\nu}$, via

$$\boldsymbol{\nu} da = \det(\mathbf{F})\mathbf{F}^{-\mathrm{T}}\mathbf{n} dA. \tag{2.7}$$

In addition, a volume element in the reference configuration, dV, is related to its counterpart in the current configuration, dv, by

$$dv = \det(\mathbf{F}) dV = J dV. \tag{2.8}$$

Next, the change in length of a line after deformation would require the difference between the length in the reference configuration, $d\mathbf{x}^2$ and that in the current configuration, $d\mathbf{X}^2$ and is computed as

$$d\mathbf{x}^2 - d\mathbf{X}^2 = (\mathbf{F}^{\mathrm{T}}\mathbf{F} - \mathbf{1}) : (d\mathbf{X} \otimes d\mathbf{X}). \tag{2.9}$$

Based on the above, the $right\ Cauchy - Green$ tensor is defined as

$$\mathbf{C} = \mathbf{F}^T\mathbf{F}. \tag{2.10}$$

Thus, the $Green$ strain tensor, which is symmetric in nature, can now be introduced as a function of $\mathbf{C}$ via

$$\mathbf{E} = \frac{1}{2}(\mathbf{C} - \mathbf{1}) = \frac{1}{2}(\mathbf{F}^T\mathbf{F} - \mathbf{1}). \tag{2.11}$$

The $right\ Cauchy - Green$ tensor can also be expressed in terms of the right stretch tensor, $\mathbf{U}$, as

$$\mathbf{C} = \mathbf{U}^2. \tag{2.12}$$

Finally, using the eigenvalues of $\mathbf{U}, \lambda_1, \lambda_2$ and λ_3, the scalar invariants of $\mathbf{C}$ are

$$I_1^{\mathrm{C}} = tr(\mathbf{C}) = \lambda_1^2 + \lambda_2^2 + \lambda_3^2, \tag{2.13}$$

$$I_2^{\mathrm{C}} = \frac{1}{2}\left[(tr\mathbf{C})^2 - tr(\mathbf{C}^2)\right] = \lambda_1^2\lambda_2^2 + \lambda_2^2\lambda_3^2 + \lambda_3^2\lambda_1^2, \tag{2.14}$$

$$I_3^{\mathrm{C}} = \det \mathbf{C} = \lambda_1^2\lambda_2^2\lambda_3^2. \tag{2.15}$$

2.3 Stress measures

Bodies subjected to forces will undergo deformation, resulting in a redistribution of forces throughout the body. Consider a body in the current configuration, $\mathcal{B}_t$, subjected to a body force, $\mathbf{b}_t$, and a surface traction, $\mathbf{t}^{(\boldsymbol{\nu})}$, which is the traction vector acting on a surface with a unit normal, $\boldsymbol{\nu}$. Then

the following relation holds;

$$\mathbf{t}^{(\boldsymbol{\nu})}(\mathbf{x},t) = \boldsymbol{\sigma}^{\mathrm{T}}(\mathbf{x},t)\boldsymbol{\nu}(\mathbf{x},t), \tag{2.16}$$

where $\boldsymbol{\sigma}(\mathbf{x},t)$ is defined as the $Cauchy$ stress tensor. Eq. (2.16) is known as $Cauchy's\ Theorem$. If the stress state of the same point in the reference configuration is to be found, then the element surface to be considered is dA, with unit normal of $\mathbf{n}$. Consequently, the traction vector is expressed as

$$\mathbf{t}^{(\mathbf{n})}(\mathbf{X},t) = \mathbf{P}(\mathbf{X},t)\mathbf{n}(\mathbf{X}), \tag{2.17}$$

with $\mathbf{P}$ being the $first\ Piola-Kirchhoff$ stress tensor. $\mathbf{P}$ relates stresses with forces in the current configuration as acting on areas in the reference configuration. Hence, the deformation gradient, $\mathbf{F}$, can be applied to map the forces to the reference configuration. In this case, the new stress tensor is defined as the $second\ Piola-Kirchhoff$ stress tensor $\mathbf{S}$ using the relation

$$\mathbf{P} = \mathbf{F}\mathbf{S}. \tag{2.18}$$

Using $\boldsymbol{\sigma}$ (the $Cauchy$ stress tensor), $\mathbf{P}$ can be defined differently, by first assuming that a force, $\mathbf{f}$, acting on da is no different to the one applied on dA, yielding,

$$d\mathbf{f} = \mathbf{P}\mathbf{n}\,dA = \boldsymbol{\sigma}^{\mathrm{T}}\boldsymbol{\nu}\,da = \boldsymbol{\sigma}^{\mathrm{T}}\det(\mathbf{F})\mathbf{F}^{-\mathrm{T}}\mathbf{n}\,dA. \tag{2.19}$$

Where, the first Piola-Kirchhoff stress can also be calculated from

$$\mathbf{P} = \det(\mathbf{F})\boldsymbol{\sigma}^{\mathrm{T}}\mathbf{F}^{-\mathrm{T}}. \tag{2.20}$$

2.4 Balance Law of Continuum Mechanics

The balance laws, also known as the conservation laws, are physical principles that must be satisfied for all material systems. If a body is subjected to perturbations of any form (e.g. force, temperature or magnetic field), then the following fundamental physical laws can be used to describe the behaviour of the body [45]:

- The law of *Conservation of Mass* ensures that there is no mass loss or gain when the body changes from the undeformed to the deformed configuration.
- The law of *Linear and Angular Momentum Conservation* defines the rate of change of linear and angular momentum over time, resulting in force and momentum.

- The law of *Energy Conservation* is related to the Principle law of Energy which states that energy can neither be created nor destroyed but can only change forms.

Each of these Balance Laws will now be presented in the sections which follow. The reader is referred to Capaldi [3] for a detailed treatment of the derivations of the integral and local forms of these laws.

2.4.1 Conservation of Mass

The mass m of a material continuum body, $\mathcal{B}_t$, at time t is given by

$$m = \int_{\mathcal{B}_t} \rho(\mathbf{x}, t) dv, \tag{2.21}$$

where, ρ is the density in the current configuration. The law of *Conservation of Mass*, states that the cumulative mass of a body, $\mathcal{B}_t$, is conserved with motion. This asserts that the derivative of Eq. (2.21) with respect to time is zero

$$\dot{m} = \frac{d}{dt} \int_{\mathcal{B}_t} \rho(\mathbf{x}, t) dv = \int_{\mathcal{B}_t} \{\dot{\rho}(\mathbf{x}, t) + \rho(\mathbf{x}, t) J \text{div} \dot{\mathbf{x}}\} dv = 0, \tag{2.22}$$

where the relations in Eq. (2.8) and Eq. (2.6) were used. Since $\mathcal{B}_t$ is arbitrary, the integrand in Eq. (2.22) must vanish, resulting in the so-called *continuity equation*, which in the Eulerian form is

$$\dot{\rho}(\mathbf{x}, t) + \rho(\mathbf{x}, t)\, J \text{div}\, \dot{\mathbf{x}} = 0. \tag{2.23}$$

The conservation of mass also states that the mass in the current and reference configurations are equal. Therefore,

$$m = \int_{\mathcal{B}_t} \rho(\mathbf{x}, t) dv = \int_{\mathcal{B}} \rho_0(\mathbf{X})\, dV, \tag{2.24}$$

where ρ_0 denotes the density of the material in the reference configuration. With Eq. (2.8) and recognizing that $\mathbf{x} = (\mathbf{X}, t)$, Eq. (2.21) can be expressed in Lagrangian form by

$$m = \int_{\mathcal{B}} \rho(\mathbf{X}, t) J dV, \tag{2.25}$$

and substituting Eq. (2.25) into the left-hand side of Eq. (2.24), we arrive at

$$\int_{\mathcal{B}} \{\rho(\mathbf{X}, t) J - \rho_0(\mathbf{X})\} dV = 0. \tag{2.26}$$

Since $\mathcal{B}$ is arbitrary, the integrand in Eq. (2.26) must vanish, yielding the Lagrangian or material form of the continuity equation, which is given by

$$\rho(\mathbf{X}, t)J = \rho_0(\mathbf{X}). \tag{2.27}$$

With $\dot{\rho_0} = 0$ we have

$$\frac{d}{dt}(\rho(\mathbf{X}, t)J) = 0, \tag{2.28}$$

which is a relation that is particularly useful in evaluating the material derivative of an integral over some product ρA,

$$\frac{d}{dt}\int_{\mathcal{B}_t} \rho(\mathbf{x}, t)\, A(\mathbf{x}, t)\, dv = \int_{\mathcal{B}_t} \rho(\mathbf{x}, t)\, \dot{A}(\mathbf{x}, t)\, dv, \tag{2.29}$$

where $A(\mathbf{x}, t)$ is a field of some property per unit mass.

2.4.2 Linear Momentum Conservation

If a body, $\mathcal{B}_t$, in the current configuration, is subjected to a body force, $\mathbf{b}_t$ and a surface traction, $\mathbf{t}^{(\boldsymbol{\nu})}$, is applied to a boundary surface, $\partial\mathcal{B}_t$, then the principle of linear momentum conservation states that the rate of change of linear momentum, is equal to the total resultant force acting on the body, which yields,

$$\frac{d}{dt}\int_{\mathcal{B}_t} \rho(\mathbf{x}, t)\dot{\mathbf{x}}dv = \int_{\partial\mathcal{B}_t} \mathbf{t}^{(\boldsymbol{\nu})}(\mathbf{x}, t)da + \int_{\partial\mathcal{B}_t} \mathbf{b}_t(\mathbf{x}, t)dv. \tag{2.30}$$

Introducing the *Cauchy stress* and making use of the *Gauss divergence theorem*, Eq. (2.30), is transformed into the global equation of motion, given by

$$\int_{\mathcal{B}_t} \{\rho(\mathbf{x}, t)\ddot{\mathbf{x}} - \mathrm{div}\boldsymbol{\sigma}^{\mathrm{T}} - \mathbf{b}_t(\mathbf{x}, t)\}dv = \mathbf{0}. \tag{2.31}$$

The local form of the equation of motion is obtained if one acknowledges that $\mathcal{B}_t$ is arbitrary, resulting in the relation

$$\mathrm{div}\boldsymbol{\sigma}^{\mathrm{T}} + \mathbf{b}_t(\mathbf{x}, t) = \rho(\mathbf{x}, t)\ddot{\mathbf{x}}. \tag{2.32}$$

For a constant velocity field, $\dot{\mathbf{x}}(\mathbf{x}, t)$, the acceleration field, $\ddot{\mathbf{x}}$, is zero, reducing Eq. (2.32) to the equilibrium equation, given by

$$\mathrm{div}\boldsymbol{\sigma}^{\mathrm{T}} + \mathbf{b}_t(\mathbf{x}, t) = \mathbf{0}. \tag{2.33}$$

The above steps can be repeated for quantities in the reference configuration, $\mathcal{B}$. The global equation of motion now becomes

$$\frac{d}{dt}\int_{\mathcal{B}} \rho_0\, \dot{\mathbf{x}}(\mathbf{X},t)dV = \int_{\partial\mathcal{B}} \mathbf{t}^{(\boldsymbol{\nu})}(\mathbf{X},t)dA + \int_{\partial\mathcal{B}} \mathbf{b}(\mathbf{X},t)dV, \tag{2.34}$$

where $\mathbf{b}$ is the body force in the reference configuration. With the elimination of the traction vector and applying the Gauss divergence theorem, Eq. (2.34) becomes

$$\int_{\mathcal{B}} \{\rho_0\, \ddot{\mathbf{x}}(\mathbf{X},t)dV - \mathrm{div}\mathbf{P} - \mathbf{b}(\mathbf{X},t)\}\, dV = \mathbf{0}. \tag{2.35}$$

Acknowledging that $\mathcal{B}$ is arbitrary, one can obtain the localized equation of motion, which shall now be called the *Lagrangian equation of motion*, as

$$\mathrm{div}\mathbf{P} + \mathbf{b}(\mathbf{X},t) = \rho_0 \ddot{\mathbf{x}}(\mathbf{X},t). \tag{2.36}$$

Finally, the *Lagrangian equilibrium equation* with constant velocity field is given by

$$\mathrm{div}\mathbf{P}(\mathbf{X},t) + \mathbf{b}(\mathbf{X},t) = \mathbf{0}. \tag{2.37}$$

2.4.3 Angular Momentum Conservation

The angular momentum is defined as the moment of the linear momentum with respect to some reference point. This point of reference is usually chosen to be the origin of some coordinate system.Thus, in the spatial or current configuration, the principle of angular momentum conservation is formulated as

$$\frac{d}{dt}\int_{\mathcal{B}_t} \mathbf{x}\times\rho(\mathbf{x},t)\dot{\mathbf{x}}dv = \int_{\partial\mathcal{B}_t} \mathbf{x}\times\mathbf{t}^{(\boldsymbol{\nu})}(\mathbf{x},t)da + \int_{\partial\mathcal{B}_t} \mathbf{x}\times\mathbf{b}_t(\mathbf{x},t)dv. \tag{2.38}$$

Normalising the integrands by taking the material derivative, using the *Cauchy stress tensor*, $\boldsymbol{\sigma}$, and applying the *Gauss divergence theorem*, we obtain that

$$\int_{\mathcal{B}_t} \{\mathbf{x}\times\rho(\mathbf{x},t)\ddot{\mathbf{x}} - \mathrm{div}(\mathbf{x}\times\boldsymbol{\sigma}^{\mathrm{T}}) - \mathbf{x}\times\mathbf{b}_t(\mathbf{x},t)\}\, dv = \mathbf{0}, \tag{2.39}$$

with

$$\mathrm{div}(\mathbf{x}\times\boldsymbol{\sigma}^{\mathrm{T}}) = \mathrm{grad}\,\mathbf{x}\times\boldsymbol{\sigma}^{\mathrm{T}} + \mathbf{x}\times\mathrm{div}(\boldsymbol{\sigma}^{\mathrm{T}}). \tag{2.40}$$

Simplifying the above, Eq. (2.39) is transformed to

$$\int_{\mathcal{B}_t} \{\mathbf{x} \times \rho(\mathbf{x},t)\ddot{\mathbf{x}} + \boldsymbol{\epsilon} : \boldsymbol{\sigma}^{\mathrm{T}} - \mathbf{x} \times \mathrm{div}\boldsymbol{\sigma}^{\mathrm{T}} - \mathbf{x} \times \mathbf{b}_t(\mathbf{x},t)\}\, dv = \mathbf{0}, \tag{2.41}$$

where $\boldsymbol{\epsilon} : \boldsymbol{\sigma}^{\mathrm{T}} = \epsilon_{ijk}\, \sigma_{lk}\, \boldsymbol{e}_i$ and ϵ_{ijk} denotes the Levi-Civita symbol. Since $\mathcal{B}_t$ in Eq. (2.41) is arbitrary we get that

$$\mathbf{x} \times \rho(\mathbf{x},t)\ddot{\mathbf{x}} - \mathbf{x} \times \mathrm{div}\boldsymbol{\sigma}^{\mathrm{T}} - \mathbf{x} \times \mathbf{b}_t(\mathbf{x},t) + \boldsymbol{\epsilon} : \boldsymbol{\sigma}^{\mathrm{T}} = \mathbf{0}. \tag{2.42}$$

Then, with Eq. (2.32) we have that

$$\boldsymbol{\epsilon} : \boldsymbol{\sigma}^{\mathrm{T}} = \mathbf{0}. \tag{2.43}$$

The above equation demonstrates the symmetric properties of the *Cauchy stress tensor*. Consequently, the Lagrangian form of the above equations, can now be formulated. Firstly, the principle of angular momentum conservation can be reformulated as

$$\begin{aligned} &\frac{d}{dt}\int_{\mathcal{B}} \mathbf{x}(\mathbf{X},t) \times \rho_0\, \dot{\mathbf{x}}(\mathbf{X},t) dV = \\ &\qquad \int_{\partial\mathcal{B}} \mathbf{x}(\mathbf{X},t) \times \mathbf{t}^{(\mathbf{n})}(\mathbf{X},t) dA + \int_{\partial\mathcal{B}} \mathbf{x}(\mathbf{X},t) \times \mathbf{b}(\mathbf{X},t) dV. \end{aligned} \tag{2.44}$$

Applying the divergence theorem we get that

$$\int_{\mathcal{B}} \{\mathbf{x}(\mathbf{X},t) \times \rho_0\, \ddot{\mathbf{x}}(\mathbf{X},t) - \mathrm{div}(\mathbf{x}(\mathbf{X},t) \times \mathbf{P}) - \mathbf{x}(\mathbf{X},t) \times \mathbf{b}(\mathbf{X},t)\}\, dV = \mathbf{0}. \tag{2.45}$$

Consequently, using Eq. (2.36)

$$\int_{\mathcal{B}} \mathbf{F} \times \mathbf{P}\, dV = \mathbf{0}, \tag{2.46}$$

and since the integrand is arbitrary,

$$\mathbf{F} \times \mathbf{P} = \boldsymbol{\epsilon} : \left(\mathbf{F}\mathbf{P}^{\mathrm{T}}\right) = \mathbf{0}. \tag{2.47}$$

Thus, the symmetric nature of $\mathbf{F}\mathbf{P}^{\mathrm{T}}$ is demonstrated, which means that

$$\mathbf{F}\mathbf{P}^{\mathrm{T}} = \mathbf{P}\mathbf{F}^{\mathrm{T}}. \tag{2.48}$$

Finally, since $\mathbf{S} = \mathbf{P}\mathbf{F}^{\mathrm{T}}$, it follows that the *second Piola-Kirchhoff stress tensor* is also symmetric

$$\mathbf{S}^{\mathbf{T}} = \mathbf{S}. \tag{2.49}$$

2.5 Constitutive laws

In physics and engineering, a constitutive law is a relation between two physical quantities that is specific to a material and approximates the response of that material to an external stimuli, usually applied fields or forces. In this research we will consider the constitutive laws which allow us to describe the relationship between stresses within a body $\mathcal{B}$ to specified strain measurements. Formulation of constitutive laws depend on the material under consideration, allowable deformations (i.e incompressibility) and certain physical principles (i.e frame invariances). For material which behave elastically and undergo very small strains, it is appropriate to approximate the stresses using a linear function of strain, for example Hook's Law. However, this assumption is not valid when the material undergoes significant strains as in the case of cardiac mechanics.

Hyperelastic material descriptions begin with the formulation of an elastic potential ψ. From this elastic potential, or strain energy function, we derive the stresses and consequent constitutive law of our cardiac material. It is convenient to define the strain energy function in terms of the principal invariants of the Green strain tensor $\mathbf{E}$. The principal invariants of a tensor are scalars quantities that remain constant for any orthogonal coordinate transformation. The second order tensor $\mathbf{E}$ contains three independent invariants

$$I_1^E = \text{tr}\,(\mathbf{E}), \tag{2.50}$$

$$I_2^E = \frac{1}{2}\left[(\text{tr}\,\mathbf{E})^2 - \text{tr}\,\left(\mathbf{E}^2\right)\right], \tag{2.51}$$

$$I_3^E = \det \mathbf{E}. \tag{2.52}$$

2.5.1 Isotropy

An isotropic material is a material where the material properties are independent of the direction in which they are measured. Consider the *St. Venant-Kirchhoff* model, which is defined by the strain energy function

$$\psi(\mathbf{E}) = \frac{1}{2}\lambda \text{tr}\,(\mathbf{E})^2 + \mu \text{tr}\left(\mathbf{E}^2\right), \tag{2.53}$$

where λ and μ are the *Lamè* parameters which characterise the material response. If the strain energy function per unit volume is formulated in terms of the *Green strain tensor*, i.e., $\Psi(\mathbf{E})$, then the *second Piola-Kirchoff stress tensor*

is given by

$$\mathbf{S}(\mathbf{E}) = \frac{\partial \psi(\mathbf{E})}{\partial \mathbf{E}} = \lambda \text{tr } (\mathbf{E})\, 1 + 2\mu \mathbf{E}. \tag{2.54}$$

The material fourth order elasticity tensor $\overset{4}{C}$ is defined by the partial derivative of the *second Piola-Kirchhoff stress tensor* with respect to Green strain

$$\overset{\mathbf{4}}{\boldsymbol{C}} = \frac{\partial \mathbf{S}}{\partial \mathbf{E}}, \tag{2.55}$$

which for the *Piola-Kirchhoff* material is conveniently expressed in index notation as

$$\overset{4}{C}_{ijkl} = \frac{\partial S_{ij}}{\partial E_{kl}} = \lambda \delta_{ij}\delta_{kl} + \mu(\delta_{ik}\delta_{jl} + \delta_{il}\delta_{jk}). \tag{2.56}$$

Making use of Eq. (2.50) and Eq. (2.51) it is possible to construct the *St. Venant-Kirchhoff* strain energy function in terms of the invariants of $\mathbf{E}$. This is given as

$$\psi(I_1^E, I_2^E, I_3^E) = \frac{1}{2} I_1^{E^2} (\lambda + \mu) - \mu I_2^E, \tag{2.57}$$

which by definition ensures the condition of isotropy. Using the chain rule one can compose $\mathbf{S}$ in the general sense as

$$\mathbf{S}(I_1^E, I_2^E, I_3^E) = \sum_{i=1}^{3} \rho_0 \frac{\partial \psi(I_1^E, I_2^E, I_3^E)}{\partial I_i^E} \frac{I_i^E}{\partial \mathbf{E}}. \tag{2.58}$$

$\overset{\mathbf{4}}{\boldsymbol{C}}$ can be derived in a similar manner.

2.5.2 Transverse Isotropy

Materials that exhibit different material properties depending on the direction in which they are measured are called anisotropic. A special case of anisotropic material behaviour, is where the material deformation differs in two orthogonal directions. This form of anisotropic material behaviour is referred to as transverse isotropy. Transverse isotropy in a material occurs due to the microscopic nature of the material.

To mathematically describe this behaviour, the preferred material direction in the reference or Lagrangian description is introduced as the unit vector, $\mathbf{V}_1$. The structural tensor of a transversely isotropic material in the

Lagrangian description is thus given by

$$\mathbf{M}_1 = \mathbf{V}_1 \otimes \mathbf{V}_1. \tag{2.59}$$

In addition, the preferred material direction, $\mathbf{V}_1$, results in two additional invariants becoming necessary. The additional invariants are I_4 and I_5, which are given respectively by

$$I_4^E = \text{tr}\left(\mathbf{M}_1\mathbf{E}\right), \tag{2.60}$$

$$I_5^E = \text{tr}\left(\mathbf{M}_1\mathbf{E}^2\right), \tag{2.61}$$

where the square of the tensor, $\mathbf{E}$, is defined as $\mathbf{E}^2 = \mathbf{E}\mathbf{E}$. Finally, the *second Piola-Kirchoff stress tensor*, can be expressed in terms of the scalar invariants as

$$\mathbf{S} = \frac{\partial\psi(I_1^E, I_2^E, I_3^E, I_4^E, I_5^E)}{\partial\mathbf{E}} = \sum_{\alpha=1}^{\alpha=5} \frac{\partial\psi}{\partial I_\alpha^E}\frac{\partial I_\alpha^E}{\partial\mathbf{E}}. \tag{2.62}$$

2.5.3 Orthotropy

For an orthotropic material, three independent material directions are present, $\mathbf{V}_1$, $\mathbf{V}_2$ and $\mathbf{V}_3$, which define an orthonormal basis system. In this case, two additional structural tensors need to be defined as

$$\mathbf{M}_2 = \mathbf{V}_2 \otimes \mathbf{V}_2, \tag{2.63}$$

$$\mathbf{M}_3 = \mathbf{V}_3 \otimes \mathbf{V}_3. \tag{2.64}$$

Also, due to the two additional material directions, $\mathbf{V}_2$ and $\mathbf{V}_3$, four additional scalar invariants are introduced as

$$I_6 = \text{tr}\left(\mathbf{M}_2\mathbf{E}\right), \tag{2.65}$$

$$I_7 = \text{tr}\left(\mathbf{M}_2\mathbf{E}^2\right), \tag{2.66}$$

$$I_8 = \text{tr}\left(\mathbf{M}_3\mathbf{E}\right), \tag{2.67}$$

$$I_9 = \text{tr}\left(\mathbf{M}_3\mathbf{E}^2\right). \tag{2.68}$$

The Green strain tensor may be expressed in a local coordinate system, with basis vectors which are the material directions

$$\begin{aligned}\mathbf{E} =& \text{E}_{11}\mathbf{V}_1 \otimes \mathbf{V}_1 + \text{E}_{22}\mathbf{V}_2 \otimes \mathbf{V}_2 + \text{E}_{33}\mathbf{V}_3 \otimes \mathbf{V}_3 \\ &+ \text{E}_{12}\left(\mathbf{V}_1 \otimes \mathbf{V}_2 + \mathbf{V}_2 \otimes \mathbf{V}_1\right) + \text{E}_{13}\left(\mathbf{V}_1 \otimes \mathbf{V}_3 + \mathbf{V}_3 \otimes \mathbf{V}_1\right) \\ &+ \text{E}_{23}\left(\mathbf{V}_2 \otimes \mathbf{V}_3 + \mathbf{V}_3 \otimes \mathbf{V}_2\right),\end{aligned} \tag{2.69}$$

where E_{ij} represent the local components of the Green strain tensor. Finally, the *second Piola-Kirchoff stress tensor* can be expressed in terms of the nine

scalar invariants as

$$\mathbf{S} = \frac{\partial \psi(I_1^E, I_2^E, I_3^E, I_4^E, I_5^E, I_6^E, I_7^E, I_8^E, I_9^E)}{\partial \mathbf{E}} = \sum_{\alpha=1}^{\alpha=9} \frac{\partial \psi}{\partial I_\alpha^E} \frac{\partial I_\alpha^E}{\partial \mathbf{E}}. \tag{2.70}$$

2.6 Variational formulation and its linearization

In Section 2.4, the law of linear momentum conservation was derived, and Eq. (2.37) represented the Lagrangian equilibrium equation for a constant velocity field. Eq. (2.37) represents the governing differential equation for the cardiac mechanics problem. In addition, both traction and displacement boundary conditions are necessary for realistic modelling of cardiac function. Hence, the general strong form for the cardiac mechanics problem is

$$\mathrm{div}\mathbf{P} + \mathbf{b}\,(\mathbf{X}, t) = \mathbf{0} \qquad \text{in } \mathcal{B}, \tag{2.71}$$

$$\mathbf{P}\mathbf{n} = \mathbf{t}^{(\mathbf{n})} \text{ on } \partial\mathcal{B}_N, \tag{2.72}$$

$$\mathbf{u} = \bar{\mathbf{u}} \text{ on } \partial\mathcal{B}_D. \tag{2.73}$$

Referring to the above strong form, the first equation represents the equilibrium equation with negligible acceleration. The second equation expresses the prescribed traction force, $\mathbf{t}^{(\mathbf{n})}$, in the Lagrangian description, acting on the Neumann boundary, $\partial\mathcal{B}_N$. Finally, the last equation expresses the displacement boundary condition, $\bar{\mathbf{u}}$, on the Dirichlet boundary, $\partial\mathcal{B}_D$. Dirichlet boundary conditions are prescribed on $\partial\mathcal{B}_D \subset \partial\mathcal{B}$ and Neumann boundary conditions are prescribed on $\partial\mathcal{B}_N = \partial\mathcal{B}/\partial\mathcal{B}_D$.

The variational formulation (or weak form) of continuum mechanics states that the external potential, $\mathcal{W}_{\text{ext}}$, is equal to the internal potential, $\mathcal{W}_{\text{int}}$ [79]. The external potential corresponds to the work done by the external forces such as a body force, $\mathbf{b}$, acting over the volume of the body and traction forces, $\mathbf{t}^{(\mathbf{n})}$, acting on the surface of the body. The external potential is given by

$$\mathcal{W}_{ext} = \int_{\mathcal{B}} \mathbf{b} \cdot \delta\mathbf{u} dV + \int_{\partial\mathcal{B}_N} \mathbf{t}^{(\mathbf{n})} \cdot \delta\mathbf{u} dA, \tag{2.74}$$

where $\delta\mathbf{u}$ is the variation of displacement. dV is a volume element of domain $\mathcal{B}$, whereas dA is a surface element of its corresponding boundary $\partial\mathcal{B}$ with the outward surface normal vector $\mathbf{n}$. Now the internal potential is given by

$$\mathbf{\Psi}_{int} = \int_{\mathcal{B}} \frac{\partial \psi}{\partial \mathbf{E}} : \delta\mathbf{E} dV, \tag{2.75}$$

where $\delta\mathbf{E}$ is the variation of the Green strain tensor. The full variational formulation, which is the sum of internal and external potential can be stated as

$$\begin{aligned}\mathcal{F} =& \boldsymbol{\Psi}_{int} - \mathcal{W}_{ext} = 0 \\ =& \int_{\mathcal{B}} \mathbf{S} : \delta\mathbf{E}\, dV - \int_{\mathcal{B}} \mathbf{b} \cdot \delta\mathbf{u}\, dV - \int_{\partial\mathcal{B}_N} \mathbf{t}^{(\mathbf{n})} \cdot \delta\mathbf{u}\, dA = 0\end{aligned} \tag{2.76}$$

where Eq (2.74) and Eq (2.75) have been substituted and $\mathbf{S}$ denotes the second *Piola-Kirchhoff* stress tensor given by

$$\mathbf{S} = \frac{\partial\psi}{\partial\mathbf{E}} \tag{2.77}$$

The double dot operator (:) denotes the scalar product of tensors. This variational principle is supplemented by the essential boundary conditions given in Eq (2.73).

It can be shown that the variational formulation in Eq. (2.76) can be derived from the strong form. This derivation will not be illustrated but the reader is directed to the book *Nonlinear finite element methods* by Wriggers [79] for further details.

The above variational statement in Eq. (2.76) is solved incrementally and iteratively employing the *Newton-Raphson* method. At each iteration step, i, of a loading or time step, n, the discrete equation system is assembled from the linearisation of the variational statement. The variational statement is linearised using a first order Taylor series expansion, about an initial guess for the displacement vector, $\mathbf{u}_n^{i-1}$, which yields,

$$\mathcal{F}(\mathbf{u}) = \mathcal{F}(\mathbf{u}_n^{i-1} + \Delta\mathbf{u}) = \mathcal{F}(\mathbf{u}_n^{i-1}) + \frac{\partial\mathcal{F}}{\partial\mathbf{u}}|_{\mathbf{u}_n^{i-1}} \cdot \Delta\mathbf{u} \approx 0, \tag{2.78}$$

where $\Delta\mathbf{u}$ is the incremental displacement field such that $\mathbf{u} = \mathbf{u}_n^{i-1} + \Delta\mathbf{u}$. Making use of a numerical approximation of the displacement field, here MLS-approximations, the linearized problem formulation (Eq. (2.78)) results in a discrete equation system of the following form

$$\mathbf{K}_n^i \Delta\mathbf{u}_n^i = [\mathbf{f}_{ext}]_n^i - [\mathbf{f}_{int}]_n^i = \mathbf{R}_n^i, \tag{2.79}$$

where, $\mathbf{R}_n^i$ is the residual of the of the discrete equation system. Also, $\mathbf{K}_n^i = \mathbf{K}\left(\mathbf{u}_n^{i-1}\right)$, and $\mathbf{R}_n^i = \mathbf{R}\left(\mathbf{u}_n^{i-1}\right)$, i.e., the tangent matrix and residual vector respectively, are evaluated at the initial guess for the displacement field, $\mathbf{u}_n^{i-1}$.

In the current framework of SESKA, the diastolic filling phase is usually pressure driven. Therefore, the cavity pressure is increased from a starting pressure, up to some user specified end-diastolic maximum. In order to solve the variational formulation for a specified end-diastolic pressure, it is necessary to solve the discrete equation system for incrementally increasing load, because the *Newton-Raphson* method will only converge if the initial guess for the displacement vector is close enough to the actual solution.

The incremental loading procedure is achieved by multiplying a final pressure, $\mathbf{P}^0$, by a Neumann loading factor, λ_n, that increases from an initial value of 0, upto some user defined maximum loading (i.e. the required end-diastolic pressure). The blood pressure, $\mathbf{P}$, exerted on the endocardium is therefore expressed as

$$\mathbf{P} = \lambda_n \mathbf{P}_0. \tag{2.80}$$

Furthermore, λ_n in Eq. (2.80) is computed as

$$\lambda_n = \lambda_{n-1} + \Delta\lambda_n, \tag{2.81}$$

where $\Delta\lambda_n$ is the loading factor increment for the current calculation step. Hence, for an incremental loading approach, the discrete equation system in Eq. (2.79) is reformulated as

$$\mathbf{K}_n^i \Delta\mathbf{u}_n^i = \lambda_n \left[\mathbf{f}_{ext}^0\right] - \left[\mathbf{f}_{int}\right]_n^i = \mathbf{R}_n^i. \tag{2.82}$$

Next, the discrete equation system is solved for the unknown displacement increment, $\Delta\mathbf{u}_n^i$, with

$$\Delta\mathbf{u}_n^i = \left[\mathbf{K}_n^i\right]^{-1} \mathbf{R}_n^i, \tag{2.83}$$

Therefore, the displacement field, $\mathbf{u}_n^i$, is updated at each iteration step using

$$\mathbf{u}_n^i = \mathbf{u}_n^{i-1} + \Delta\mathbf{u}_n^i. \tag{2.84}$$

The updated displacement field, $\mathbf{u}_n^i$, is then used as the initial guess for the next iteration $(i+1)$. It is important to note that for the first iteration step (i=0), the initial guess of the displacement field, is taken to be the displacement solution from the previous converged calculation step, i.e., $\mathbf{u}_n^{i-1} = \mathbf{u}_{n-1}$.

The iterative procedure is terminated when the Euclidean norm of residual vector, $||\mathbf{R}_n^i||$, falls below a desired threshold, ϵ_s. $||\mathbf{R}_n^i||$, is computed as

$$||\mathbf{R}_n^i|| = \sqrt{[\mathbf{R}_n^i]^{\mathrm{T}}\,\mathbf{R}_n^i}. \tag{2.85}$$

When $||\mathbf{R}_n^i||$ falls below the desired threshold, it implies that $[\mathbf{f}_{ext}]_n^i \approx [\mathbf{f}_{int}]_n^i$, which represents static equilibrium between externally applied loads and internal reactions of the body. In this scenario, the calculation then proceeds to the next loading step (i.e. $n := n + 1$).

2.7 Element-free Galerkin method

When it comes to modelling formulations of solids and structures, it is the finite element method (FEM) which is the usual choice. However, in the case of formulations which involve higher order derivatives such as strain gradient plasticity theory, it was shown that their implementation into the finite element code is rather limited [81] [65].

The Element-free Galerkin (EFG) method is a meshless method which is used for solving partial differential equations with moving least squares interpolants. EFG methods require only nodal data, no element connectivity is needed. Instead of using a mesh, as in finite element methods, a particle distribution is used to calculate the shape functions. In SESKA, the moving least squares (MLS) method is used to compute the shape functions and approximate displacement, strain and stress over the domain. It should be noted that FEM is utilized as a background mesh for numerical integration purposes. The MLS method will be presented in Section 4.3.

For a detailed treatment on the EFG and MLS methods, the reader is directed to the paper by Belytschko, Lu, and Gu [2]. The work by Dr Sebastian Skatulla [64] can be referred to for a detailed treatment on moving least squares approximations and the fundamental underlying principles of SESKA.

Chapter 3

Cardiac mechanics

This chapter will present the key physiological principles required to model the behaviour of the human heart. The basic functioning of the heart and all its constituents will be presented. The structural components of the heart will also be examined. For a more detailed treatment of the physiology of the heart, the reader is referred to the publications by Katz et al.[30] and Guyton et al.[20].

3.1 Structure of the human heart

Although it may appear complex at first, the heart is a well-structured organ. It consists of four chambers. The first two chambers are known as the right and left atria. These two chambers receive blood from the body. The last two chambers are known as the left and right ventricles. The left ventricle pumps blood to the body while the right ventricle sends blood to the lungs. These four chamber and the course of blood flow are shown in Figure 3.1. The atria are smaller than the ventricles and have thinner, less muscular walls than the ventricles. The atria act as receiving chambers for blood, so they are connected to the veins that carry blood to the heart. The ventricles are the larger, stronger pumping chambers that send blood out of the heart. The ventricles are connected to the arteries that carry blood away from the heart.

The structure of the heart wall is made of three layers:

- *Epicardium*: The epicardium is the outermost layer of the heart wall. It is a thin membrane layer that helps to lubricate and protect the outside of the heart.
- *Myocardium*: The myocardium is the muscular middle layer of the heart wall that contains the cardiac muscle tissue. Myocardium makes up the majority of the thickness and mass of the heart wall and is the part of the heart responsible for pumping blood.

- *Endocardium*: Endocardium is the inner layer of the heart. The endocardium is very smooth and is responsible for keeping blood from sticking to the inside of the heart and forming potentially deadly blood clots.

The chambers on the right side of the heart are smaller and have less myocardium in their heart wall when compared to the left side of the heart. This difference in size between the sides of the heart is related to their functions and the size of the two circulatory loops. The right side of the heart maintains pulmonary circulation to the nearby lungs while the left side of the heart pumps blood all the way to the extremities of the body in the systemic circulatory loop.

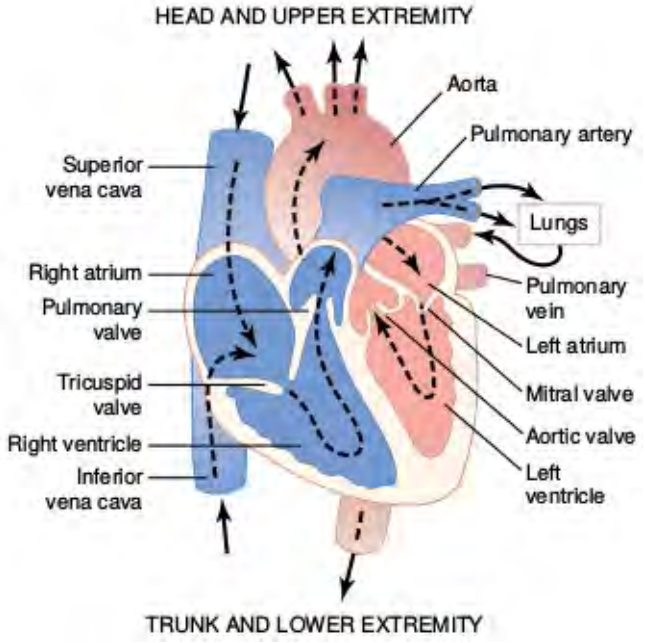

FIGURE 3.1: Structure of the heart and the course of blood flow through the heart chambers and heart valves. Image from textbook by Guyton and Hall [20].

The left ventricle is the largest cavity in the heart and the most susceptible to myocardial infarctions. It is therefore a logical choice for the left ventricle to be the favoured starting point in cardiac modelling. This research will focus on the myocardium layer since this makes up the majority of the thickness and mass of the heart wall and is the part of the heart responsible for pumping blood.

3.2 Physiology of cardiac muscle

The heart is composed of three major types of cardiac muscle: *atrial muscle*, *ventricular muscle*, and specialized *excitatory* and *conductive muscle* fibres

[20]. The atrial and ventricular types of muscle contract in much the same way as other muscles such as skeletal muscle, except that the duration of contraction is much longer. Figure 3.2 shows a typical histological picture of cardiac muscle, demonstrating cardiac muscle fibres arranged in a latticework structure, with the fibres dividing, recombining, and then spreading again [20].

Cardiac muscle can be thought of as a Syncytium [20], which is a multinucleate mass of protoplasm produced by the merging of cells. The dark areas crossing the cardiac muscle fibres in Figure 3.2 are called intercalated discs. These are cell membranes that separate individual cardiac muscle cells from one another, which follows that cardiac muscle fibres are made up of many individual cells connected in series and in parallel with one another.

At each intercalated disc the cell membranes fuse with one another in such a way that they form permeable "communicating" junctions which are also known as gap junctions. These allow almost totally free diffusion of ions. Ions are able to move with ease in the intracellular fluid along the longitudinal axes of the cardiac muscle fibres, so that action potentials travel easily from one cardiac muscle cell to the next, past the intercalated discs. Thus, cardiac muscle is a syncytium of many heart muscle cells in which the cardiac cells are so interconnected that when one of these cells becomes excited, the action potential spreads to all of them, spreading from cell to cell throughout the latticework interconnections.

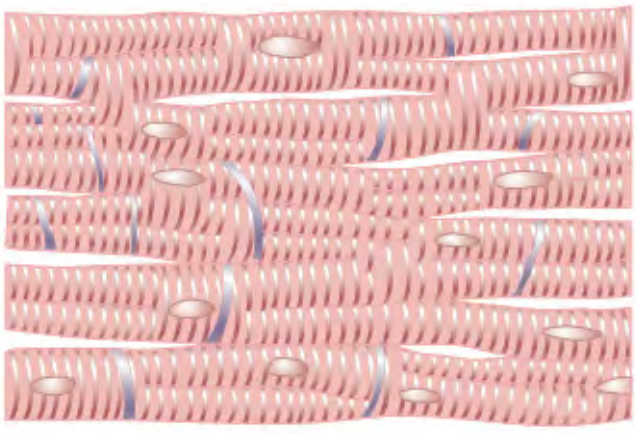

FIGURE 3.2: Syncytial interconnecting nature of cardiac muscle fibres. Cited from Guyton and Hall [20].

The heart is actually composed of two syncytiums: the *atrial syncytium* that constitutes the walls of the two atria, and the *ventricular syncytium* that constitutes the walls of the two ventricles. The atria are separated from the

ventricles by fibrous tissue that surrounds the atrioventricular (A-V) valvular openings between the atria and ventricles. This division of the muscle of the heart into two functional syncytiums allows the atria to contract a short time ahead of ventricular contraction, which is important for the effectiveness of heart pumping.

3.3 Cardiac tissue orientation

The human heart is composed of a helical network of muscle fibres organized to form sheets that are separated by a complex structure of cleavage planes [54] [6]. Understanding the 3-dimensional (3D) configuration of the fibre and sheet structure is important for modelling the mechanical properties of the heart. A comprehensive way to visualize these fibres is the use of 3D paths throughout the ventricle where the sheets are well represented by their cleavage planes [54].

The left ventricle is organized in a collection of muscle fibres composed of myocytes (muscle cells) where each are 80 to 100 μm in length and have a cylindrical shape with a radius of 5 to 10 μm [24]. Histologic studies have shown that the orientation of the fibre angles vary continuously from approximately +60° to -60° across the wall, where from the apex to the base the fibres are a left-handed spiral from the epicardium to the midwall, have a planar circular geometry in the midwall, and are a right-handed spiral from the midwall to the endocardium [54]. The fibres and sheets of the heart form a very complex structure overall. The reader is referred to Rohmer, Sitek, and Gullberg [54] and Costa et al. [6] for a more detailed treatment of the topic.

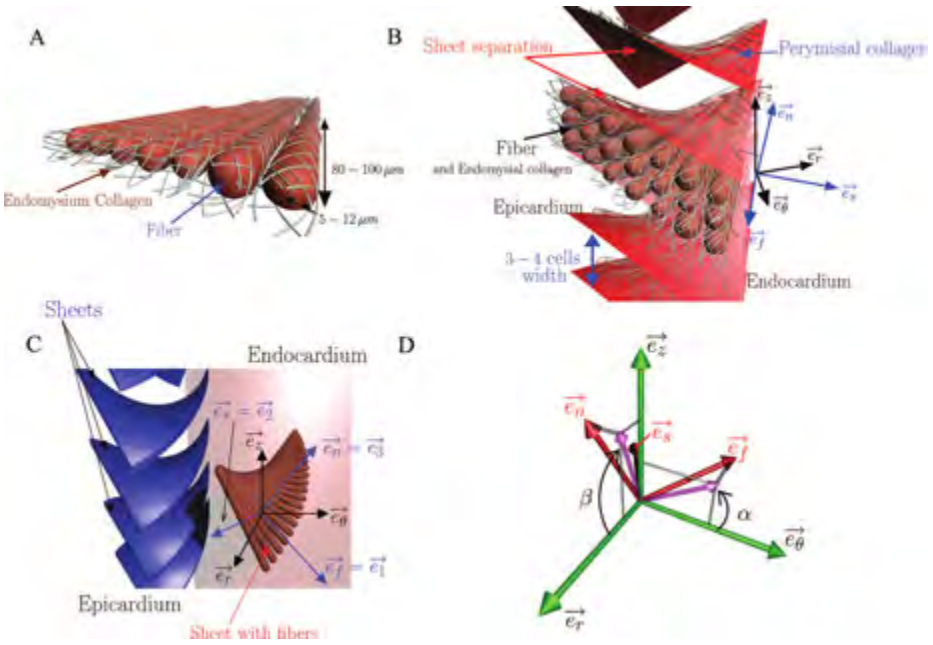

FIGURE 3.3: Representation of the fibres in the heart adopted from Rohmer, Sitek, and Gullberg [54].

Figure 3.3A shows how the long oval structures correspond to the fibres. Figure 3.3B shows the laminar structure in the heart while Figure 3.3C shows a simplified visualization of the sheet and fibre spatial arrangement with the associated coordinate systems. Figure 3.3D exhibits the definition of the fibre angle α and sheet angle β.

3.4 Cardiac cycle

The cardiac events that occur from the beginning of one heartbeat to the beginning of the next collectively make up what is called the *cardiac cycle*. The cardiac structure's physiological function is to ensure directed blood flow through the heart over the cardiac cycle. Each cycle is initiated by a generation of an action potential in the sinus node which is located in the superior vena cava. The action potential then travel from the sinus node rapidly through both atria and then through the A-V bundle into the ventricles. Because of this special arrangement of the conducting system from the atria into the ventricles, there is a delay of more than 0.1 second during passage of the cardiac impulse from the atria into the ventricles. This allows the atria to contract ahead of ventricular contraction, thereby pumping blood into the ventricles before the strong ventricular contraction begins. Thus, the atria act as primer pumps for the ventricles, and the ventricles in turn provide the major source of power for moving blood through the body's

vascular system. The heart has an elegant and complex biomechanical function. Moreover, it must replicate it's cyclic function over an entire lifetime, with an estimated total functional demand of least $3x10^9$ cycles [59].

The cardiac cycle can be divided into four phases as illustrated in Figure 3.4 and listed below:

- *Passive filling*: The mitral valve opens, allowing blood to fill the ventricle. The cavity volume increases as more blood flows into the ventricle and the pressure increases accordingly. The material behaves completely passively in this phase.
- *Isovolumetric contraction*: The ventricle contracts with the valves closed. The cavity volume remains constant or nearly constant since all valves are closed and the pressure in the cavity increases due to the contraction of the ventricle. Active tension is introduced in this phase and continuously increases at a rapid pace.
- *Ejection*: Once the pressure within the cavity reaches the same pressure as in the aorta, the aortic valve opens and blood is ejected from the ventricle. The cavity volume decreases as blood is ejected from the contracting left ventricle. The pressure in the cavity first increases further due to the compliance of the aorta and then decreases as the rate of ejection decreases. The active tension reaches a peak in this phase and starts to tail off.
- *Isovolumic relaxation*: Once the cavity ceases to contract further, the aortic valve closes and the ventricle relaxes. The cavity volume remains constant or nearly constant as all the valves are closed. The pressure decreases due to the relaxation of the ventricle. The active tension declines to zero and by the end of relaxation the material is once again in a fully passive state.

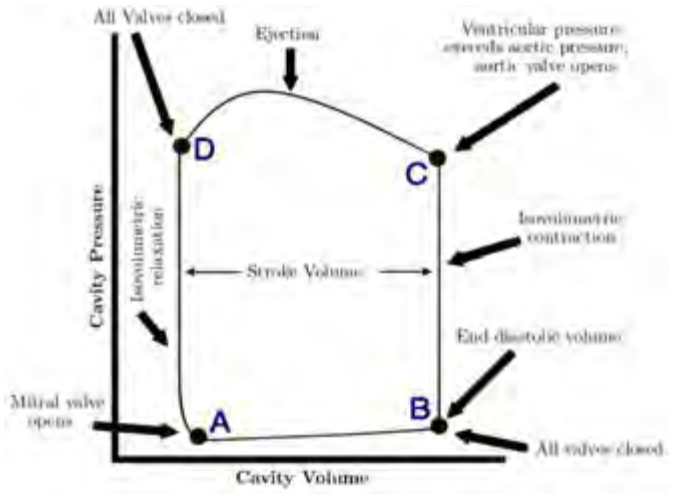

FIGURE 3.4: Pressure volume relation of the left ventricle (LV) during the cardiac cycle

The end systolic volume (ESV) is defined as the cavity volume at the end of ejection. The end diastolic volume (EDV) is defined as the cavity volume immediately prior to isovolumetric contraction. The stroke volume is the amount of blood expelled during systole (i.e. the difference between end diastolic volume and end systolic volume). This research will focus on the passive filling during the diastolic phase only.

In brief, the loop (shown in Figure 3.4) involves three calculation models:

- Passive stress model
- Active stress model
- Windkessel model

The passive stress model applies throughout the cardiac cycle. The active stress model applies to the isovolumetric contraction, ejection and isovolumetric relaxation phase. The Windkessel model applies to the ejection and isovolumetric relaxation phase when the valves are open. This research will only require the passive stress model.

3.5 Passive stress model

During the filling phase of the left ventricle, the myocardium is deformed in a passive manner. This deformation is largely dictated by the fibre distribution and orientation of the myocytes. To account for this in modelling, numerous models have been used in literature over the past 30 years, but most of them are quite closely linked. Three major categories of passive mechanics strain energy, based of the type of fibres, can be differentiated. The

description of these categories are summarised from Usyk and McCulloch [75] and given in the paragraph below:

- **Isotropic constitutive model**
  This model is based on the isotropic constitutive equation which is constructed from a simple Mooney-Rivlin strain-energy function. The equation was found to be ideal in predicting large deformations as encountered in real hearts. However, to have one which is more suited to predict stress and strains in heart tissue, an exponential term, which includes the first principal invariant of the right Cauchy-green deformation tensor, I_1^A , was added to the potential energy function, which also includes a stress scaling factor, A. In order to cater for the assumption that the myocardium muscles are incompressible, a Lagrange multiplier, p, was incorporated along with the third principal invariant of the right Cauchy-green deformation tensor, I_3. The final form of the strain energy function is as follows:

$$\psi = A(e^{b(I_1-3)} - 1) + \frac{p}{2}(I_3^A - 1) \tag{3.1}$$

- **Transverse isotropic constitutive model**
  With the isotropic material behaviour, the approximation is poor because it does not consider the myocardium preferred fibre direction. Using a transversal isotropic strain energy function, the new passive constitutive law is now defined by three material constants which are determined from the biaxial experimental test. By also including the compressibility term, the resulting equation obtained from [75] is:

$$\psi = A\frac{(e^Q - 1)}{2} + A_{comp}(I_3 \cdot lnI_3 - I_3 + 1) \tag{3.2}$$

  with

$$\begin{aligned} Q =& b_{ff}E_{ff}^2 + b_{xx}(E_{cc}^2 + E_{ss}^2 + E_{cs}^2 + E_{sc}^2) + \\ &+ b_{fx}(E_{fc}^2 + E_{cf}^2 + E_{fs}^2 + E_{sf}^2) \end{aligned} \tag{3.3}$$

  where both the material constant b_{ij} and the Green strain tensor E_{ij} is direction dependent. i and j refer to either the fibre axis, f , or sheet axis, s, or the sheet-normal axis, c. The compressibility term is a penalty term which penalizes volumetric strains in order to enforce nearly incompressible material behaviour. Regarding the parameters b_{ij} , different sets of values are required if a canine, rat or human heart is to be considered as each one behaves in a different manner. Most finite element models to date have used transversely isotropic material laws for myocardium.

- **Orthotropic constitutive model**
  The orthotropic material constitutive law is a generalisation of the transversely isotropic material. In this case, all three material directions of the fibre sheets can be considered. In this way, the effect of inter-laminar tensile and shear stiffness can be easily regulated to increase the accuracy of the material behaviour. On the other hand, it also leads to a greater number of material constants which is difficult to determine from experiments. The following equation given in [75] describes an orthotropic material:

$$\psi = A\frac{(e^Q - 1)}{2} + A_{comp}(I_3 \cdot lnI_3 - I_3 + 1) \tag{3.4}$$

with

$$\begin{aligned} Q =& b_{ff}E_{ff}^2 + b_{cc}E_{cc}^2 + b_{ss}E_{ss}^2 + b_{cs}(E_{cs}^2 + E_{sc}^2) + b_{fs}(E_{fs}^2 + E_{sf}^2) + \\ &+ b_{fc}(E_{fc}^2 + E_{cf}^2) \end{aligned} \tag{3.5}$$

Herein, the components E_{ij} of the *Green* strain $\mathbf{E}$ are associated with a local Cartesian basis $\mathbf{V}_i$, $i = 1, 2, 3$ with fibre axis $\mathbf{V}_1$, the sheet axis $\mathbf{V}_2$, and the sheet-normal axis $\mathbf{V}_3$, therefore

$$\begin{aligned} \mathbf{E} =& \mathrm{E}_{11}\mathbf{V}_1 \otimes \mathbf{V}_1 + \mathrm{E}_{22}\mathbf{V}_2 \otimes \mathbf{V}_2 + \mathrm{E}_{33}\mathbf{V}_3 \otimes \mathbf{V}_3 \\ &+ \mathrm{E}_{12}\left(\mathbf{V}_1 \otimes \mathbf{V}_2 + \mathbf{V}_2 \otimes \mathbf{V}_1\right) + \mathrm{E}_{13}\left(\mathbf{V}_1 \otimes \mathbf{V}_3 + \mathbf{V}_3 \otimes \mathbf{V}_1\right) \\ &+ \mathrm{E}_{23}\left(\mathbf{V}_2 \otimes \mathbf{V}_3 + \mathbf{V}_3 \otimes \mathbf{V}_2\right). \end{aligned} \tag{3.6}$$

The second term in Eq. (3.4) serves to enforce the assumed nearly incompressible material behaviour, where the right stretch is denoted by I_3. Then Q may be expressed alternatively

$$\begin{aligned} Q =& a_1(\mathrm{tr}(\mathbf{M}_1\mathbf{E}))^2 + a_2(\mathrm{tr}(\mathbf{M}_2\mathbf{E}))^2 + a_3(\mathrm{tr}(\mathbf{M}_3\mathbf{E}))^2 \\ &+ a_4\mathrm{tr}(\mathbf{M}_1\mathbf{E}^2) + a_5\mathrm{tr}(\mathbf{M}_2\mathbf{E}^2) + a_6\mathrm{tr}(\mathbf{M}_3\mathbf{E}^2), \end{aligned} \tag{3.7}$$

with the structural tensors $\mathbf{M}_i$ defined by

$$\mathbf{M}_1 = \mathbf{V}_1 \otimes \mathbf{V}_1,\ \mathbf{M}_2 = \mathbf{V}_2 \otimes \mathbf{V}_2,\ \mathbf{M}_3 = \mathbf{V}_3 \otimes \mathbf{V}_3. \tag{3.8}$$

Chapter 4

Reduced order method

A reduced order method (ROM) is a technique commonly used to decrease the complexity of large system of equations. This is achieved by compressing the whole system to such a point that accuracy is not greatly reduced and that the general behaviour of the problem, e.g. its mechanics, is preserved.

One widely used ROM is the so called proper orthogonal decomposition (POD). This work will make use of a variation of the POD method called proper orthogonal decomposition with interpolation (PODI). The PODI method employs an interpolation technique called the Moving Least Square Approximation method (MLS) [36]. The focus of this chapter will be to introduce the reader to the POD, PODI and MLS techniques.

4.1 Proper orthogonal decomposition (POD)

There are various forms of the POD method. In the literature, three distinct forms are usually found, namely the Kharhunen-Loéve Decomposition (KLD), the Singular Value Decomposition (SVD) or the Principal Component Analysis (PCA). In this paper, the KLD has been chosen to explain the POD and the mathematical formulation presented closely follows the one in Rama, S.Skatulla, and C.Sansour [53]. Literature by Tan, Willcox, and Damodaran [71] was also consulted.

Suppose $\mathbf{U}$ is an ensemble set of displacement fields, describing the state of deformation of a body at discrete time steps t_i, i = 1, 2,...,n, which have been defined over a one-dimensional spatial domain $0 \leq x \leq 1$.

$$\mathbf{U} = \{\mathbf{u}^1, \mathbf{u}^2, ..., \mathbf{u}^n\} \tag{4.1}$$

where for the total number of time steps it holds $n << m$, and m is the number of displacement degrees of freedom. If the displacement field is

approximated by a set of basis vectors, $\widetilde{\mathbf{\Phi}}$, and coefficients, α, through

$$\mathbf{u}_i = \sum_{j=1}^{n} \alpha_i^j \widetilde{\mathbf{\Phi}}^j, \tag{4.2}$$

then, the KLD problem is posed as an optimality scheme which requires one to maximise the average projection of $\mathbf{U}$ onto $\widetilde{\mathbf{\Phi}}$ while being subjected to the constraint of $\widetilde{\mathbf{\Phi}}$ being orthonormal:

$$\max_{\widetilde{\mathbf{\Phi}}} \left\langle \left| \left(\mathbf{U}, \widetilde{\mathbf{\Phi}} \right) \right|^2 \right\rangle \text{ such that } \left\| \widetilde{\mathbf{\Phi}} \right\|^2 = 1, \tag{4.3}$$

with

$$(\mathbf{f}, \mathbf{g}) = \int_0^1 \mathbf{f}(x)\mathbf{g}^{\mathrm{T}}(x)dx, \tag{4.4}$$

with $\langle \cdot \rangle$ being the averaging operation and $\|\mathbf{f}\| = (\mathbf{f}, \mathbf{f})^{\frac{1}{2}}$. The Lagrange multiplier method is then used to solve Eq.(4.3) and the following eigenvalue problem is obtained:

$$\left(\mathbf{R}, \widetilde{\mathbf{\Phi}} \right) = \boldsymbol{\lambda} \widetilde{\mathbf{\Phi}} \tag{4.5}$$

with

$$\mathbf{R} = \frac{1}{n} \mathbf{U}\mathbf{U}^{\mathrm{T}}. \tag{4.6}$$

Solving the above produces a set of eigenfunctions which is optimal to the optimisation problem stated in Eq. (4.3). $\mathbf{R}$ is usually referred to as the *kernel* and is a positive semi-definite symmetric matrix [71]. It is also defined as the *auto-correlation* matrix [9]. The eigenvalues are known as proper orthogonal values (POVs) and the eigenfunctions are known as proper orthogonal modes (POMs). The POV and POM are represented by $\boldsymbol{\lambda}$ and $\widetilde{\mathbf{\Phi}}$ respectively.

If $\mathbf{R}$ is computed from a whole set of data $m \times n$, with m being very large, then the resulting matrix would be of size $m \times m$ and thus, extremely large as well. This would increase the computational time to find solutions for $\boldsymbol{\lambda}$ and $\widetilde{\mathbf{\Phi}}$. One commonly used method to reduce the system was proposed by Sirovich [62] in 1987 and is known as the *snapshot method* [62] [63]. To decrease the size of the aforementioned matrix, Eq. (4.5) could be modified to the form of

$$(\boldsymbol{C}, \boldsymbol{\xi}) \text{ with } \mathbf{C} = \frac{1}{n} \mathbf{U}^{\mathrm{T}}\mathbf{U} \tag{4.7}$$

The eigenvalues of $\mathbf{C}$ are the same as those obtained from Eq. (4.5), which are the sought POVs. It should be noted that the associated eigenvectors are not proper orthogonal modes. In order to circumvent this problem,

Li, Luo, and Chen [38] proposed the following equation

$$\widetilde{\mathbf{\Phi}}^i = \frac{1}{\sqrt{n\lambda_i}} \boldsymbol{U}\boldsymbol{\xi}^i \tag{4.8}$$

To preserve the energy of the dataset $\mathbf{U}$ when it is being reduced from a higher order solution space to a lower order solution space, Falkiewicz and Cesnik [12] proposed the following expression

$$\varepsilon_{rel} = \frac{\sum_{f=1}^{n-r} \lambda_f}{\sum_{g=1}^{n} \lambda_g} \times 100 \tag{4.9}$$

with r being the number of POMs conserved and $r < n$. It then follows that in order to find a proper balance between selecting a few POMs and conserving the greatest amount of energy, the POD basis associated with the highest POVs is selected, because the former represents the dominant modes of deformation [53]. Lin, Zhang, and Li [40] noted that, with their set of data comprising of 24 snapshots, only the first two POVs were enough to achieve an energy conservation of 99.9997 %.

The application of the POMs to reduce a system of equations is straight forward. A good example to illustrate the procedure is the discretized equation of motion as encountered in the finite element method

$$\underset{(m\times m)(m\times 1)}{\mathbf{M}} \quad \underset{(m\times 1)}{\ddot{\mathbf{u}}} + \underset{(m\times m)(m\times 1)}{\mathbf{C}} \quad \underset{(m\times 1)}{\dot{\mathbf{u}}} + \underset{(m\times m)(m\times 1)}{\mathbf{K}} \quad \underset{(m\times 1)}{\mathbf{u}} = \underset{(m\times 1)}{\mathbf{F}} \tag{4.10}$$

where

$\mathbf{M}$ = mass matrix

$\mathbf{C}$ = damping matrix

$\mathbf{K}$ = stiffness matrix

$\mathbf{F}$ = force vector

$\ddot{\mathbf{u}}$ = acceleration vector

$\dot{\mathbf{u}}$ = velocity vector

$\mathbf{u}$ = displacement vector

For a large problem with the number of degrees of freedom, m, being high, the solving for Eq. (4.10) is computationally expensive and time consuming. To simplify this, the POMs can be used to project the system of equations from the high dimensional space to a low dimensional one. In order

to do so, $\mathbf{u}$ is then assumed to be approximated by $\mathbf{\Phi}$, which is an ensemble of the r most dominant POMs selected from $\widetilde{\mathbf{\Phi}}$ in

$$\underset{(m\times 1)}{\mathbf{u}} \approx \underset{(m\times r)}{\mathbf{\Phi}} \underset{(r\times 1)}{\boldsymbol{\psi}} \tag{4.11}$$

where $\boldsymbol{\psi}$ denotes a coefficient vector. As Niroomandi et al. [50] showed, Eq. (4.11) can be substituted into Eq. (4.10) which is additionally multiplied by $\mathbf{\Phi}^{\mathrm{T}}$. The resulting system of equations is reduced from size m to r as shown in the following set of equations

$$\begin{aligned}\Bigg[\underbrace{\underset{(r\times m)}{\mathbf{\Phi}^T}\underset{(m\times m)}{\mathbf{M}}\underset{(m\times r)}{\mathbf{\Phi}}}_{(r\times r)}\Bigg]\underset{(r\times 1)}{\ddot{\boldsymbol{\psi}}} + \Bigg[\underbrace{\underset{(r\times m)}{\mathbf{\Phi}^T}\underset{(m\times m)}{\mathbf{C}}\underset{(m\times r)}{\mathbf{\Phi}}}_{(r\times r)}\Bigg]\underset{(r\times 1)}{\dot{\boldsymbol{\psi}}} + \\ + \Bigg[\underbrace{\underset{(r\times m)}{\mathbf{\Phi}^T}\underset{(m\times m)}{\mathbf{K}}\underset{(m\times r)}{\mathbf{\Phi}}}_{(r\times r)}\Bigg]\underset{(r\times 1)}{\boldsymbol{\psi}} = \underbrace{\underset{(r\times m)}{\mathbf{\Phi}^T}\underset{(m\times 1)}{\mathbf{F}}}_{(r\times 1)}\end{aligned} \tag{4.12}$$

4.2 Proper orthogonal decomposition with interpolation (PODI)

For the purpose of real-time modelling of the heart, the direct application of POD is not suitable. This is because when applied to the finite element method (FEM), only the solving part of the overall process is accelerated while the time spent on preprocessing and the repetitive assembly of the discrete equation system prohibits a drastic drop in calculation time [53]. Hence, in order to circumvent this problem, the Proper Orthogonal Decomposition with Interpolation (PODI), developed by Ly and Tran [43], is employed in the in-house POD software, ORION. The idea of Ly and Tran [43] starts by first constructing the matrix $\mathbf{U}$ from a group of displacement field vectors $\{\mathbf{u}^1, ..., \mathbf{u}^p\}$. Each dataset $\mathbf{u}^a$, where $\mathbf{u}^a \in \{\mathbf{u}^1, ..., \mathbf{u}^p\}$, corresponds to a set of parameters, $\boldsymbol{\theta}^a$, where $\boldsymbol{\theta}^a \in \{\boldsymbol{\theta}^1, ..., \boldsymbol{\theta}^p\}$. Here, $\{\boldsymbol{\theta}^1, ..., \boldsymbol{\theta}^p\}$ is defined as a sequence of parameter sets.

From there, the POD calculation is carried out and used to transfer the datasets to a low-dimensional space using the POMs where an interpolation technique is employed to approximate the solution of a similar problem in the low-dimensional space. Then this interpolated solution is projected back to the high-dimensional space. The derivation of the method is given by first applying Eq. (4.11) to each dataset $\mathbf{u}^a$

$$\mathbf{u}^a \approx \psi_1^a \boldsymbol{\Phi}^1 + \psi_2^a \boldsymbol{\Phi}^2 + ... + \psi_r^a \boldsymbol{\Phi}^r \tag{4.13}$$

or in matrix form it is expressed as

$$\begin{bmatrix} u_1^a \\ u_2^a \\ . \\ . \\ . \\ u_{m-1}^a \\ u_m^a \end{bmatrix} \approx \psi_1^a \begin{bmatrix} \phi_1^1 \\ \phi_2^1 \\ . \\ . \\ . \\ \phi_{m-1}^1 \\ \phi_m^1 \end{bmatrix} + \psi_2^a \begin{bmatrix} \phi_1^2 \\ \phi_2^2 \\ . \\ . \\ . \\ \phi_{m-1}^2 \\ \phi_m^2 \end{bmatrix} + ... + \psi_r^a \begin{bmatrix} \phi_1^r \\ \phi_2^r \\ . \\ . \\ . \\ \phi_{m-1}^r \\ \phi_m^r \end{bmatrix} \tag{4.14}$$

Combining all datasets approximated by Eq. (4.13), we arrive at

$$\mathbf{U} \approx \mathbf{\Phi}\mathbf{\Psi} \tag{4.15}$$

which in matrix form is expressed as

$$\begin{bmatrix} u_1^1 & u_1^2 & . & . & u_1^{p-1} & u_1^p \\ u_2^1 & u_2^2 & & & & u_2^p \\ . & . & . & & & . \\ . & . & & . & & . \\ . & . & & & . & . \\ u_{m-1}^1 & & & & & u_{m-1}^p \\ u_m^1 & u_m^2 & . & . & u_m^{p-1} & u_m^p \end{bmatrix} \approx \begin{bmatrix} \phi_1^1 & \phi_1^2 & . & . & . & \phi_1^r \\ \phi_2^1 & \phi_2^2 & . & . & . & \phi_2^r \\ . & . & & & & . \\ . & . & & & & . \\ . & . & & & & . \\ \phi_{m-1}^1 & \phi_{m-1}^2 & . & . & . & \phi_{m-1}^r \\ \phi_m^1 & \phi_m^2 & . & . & . & \phi_m^r \end{bmatrix} \begin{bmatrix} \psi_1^1 & \psi_1^2 & . & . & . & \psi_1^p \\ \psi_2^1 & \psi_2^2 & . & . & . & \psi_2^p \\ . & . & & & & . \\ . & . & & & & . \\ . & . & & & & . \\ \psi_{r-1}^1 & \psi_{r-1}^2 & . & . & . & \psi_{r-1}^r \\ \psi_r^1 & \psi_r^2 & . & . & . & \psi_r^p \end{bmatrix}. \tag{4.16}$$

By using Eq. (4.13) we can find the coefficeint, Ψ^a, where $\mathbf{\Psi} = \left\{\mathbf{\Psi}^1, ..., \mathbf{\Psi}^p\right\}$, as follows

$$\mathbf{\Psi} = \mathbf{\Phi}^{\mathrm{T}}\mathbf{U} \tag{4.17}$$

Now let us suppose that an unknown displacement field $\hat{\mathbf{u}}$, with $\hat{\mathbf{u}} \notin \left\{\boldsymbol{u}^1, ..., \boldsymbol{u}^p\right\}$, corresponds to the set or parameters $\hat{\boldsymbol{\theta}}$, with $\boldsymbol{\theta}^1 < \hat{\boldsymbol{\theta}} \leq \boldsymbol{\theta}^p$ and $\hat{\boldsymbol{\theta}} \notin \left\{\hat{\boldsymbol{\theta}}^1, ..., \hat{\boldsymbol{\theta}}^p\right\}$. Similarly as done in Eq. (4.13), $\hat{\mathbf{u}}$ is found using the above POD-basis and is therefore approximated via Eq. (4.11) as

$$\hat{\mathbf{u}} \approx \hat{\psi}_1\mathbf{\Phi}^1 + \hat{\psi}_2\mathbf{\Phi}^2 + ... + \hat{\psi}_r\mathbf{\Phi}^r. \tag{4.18}$$

However, the coefficients $\hat{\mathbf{\Psi}} = \left\{\hat{\Psi}_1, \hat{\Psi}_2, ..., \hat{\Psi}_r\right\}$ are unknown and cannot be directly solved. Ly and Tran [43] therefore suggested to interpolate $\hat{\mathbf{\Psi}}$ from matrix $\mathbf{\Psi}$ through

$$\hat{\mathbf{\Psi}} = \mathbf{\Psi}\mathbf{N} \tag{4.19}$$

where $\mathbf{N}$ are the interpolants that can be derived from

$$\hat{\boldsymbol{\theta}} = \mathbf{\Theta}\mathbf{N}, \tag{4.20}$$

where matrix $\mathbf{\Theta} = \left\{\boldsymbol{\theta}^1, \boldsymbol{\theta}^2, ..., \boldsymbol{\theta}^p\right\}$ contains column vectors which are the different sets of parameters corresponding to the known solutions.

4.3 Moving least squares (MLS)

The PODI method makes use of the MLS interpolation technique. The PODI method was chosen by the CCM research group as it can deal with problems of arbitrary dimensionality and different size of data points [53]. The following derivation follows that closely in the works of Rama et al[53].

Let us consider a function $f(\boldsymbol{\theta})$ defined over the domain M where each point in M is not a associated with spatial coordinates but with a set of parameters $\boldsymbol{\theta}$ representing the charaterising properties of a problem's solution, for e.g. stiffness, anisotropy etc. A possible approximation for $f(\boldsymbol{\theta})$ is given by a polynomial $\mathbf{P}(\boldsymbol{\theta})$ and its non-constant coefficients $\mathbf{a}(\boldsymbol{\theta})$

$$f^h(\boldsymbol{\theta}) = \mathbf{P}(\boldsymbol{\theta}) \cdot \mathbf{a}(\boldsymbol{\theta}). \tag{4.21}$$

Now, let domain M be discretised by a finite number of parameter sets $\{\boldsymbol{\theta}^1, ..., \boldsymbol{\theta}^p\}$, the so-called *particles* scattered in domain M. Each particle is associated with a so-called *weight function* Φ of compact support. The size of the support can be individually defined for each particle $\boldsymbol{\theta}^I$, I= 1, p by ϱ_I, the so-called *influence radius* of Φ. The collection of particles with a non-vanishing weight function at point $\boldsymbol{\theta}$ constitutes its support denoted by Λ. Based on this set of particles, a weighted least square fit in the vicinity of point $\boldsymbol{\theta}$ can be constructed according to

$$J(\mathbf{a}(\boldsymbol{\theta})) = \sum_{I \in \Lambda} [\mathbf{P}\left(\boldsymbol{\theta}^I \cdot \mathbf{a}(\boldsymbol{\theta}) - f(\boldsymbol{\theta}^I)\right)]^2 \, \Phi\left(\frac{\boldsymbol{\theta} - \boldsymbol{\theta}^I}{\varrho_I}\right) \tag{4.22}$$

The unknown coefficients $\mathbf{a}(\boldsymbol{\theta})$ can be readily determined by minimising the squared and weighted error between the approximated and actual values of $f(\boldsymbol{\theta}^I)$ at each of the particles $\boldsymbol{\theta}^I \in \Lambda$. That is minimising the function J in Eq. (4.22), with respect to $\mathbf{a}(\boldsymbol{\theta})$. Finally, the coefficients $\mathbf{a}(\boldsymbol{\theta})$ are substituted into Eq. (4.21) and the approximation of function $f(\boldsymbol{\theta})$ takes the following form

$$f^h(\boldsymbol{\theta}) = \mathbf{P}(\boldsymbol{\theta}) \cdot \mathbf{M}^{-1}(\boldsymbol{\theta}) \sum_{I \in \Lambda} \left\{ \mathbf{P}(\boldsymbol{\theta}^I) \Phi\left(\frac{\boldsymbol{\theta} - \boldsymbol{\theta}^I}{\varrho_I}\right) f_I \right\}, \tag{4.23}$$

where $\mathbf{M}(\boldsymbol{\theta})$ is the so-called moment matrix of the weight function Φ

$$\mathbf{M}(\boldsymbol{\theta}) = \sum_{I \epsilon \Lambda} \mathbf{P}(\boldsymbol{\theta}^I) \mathbf{P}(\boldsymbol{\theta}^I) \Phi\left(\frac{\boldsymbol{\theta} - \boldsymbol{\theta}^I}{\varrho_I}\right) \tag{4.24}$$

and f_I are the so-called particle parameters.

With the refinement of the particle distribution, the support of the weight functions can be chosen smaller and the approximation $f^h(\boldsymbol{\theta})$ converges

for $\varrho_I \longrightarrow 0$ to the exact function $f(\boldsymbol{\theta})$. The minimum number of supporting particles for any point $\boldsymbol{\theta}$ is dictated by invertibility requirement of Eq. (4.24), that is the chosen basis polynomial. The smoothness of the MLS-approximation in Eq. (4.23) depends on the continuity of the basis polynomial $\mathbf{P} \in C^m(\Omega)$ as well as the weight function $\Phi \in C^l(\Omega)$ and it holds $f^h \in C^k$ with $k = \min(l, m)$ [53].

The chosen complete basis polynomial in two dimensions is given by

$$\mathbf{P}(\boldsymbol{\theta}) = [1, \theta^1, \theta^2], \tag{4.25}$$

and the weight function is based on a cubic spline

$$w(r) = \begin{cases} \frac{2}{3} - 4r^2 + 4r^3 & \text{for } |r| \leq \frac{1}{2} \\ \frac{4}{3} - 4r + 4r^2 - \frac{4}{3}r^3 & \text{for } |r| \leq \frac{1}{2} \leq 1. \\ 0 & \text{for } |r| > 1 \end{cases} \tag{4.26}$$

For the n-dimensional domain, the weight function can be constructed by the following expression:

$$\Phi\left(\frac{\boldsymbol{\theta} - \boldsymbol{\theta^I}}{\varrho_I}\right) = \sum_{k=1}^{n} w\left(\frac{\theta_k - \theta_k^I}{\varrho_I^k}\right) \tag{4.27}$$

Chapter 5

Inverse material parameter identification

The mechanics and constitutive equations that govern the passive behaviour of the myocardium were explored in the previous chapters. In addition, the fundamental cardiac mechanics principles and the methods used by the in-house software SESKA were outlined in Chapter 2.

Identification of material parameters can be obtained by using numerical simulations (e.g. FEM or EFG methods), in combination with measurements of variables, such as stresses, strains, pressure, volume or displacements, obtained from experimental testing. Such methods of solving for material parameters are referred to as inverse methods [1] or inverse problems [19]. This work uses the BLVM script developed by Guyon and Riche [19] which makes use of a least squares parameter estimation technique using the Levenberg-Marquardt algorithm.

This chapter will start by briefly introducing the read to the two broad categories of inverse methods. The underlying concepts of the Levenberg-Marquardt method are then outlined in the remainder of this chapter.

5.1 Inverse methods

Various inverse methods are presented in literature, however, Avril et al. [1] identified two broad categories, namely, updating and non-updating methods.

5.1.1 Non-updating methods

In non-updating methods of inverse modelling [1], simulated fields (e.g. strain, stress, pressure or volume fields) are computed from experimentally measured fields, using a constitutive material model, whose parameters are

to be identified and depend implicitly upon the latter. Equilibrium equations then provide the relationships that need to be solved, in order to obtain the sought after constitutive parameters. These methods are advantageous, as they are usually associated with faster computational time. However, such methods require full-field experimental data, with very sharp spatial resolution. As mentioned previously, there is usually shortage of suitable full-field experimental data [57].

5.1.2 Updating methods

These methods involve the computation of displacement, strain, stress, pressure or volume fields, via a numerical analysis, using initial guesses for material parameters. Actual material parameters are then identified by minimizing an objective cost function, which compares available measurements, to the corresponding simulated results. This method of finding constitutive parameters is advantageous, as full-field measurements are not required, rather, only a few measurements distributed across the volume of interest are necessary.

Updating methods however, involve iterative computational procedures and are thus computationally intensive. In addition, such methods are sensitive to measurement noise if based on scarce experimental data [1]. The process of the updating method of inverse modelling is shown schematically in Figure 5.1.

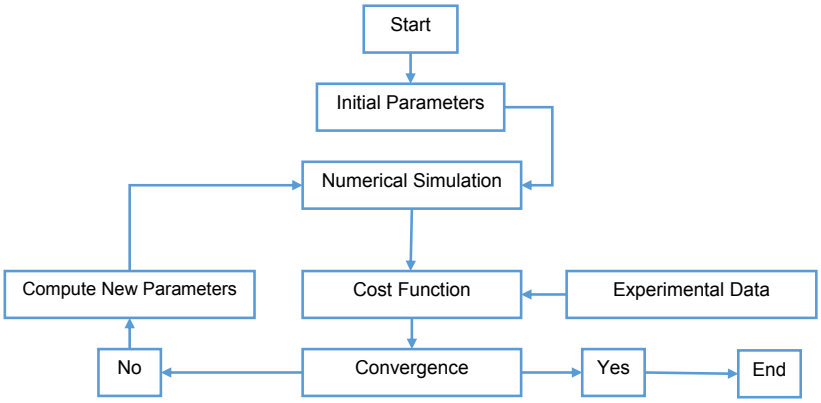

FIGURE 5.1: Flow chart illustrating the process of the updating method of inverse modelling.

Updating methods of inverse modelling will be used to solve for material parameters that best simulate the mechanical response of the human heart in this work. One reason for this choice of inverse method is due to

the fact that detailed full-field experimental data is scarce in the literature (such as stress, strain or displacement data).

5.2 Least squares parameter estimation

As mentioned previously, parameter estimation is the process of fitting a mathematical model to experimental data to determine unknown parameters of the model. The parameters are chosen so that the output of the model match, to a certain degree, observed experiments. The most general criterion to assess the worth of a set of parameters is the square of the Euclidean distance between the model and the experimental data [19].

As presented by Guyon et al. [19], we shall consider a vector $\mathbf{x}$ with parameters $\mathbf{x}_i$ to be in a n-dimensional closed and bounded hypercube, $S \subset \mathbb{R}^n$. Experimental data are written as a vector $\mathbf{z} \in \mathbb{R}^m$. The model $f(\mathbf{x})$ defines mapping $f : \mathbb{R}^n \to \mathbb{R}^m$ with f assumed to be twice continuously differentiable. Least squares parameters estimates are solutions of the unconstrained optimization problems,

$$\begin{aligned} min_{\mathbf{x}\in S} J(\mathbf{x}) &= \frac{1}{2}\sum_{i=1}^{m} w_i(f_i(\mathbf{x}_i) - \mathbf{z}_i)^2 \\ &= \frac{1}{2}(f(\mathbf{x}) - \mathbf{z})^T \mathbf{W}(f(\mathbf{x}) - \mathbf{z}) \\ &= \frac{1}{2}\|\mathbf{C}(f(\mathbf{x}) - \mathbf{z})\|^2 \end{aligned} \tag{5.1}$$

where the subscript i denotes components of a vector, $\mathbf{W} = \mathbf{C}^T\mathbf{C}$ is a $m \times m$ positive definite diagonal matrix of weights and $\|.\|$ is an L2 norm. Eq. (5.1) is sometimes referred as an output least squares minimization [19]. When solving the least squares problem (Eq. 5.1), two key issues need to be addressed:

- *Identifiability*: is the solution to Eq. (5.1) unique?
- *Sensitivity / Stability*: by how much will the parameter estimate change as a result of perturbation in the data or model?

Problems that are not identifiable or not stable are said to be ill-posed. Against non-uniqueness, a second, regularizing, minimization is used

$$min_{\mathbf{x}\in\chi}\frac{1}{2}\|\mathbf{x}\|^2 \tag{5.2}$$

Eq. (5.1) and (5.2) can then be applied to four types of functions, namely, injective, surjective, general linear and non-linear functions. The reader is referred to the work by Guyon et al. [19] for a more detailed treatment on this.

Another important concept in least square estimate problems is "sensitivity". Calculations may be corrupted by experimental and numerical errors, inducing model and data changes. The generic term "sensitivity" describes the influence of the errors on the identified model. Sensitivities concern either a change of least squares norm or a change of parameter estimate. Sensitivities are calculated, first of all, in order to have a level of confidence in an identified model. But high sensitivities are also hints that numerical difficulties might occur during identification. It is therefore common practice to select experimental data as to minimize sensitivities [19].

5.3 Levenberg-Marquardt method

The Levenberg-Marquardt algorithm is an iterative technique that locates the minimum of a function that is expressed as the sum of squares of non-linear functions. It has become a standard technique for non-linear least-squares problems and can be thought of as a combination of steepest descent and the Gauss-Newton method. The Levenberg-Marquardt family of algorithms have emerged as robust methods for non-linear least squares minimizations [19]. The Levenberg-Marquardt algorithm is perhaps the most common method for non-linear least-squares minimization [72] [42] [19]. The LM is essentially used to find the minimum of a function that is a sum of squares of non-linear functions. This work makes use of the Levenberg-Marquardt script developed by Guyon and Riche and as described in their work [19].

LM methods are classically derived by sequentially linearizing $f(\mathbf{x})$ in Eq. (5.1). In order to maintain validity of the linearization, move limits on the variable $\mathbf{x}$ are added. At iteration k, the following is solved,

$$\begin{cases} \min_{\mathbf{x}\in S} J_L(\mathbf{x}) = \dfrac{1}{2}\left\|(f(\mathbf{x}_k) + \nabla f(\mathbf{x}_k)(\mathbf{x}_{k+1} - \mathbf{x}_k) - \mathbf{z})\right\|^2 \\ \text{such that } g(\mathbf{x}) = \dfrac{1}{2}\left\|\mathbf{x}_{k+1} - \mathbf{x}_k\right\|^2 - \delta_k < 0 \end{cases} \tag{5.3}$$

where $\nabla f(\mathbf{x}_k)$ is the gradient of the function f with respect to $\mathbf{x}$ and is called the Jacobian, $\mathbf{J} = \nabla f(\mathbf{x}_k)$. First order necessary and sufficient conditions of optimality for Equation 5.3 are the basis for the Levenberg-Marquardt algorithms,

$$(\nabla f(\mathbf{x}_k)^T \nabla f(\mathbf{x}_k) + \lambda_k \mathbf{I})(\mathbf{x}_{k+1} - \mathbf{x}_k) = -\nabla f(\mathbf{x}_k)^T (f(\mathbf{x}_k) - \mathbf{z}). \tag{5.4}$$

λ_k is the Lagrange multiplier associated to the constraint of Eq. (5.3). The Hessian matrix is given by

$$\mathbf{H} = \mathbf{J}^T\mathbf{J} = \nabla f(\mathbf{x}_k)^T \nabla f(\mathbf{x}_k) \tag{5.5}$$

and is the second derivative of f with respect to vector $\mathbf{x}$. The parameter vector, $\mathbf{x}_{k+1}$, is found by rearranging Eq (5.5)

$$\mathbf{x}_{k+1} = \mathbf{x}_k - (\nabla f(\mathbf{x}_k)^T \nabla f(\mathbf{x}_k) + \lambda_k \mathbf{I})^{-1} \nabla f(\mathbf{x}_k)^T (f(\mathbf{x}_k) - \mathbf{z}). \tag{5.6}$$

The equations presented so far provide the basis for how the LM method operates. The next two subsections will look at two important concepts which the LM method employs, namely scaling and handling boundary constraints.

5.3.1 Scaling

Scaling is critical for problems where model parameters have different values. The main relations underlying scaling and reinterpret singular value analysis when scaling is performed will be presented. This sub-section closely follows the work by Guyon and Riche [19]. Scaled variables $\mathbf{x}$ are written for each iteration k,

$$\mathbf{D}_k \bar{\mathbf{x}} = \mathbf{x}, \tag{5.7}$$

where $\mathbf{D}_k$ is a positive definite diagonal matrix. Elements of $\mathbf{D}_k$ are taken as one of two choices. The first choice occurs when we have insight of typical values of the parameters then the starting set of parameters as set along the diagonal of $\mathbf{D}_k$. The second choice occurs when not enough is known about the problem, then scaling is performed in accordance with

$$\mathbf{D}_{k,i} = \|(\nabla f(\mathbf{x}_k))_i\|^{-1} \tag{5.8}$$

where $i \in \{1, ..., n\}$. An unique scenario can occur when one of the entries of the Jacobian is equal to zero which results in instabilities [19]. This problem can be solved by replacing the zero with the value from the previous iteration, $k-1$, of the same entry. The scaled version of Levenberg-Marquardt is obtained by rewriting $g(\mathbf{x})$ of Eq. (5.3) in terms of the scaled variables,

$$\begin{cases} \min_{\mathbf{x} \in S} J_L(\mathbf{x}) = \dfrac{1}{2} \|(f(\mathbf{x}_k) + \nabla f(\mathbf{x}_k)(\mathbf{x}_{k+1} - \mathbf{x}_k) - \mathbf{z})\|^2 \\ \text{such that } \bar{g}(\bar{\mathbf{x}}) = \dfrac{1}{2} \|\bar{\mathbf{x}}_{k+1} - \bar{\mathbf{x}}_k\|^2 - \delta_k < 0. \end{cases} \tag{5.9}$$

The derivatives with respect to the unscathed variables can be written as

$$(\mathbf{D}_k^T \nabla f^T \nabla f \mathbf{D}_k + \lambda_k \mathbf{I})(\bar{\mathbf{x}}_{k+1} - \bar{\mathbf{x}}_k) = -\mathbf{D}_k^T \nabla f^T (f(\mathbf{D}_k \bar{\mathbf{x}}_k) - \mathbf{z}) \tag{5.10}$$

Finally multiplying by $(\mathbf{D}_k^T)^{-1} = \mathbf{D}_k^{-T}$ and expressing in terms of $\mathbf{x}$, we obtain a scaled version of Levenberg-Marquardt

$$(\nabla f^T \nabla f + \lambda_k \mathbf{D}_k^{-T} \mathbf{D}_k^{-1})(\mathbf{x}_{k+1} - \mathbf{x}_k) = -\nabla f^T (f(\mathbf{x}_k) - \mathbf{z}) \tag{5.11}$$

Eq. (5.11) forms an important part of the Levenberg-Marquardt script by Guyon and Riche [19].

5.3.2 Handling boundary constraints

The Kuhn-Tucker conditions (also known as the Karush-Kuhn-Tucker conditions) are first order necessary conditions for a solution in non-linear programming to be optimal, provided that some regularity conditions are satisfied. These boundary constraints are essential in the LM algorithm because they restrict movement of the algorithm over specific parametric range. The Kuhn-Tucker conditions are used to handle the variable bounds of the constrained problem,

$$\begin{cases} \min_{d \in S} J_L(\mathbf{x}) = \dfrac{1}{2} \left\| (f(\mathbf{x}_k) + \nabla f(\mathbf{x}_k) d - \mathbf{z}) \right\|^2 \\ \text{such that } \dfrac{1}{2} \left\| d \right\|^2 - \delta_k \leq 0 \\ \mathbf{x}_k + d - \mathbf{x}_{max} \leq 0 \\ -\mathbf{x}_k - d + \mathbf{x}_{min} \leq 0 \end{cases} \tag{5.12}$$

where $d = \mathbf{x}_{k+1} - \mathbf{x}_k$. If we let $\mu \in \mathbb{R}^n$ and $\gamma \in \mathbb{R}^n$ denote Lagrange multipliers associated to upper and lower bounds, respectively, then the Kuhn and Tucker conditions for the constrained problem in Eq. (5.12) become

$$(\nabla f(\mathbf{x}_k)^T \nabla f(\mathbf{x}_k) + \lambda_k \mathbf{I}) d + \mu - \gamma = -\nabla f(\mathbf{x}_k)^T (f(\mathbf{x}_k) - \mathbf{z}) \tag{5.13}$$

$$\mu_i (\mathbf{x}_{k,i} + d_i - \mathbf{x}_{max,i}) = 0 \tag{5.14}$$

$$\gamma_i (-\mathbf{x}_{k,i} - d_i + \mathbf{x}_{min,i}) = 0 \tag{5.15}$$

$$\mu \geq 0 \tag{5.16}$$

$$\gamma \geq 0 \tag{5.17}$$

$$\mathbf{x}_k + d - \mathbf{x}_{max} \leq 0 \tag{5.18}$$

$$-\mathbf{x}_k - d + \mathbf{x}_{min} \leq 0 \tag{5.19}$$

The Levenberg-Marquardt algorithm satisfies the Kuhn-Tucker conditions by decomposing into two steps. First, a decision is made on which constraint is active. Next, Eq. (5.13) to (5.15) are solved. Eq. (5.16) to (5.18) are checked based on the observed results. If any of the conditions are violated, a new decision is made on which constraint is active and the process is repeated. This process is also known as the Active Set Method.

Once a choice has been made about active constraints, Eq. (5.14) and (5.15) imply,

$$\text{if } \mu_i \neq 0 \Rightarrow \gamma_i = 0 \text{ , } d_i = \mathbf{x}_{max,i} - \mathbf{x}_{k,i} \tag{5.20}$$

$$\text{else if } \gamma_i \neq 0 \Rightarrow \mu_i = 0 \text{ , } d_i = \mathbf{x}_{min,i} - \mathbf{x}_{k,i} \tag{5.21}$$

$$\text{else } \mu_i = 0 \text{ , } \gamma_i = 0 \Rightarrow d_i \text{ unknown.} \tag{5.22}$$

The remaining unknown parametrs are then solved using Eq. (5.20).

The algorithm by Guyon and Riche [19] uses the following rules for adding or deleting constraints from the active set:

- if there are violated constraints add the most critical to the active set,
- else if there are negative μ_i's or γ_i's, randomly delete one of the associated constraints from the active set,
- else stop. The Kuhn-Tucker conditions are satisfied.

Chapter 6

Methodology

The cardiac models developed in this study simulate a functioning human heart. The two cardiac models were created using a pre-processing software called GID version 12.0.7. The first model is a left ventricle (LV) model while the second is a bi-ventricle (BV) model.

This chapter will begin by describing the methodology for the development of the numerical models for the LV and BV which are then benchmarked to data from literature. The initial calibration of the anisotropic material parameters, a_1 to a_6, are then presented. The details on how the databases were constructed for the LV and BV models are also presented. Finally, the methodology for the generation of the EFG reference solution and the BLVM-PODI parameter optimization is described. Figure 6.1 provide a concise flow chart which outlines the overall methodology for the model development and database construction employed in this work.

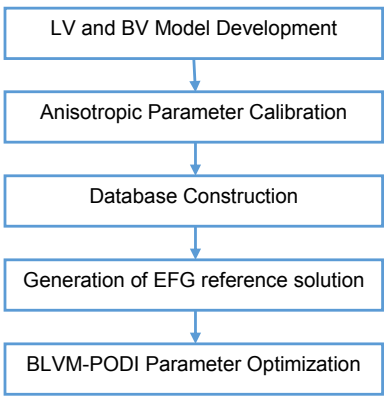

FIGURE 6.1: Methodology flow chart

It should be noted that no programming was undertaken by the author and the in-house codes used in this work were developed by the CCM research group. More details on SESKA and ORION are provided in Appendix A and B respectively.

6.1 Introduction to biomechanics modelling

As engineers, we seek to develop mathematical models which allow us to predict a system response to external stimuli. In this study we want to predict the deformations that occur when the cardiac model is subjected to a set of prescribed pressures. The general procedure for building a practical model of a material body can be described as consisting of four major steps.

First, we must identify the forces and fields which we would like to model. In cardiac mechanics, there are several forces and fields which influence the behaviour of cardiac tissue. A model that captures the coupling between all of these fields would be complex. Therefore, in this study we will select the forces and fields which are of primary interest, these being the pressure and volume changes which are obtained from the stress, strain and displacement solution fields.

Second, the balance laws and constitutive model must be formulated given the relevant variables and material characteristics determined in step one. The result of this second step is a set of mathematical equations describing the connections between the selected forces and fields in the material body. These were highlighted in Chapter 2.

Third, a strategy for parametrizing the constitutive model must be developed. This involves the selection of an appropriate experimental method and the derivation of working equations particular to that experiment. These were also highlighted in Chapter 2.

Fourth, a numerical solution must be obtained in order to apply the mathematical model to conditions mimicking real-world systems. The mathematical equations derived in step two are often complex and an analytical solution may be difficult to obtain. In addition, the geometry and boundary conditions found cardiac mechanics applications make an analytical solution for some constitutive models very complex or even impossible.

Numerical techniques, such as the finite element method (FEM), are generally used to solve the set of partial differential equations which make up the constructed model. Meshfree methods such as the element free Galerkin (EFG) method can also be used. One of the most critical steps in biomechanical modelling is the choice of a suitable constitutive law and the calibration of its parameters for the structure under consideration, in this case the heart.

6.2 Left ventricular model development

To reduce the complexity of the computational model, various studies consider the LV only. In Wenk et al. [77] and Niederer et al. [49], the LV was idealized using an ellipsoidal geometry. In total the LV discretized model in this work comprised of 937 nodes and 3860 4-node tetrahedra elements. As can be seen in Figure 6.2, the base of the LV is shown at the top by the opening from the aorta while the apex is shown at the opposite end.

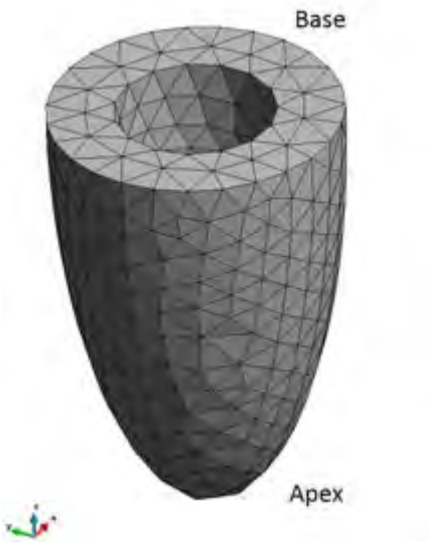

FIGURE 6.2: Meshed LV model

Geometry

A common simplification of the left ventricle geometry is a truncated ellipsoid [57]. The LV model was created by bisecting an ellipsoid volume in exactly half along its major axis. The volume of an ellipsoid can be calculated by

$$V = \frac{4}{3}\pi abc \tag{6.1}$$

where a, b and c are shown in Figure 6.3.

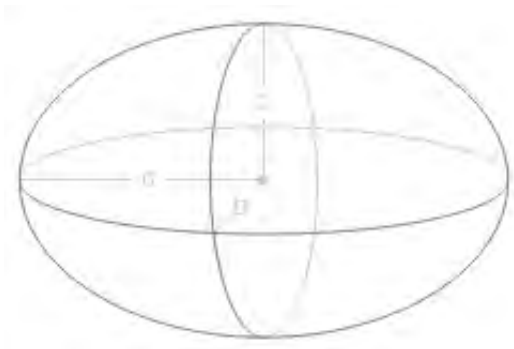

FIGURE 6.3: Ellipse volume representation

The base radius for the LV are in accordance with experimental data for human hearts found in the literature of Stolzmann et al. [69] and Simmons, Gillin, and Jeremy [61]. As shown in Figure 6.4, a base radius of 28.21mm was used. Yiu et al. [82] found that the LV length to base width ratio (L/D) was in the magnitude range of between two and three. A height for the LV of 73.5mm was chosen and this equates to a L/D ratio of 2.6 which satisfies the finding of Yiu et al. [82]. The wall thickness of 12.71mm is in accordance with the findings of Sandstede et al. [60] and Sommer et al. [67].

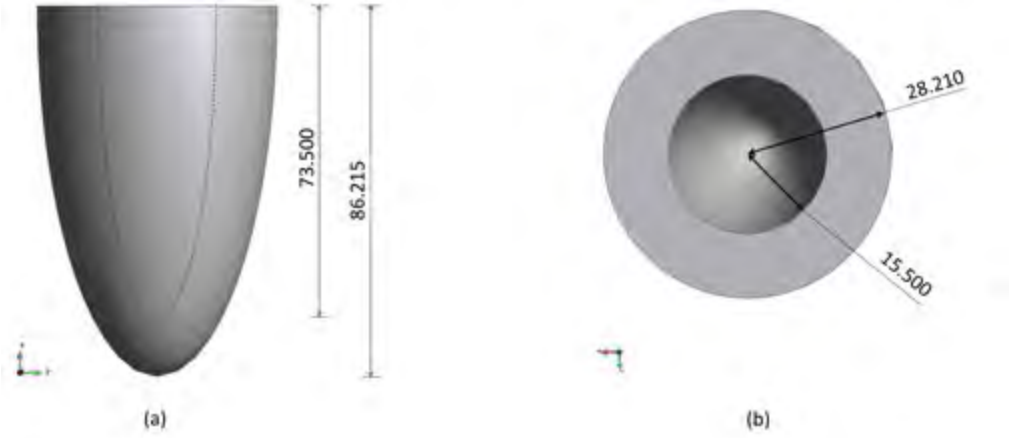

FIGURE 6.4: Geometrical layout of the LV model

If we now apply Equation 6.1 with $a = 7.35cm$ and $b = c = 1.55cm$ then the half ellipsoidal volume, V, is approximately $37cm^3$. This represents the LV volume of a human heart at the start of the diastolic filling phase, which is in accordance with Sandstede et al. [60] and Hudsmith et al. [23].

Boundary conditions

In order to model the cardiac cycle, it is essential to specify boundary conditions that reflect the physiological function as close as possible, without introducing unnecessary complications. These boundary conditions can be divided into two categories: Dirichlet and Neumann. Dirichlet boundary conditions are required to prevent rigid body motion and to constrain the base of the heart. Neumann boundary conditions are required to simulate the blood filling the cavity which causes pressure to act on the endocardium of the left ventricle. The boundary conditions applied to the LV model during the diastolic filling phase will now be presented.

A surface pressure of 1.5 kPa was applied to the inner endocardium surface of the LV as shown in Figure 6.5a. This is in accordance with the literature of Guccione et al. [18]. The surface of the base was fixed in the Z direction such that $u_z = 0$ as illustrated in 6.5b. An elastic line boundary condition was applied to the inner ring and outer ring of the base as shown

in Figure 6.5c. The purpose of this condition is to elastically restrain the rotational movement in the circumferential direction of the heart base but allowing free radial movement. This is achieved by adding a penalty term to the variational formulation (Eq. (2.76)) of the following form:

$$\oint_{C_D} \beta \, (\mathbf{u} \cdot d\mathbf{S}) \, d\mathbf{S} \cdot \delta\mathbf{u} \tag{6.2}$$

where $d\mathbf{S}$ denotes a line element in the undeformed configuration and β is a penalty factor.

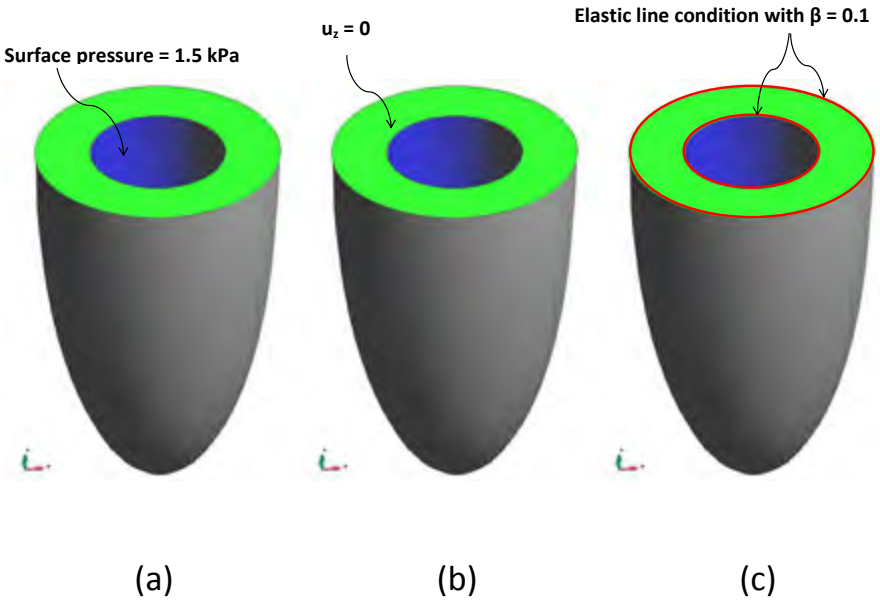

FIGURE 6.5: Boundary conditions enforced on the LV model during diastolic filling.

Material parameters and fibre distribution

The material parameters in Table 6.2 were kept constant for all of the LV simulations. The parameter values used for the fibre and sheet angles are in accordance with the findings of Rohmer, Sitek, and Gullberg [54] and are given in Table 6.1. In Rohmer, Sitek, and Gullberg [54], a human heart left ventricle was scanned and its fibre angles averaged for different zones of the left ventricle. In order to simplify the procedure of the fibre assignment on the LV geometry, the base angles were used and assigned to the whole of the geometry. The fibre orientation is computed using an algorithm developed by Wong and Kuhl [78]. The two associated cross-fibre directions are then found afterwards using the Moving Least Squares method.

TABLE 6.1: Constant fibre and sheet angles for LV database

Parameter	**Value**
F_{epi}	$-57°$
F_{endo}	$59°$
S_{epi}	$45°$
S_{endo}	$-10°$

Figure 6.6 provides a post-processed visualization of the fibre and sheet angles for the LV model. Figure 6.6a shows arrows representing the fibre angle. Figure 6.6b shows the sheet normal and Figure 6.6c shows the sheet angle.

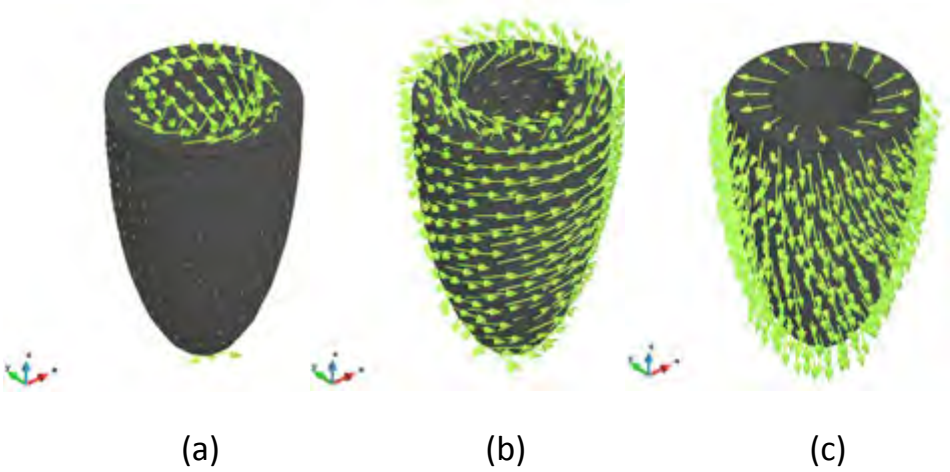

FIGURE 6.6: Post-processed visual representation of the fibre angle, sheet angle and sheet normal for the LV model

The previously calibrated parameters describing the anisotropic material composition of the myocardium (see Section 6.4) were kept constant and are shown in Table 6.2. Only the values of parameter A in the orthotropic material law (Eq. 3.4) were varied to construct the database for the LV. More details on the varying material parameters will be provided in section 6.5.

TABLE 6.2: LV material parameters

Parameter	Value
A_{Comp}	100 kPa
a_1	12.699
a_2	-8.3616
a_3	-8.5768
a_4	11.217
a_5	14.251
a_6	9.1531

6.3 Bi-ventricular model development

As described for the LV model, the left ventricle in the BV model was idealized using an ellipsoidal geometry and the geometry is exactly the same as the LV model. In total the BV discretized model comprised of 956 nodes and 3680 4-node tetrahedra elements. It must be noted that the BV model was not created by the author and was provided by the CCM research group at the University of Cape Town.

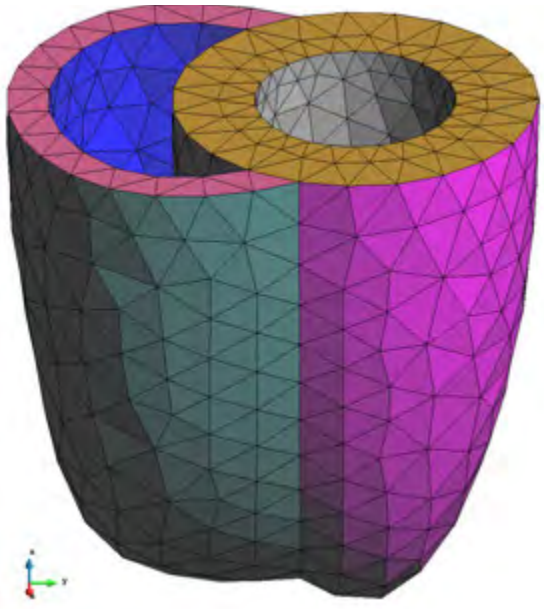

FIGURE 6.7: Meshed BV model

Geometry

The left ventricle of the BV model is identical in geometry to the LV model as described already. The RV geometry was setup such that the end diastolic volume equalled that of a human as reported by Sandstede et al. [60] and Hudsmith et al. [23]. The geometry of the BV model is illustrated in Figure 6.8.

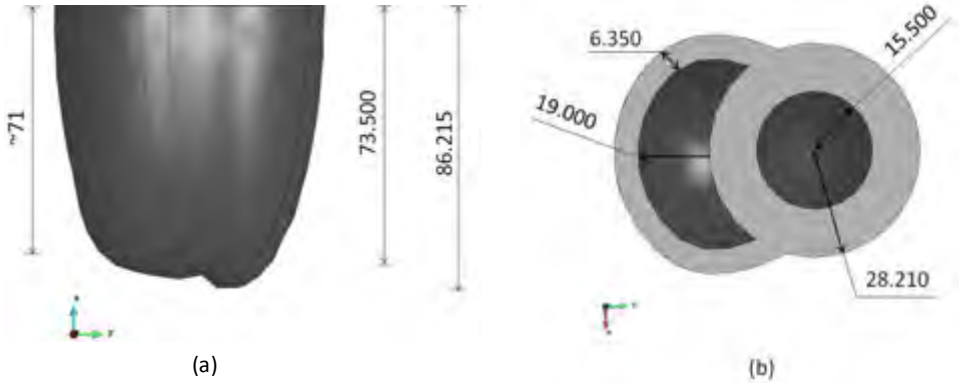

FIGURE 6.8: Geometrical layout of the BV model

Boundary conditions

The boundary conditions applied to the BV model are similar to what was applied to the LV model. Similar to the LV model, the base of the BV is constrained at the top by the opening from the aorta while the apex is positioned at the opposite end. A surface pressure of 1.5 kPa was applied to the inner endocardium surface of the LV as shown in Figure 6.9a. This is in accordance with the literature of Guccione et al. [18]. A surface pressure of 1 kPa was applied to the inner surface of the RV. The surface of the base was fixed in the Z direction such that $u_z = 0$ as illustrated in 6.9b. An elastic line boundary condition of 0.1 was applied to the inner and outer rings of the base as shown in Figure 6.9c.

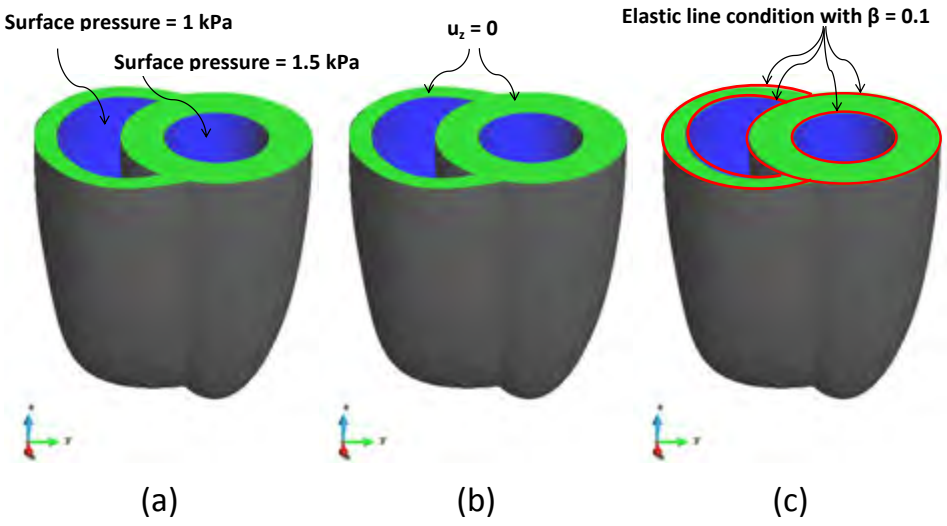

FIGURE 6.9: Boundary conditions enforced on the BV model during diastolic filling.

Material parameters and fibre distribution

The material parameters in Table 6.4 were kept constant for all the BV simulations. Similar to the LV, the values used for the fibre and sheet angles are in accordance with the findings of Rohmer, Sitek, and Gullberg [54] listed in Table 6.1. It was decided not to vary the sheet angle values during the creation of the database because this drastically grew the required number of simulations for the database creation. Table 6.3 shows the sheet angle values which were kept constant for all of the simulations of the BV. Figure 6.10 provides a visualization of the fibre and sheet angles for the BV model. Figure 6.10a shows arrows representing the fibre angle. The fibre angle was varied for each simulation in order to create the database. More details on the varying fibre angles will be provided in section 6.5. Figure 6.10b shows the sheet angle and Figure 6.10c shows the sheet normal.

TABLE 6.3: Constant sheet angles for BV database

Parameter	Value
S_{epi}	$45°$
S_{endo}	$-10°$

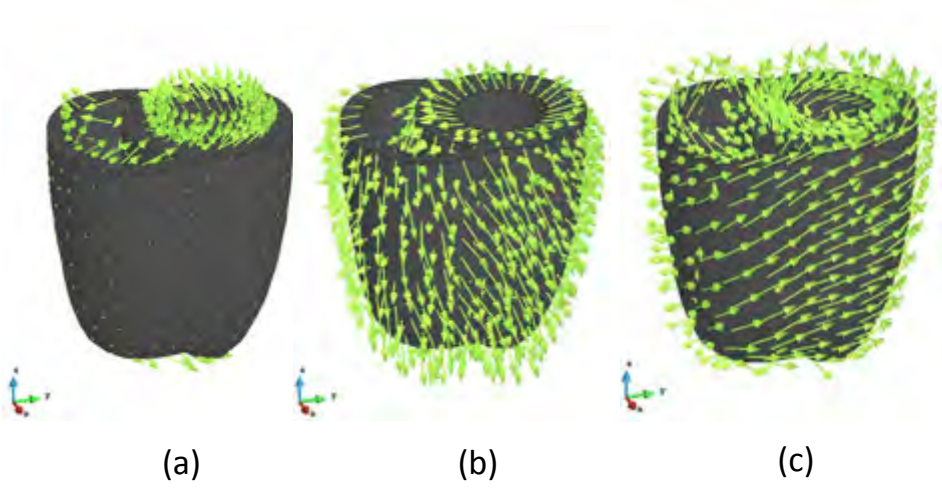

FIGURE 6.10: Post-processed visual representation of the fibre angle, sheet angle and sheet normal for the BV model

Parameter A, F_{epi} and F_{endo} were varied to construct the database. Details on the database construction will be provided in Section 6.5.

TABLE 6.4: BV material parameters

Parameter	**Value**
A_{Comp}	100 kPa
a_1	12.699
a_2	-8.3614
a_3	-8.561
a_4	11.217
a_5	14.251
a_6	9.1529

6.4 Initial calibration of anisotropic material parameters

The shear properties of the myocardium from the triaxial simple shear tests performed by Sommer et al. [67] on small cubic specimens excised from a human heart were used to calibrate the material properties a_1 to a_6.

The experimental data by Sommer et al. [67] comprised of human myocardial tissue from 28 subjects (11 women and 17 men) with an age of 61 $\pm$ 15 years (range 31 - 93). Triaxial shear properties in all three orthogonal orientations were determined by simple shear tests on three cubic specimens taken from a region adjacent to the biaxially tested specimens. Six possible simple shear modes for an orthotropic myocardium cube were defined with respect to the fibre f_0, sheet s_0, and sheet-normal direction n_0. The six shear modes are shown in Figure 6.11. The modes are ij and i ; $j \in$ {F, S, N}, where i denotes the normal vector of the face that is shifted by the simple shear and j denotes the direction in which the face is shifted.

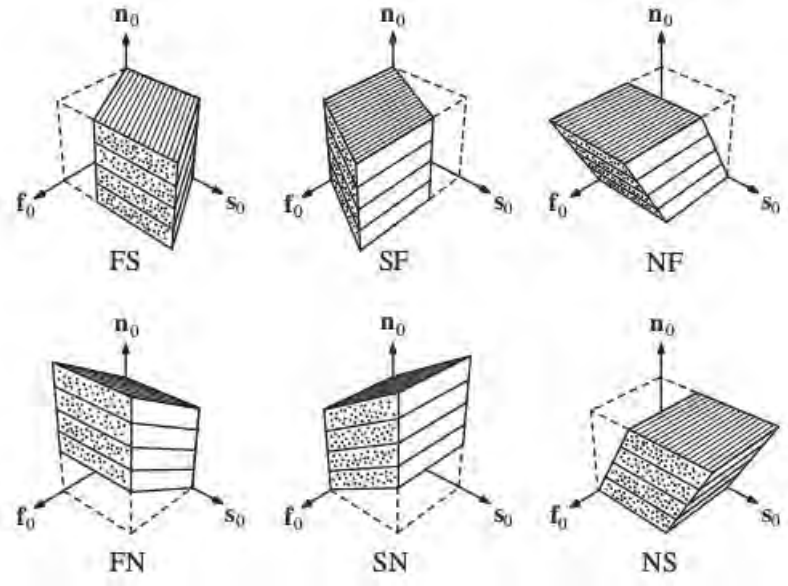

FIGURE 6.11: Six possible simple shear modes for an orthotropic myocardium cube as depicted in the work by "Biomechanical properties and microstructure of human ventricular myocardium"

Figure 13 from Sommer et al. [67] show graphs of average 'elastic' triaxial shear stress versus 'amount of shear' behaviour of all the considered human myocardial specimens subjected to each shear mode (FS, FN, SF, SN, NF, NS). The material parameters were calibrated by running inverse material parameter optimization coupling BLVM with SESKA. This iterative procedure involved running simulations corresponding to the shear experiments of Sommer et al [67]. The final stress-strain graphs resulting from the SESKA simulations for the calibration are shown in Figure 6.12. The lower, upper and mean values were extrapolated from Figure 13 of Sommer et al [67]. As can be seen, the SESKA graph closely fits the mean graph.

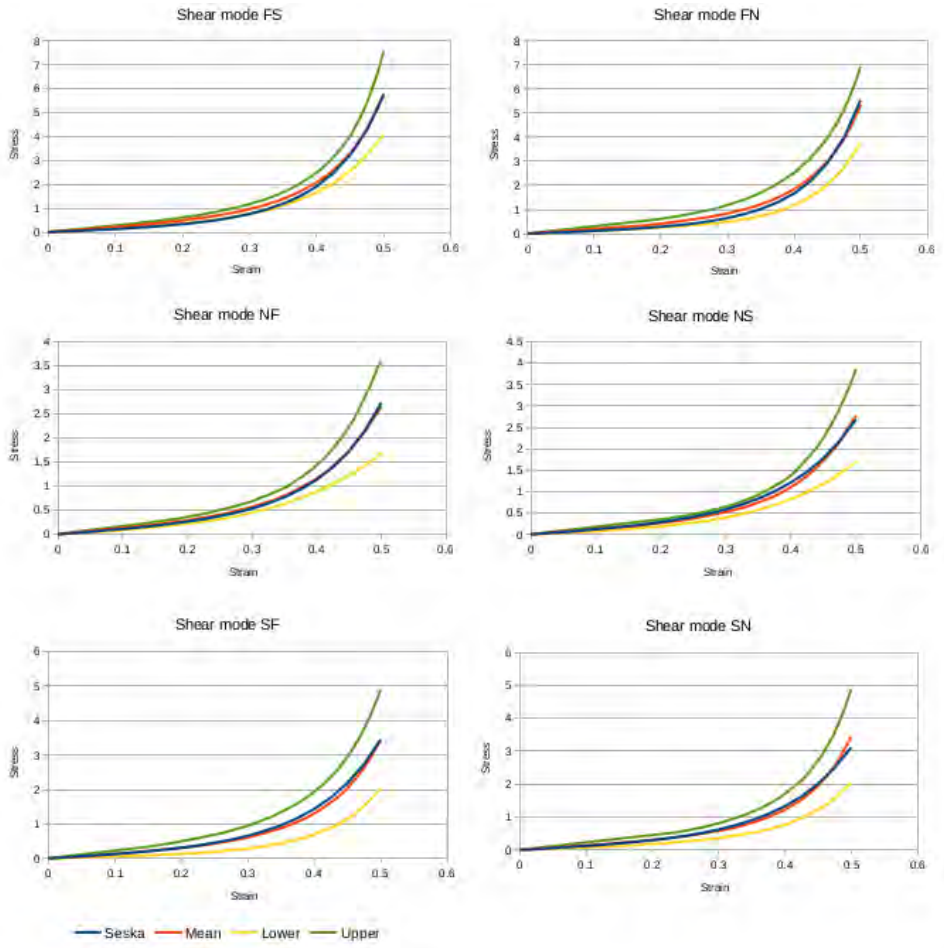

FIGURE 6.12: Stress strain graphs obtained from the SESKA simulations for the shear cube calibrations.

It should be noted that the calibration of the parameters a_1, a_2, a_3, a_4, a_5 and a_6 were calibrated by the CCM research group based on the experimental data from the work by Sommer et al. [67].

6.5 Database construction

The in-house code SESKA was used to simulate the cardiac mechanics of the diastolic filling phase. Various simulations were run and each provided a dataset which consists of solution fields, such as displacement, stress and strain. These groups of datasets make up what is called the database. This section will describe the process undertaken for the LV and BV database construction.

As mentioned previously, the cardiac simulations were run using an in-house code called SESKA. Each simulation represent a dataset and the group of datasets make up the database. Each dataset is characterized by a unique set of parameter values (for e.g. A, f_{epi} and f_{endo}). Each dataset is

stored off-line for each time-step of the simulation. There were two separate databases constructed, one for the LV model and one for the BV model.

The upper and lower bounds of the end-diastolic volume (EDV) specified in Table 6.5 were used to determine the upper and lower bounds of parameter A for the purpose of the database construction which are listed in Table 6.6 for the LV and Table 6.8 for the BV. These bounds are in accordance with the ranges provided in Table 1 of Sandstede et al. [60].

TABLE 6.5: Upper and lower bound EDV values

	Lower bound	Upper bound
Left ventricle EDV (mL)	81	135
Right ventricle EDV (mL)	84	146

Regarding the database itself, a basic database management system was utilized where all datasets were stored locally on a hard-drive and structured into folders. The entry of each dataset was then registered in a comma-separated values (CSV) file, which can be generated by an editor program or a spreadsheet software. The latter will only be used to store the required parameter values (such as A, f_{epi} and f_{endo}) along with the location of the dataset on the drive.

The next two subsections will provide details on how the material parameters were varied for the LV and BV databases respectively.

6.5.1 LV database construction

For the LV database construction, only the material parameter A was varied.

TABLE 6.6: LV EDV for limiting Parameter A

	Lower bound	Upper bound	Dataset increment
Parameter A	0.020	0.280	0.02
EDV (mL)	134.04	81.62	-

The database was constructed by running conventional full-scale simulations in increments of A = 0.02 between the lower bound and the upper bound (i.e. from A = 0.02 to A = 0.28). Accordingly, there were a total number of 14 datasets available for the calculation and their respective EDV are shown in Table 6.7. As can be seen in Table 6.7 the EDV volumes are within the EDV bounds shown in Table 6.5. Figure 6.13 shows the trend of the parameter A within the LV database and their respective EDV. As parameter A values increase in increments of 0.02 the EDV decreases.

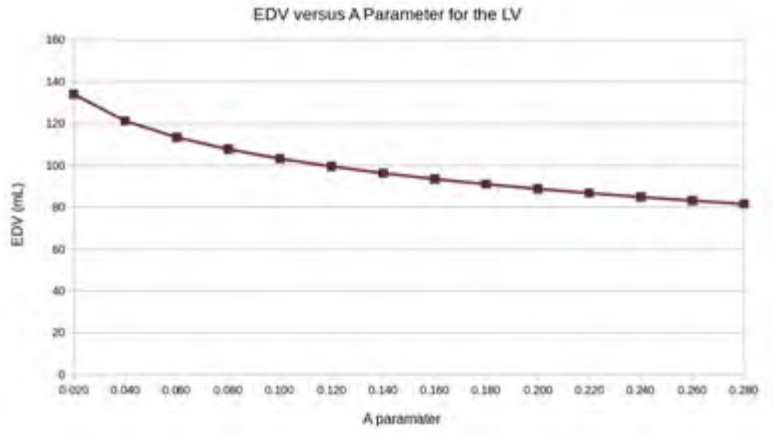

FIGURE 6.13: EDV versus Parameter A from the LV database.

TABLE 6.7: Resulting LV EDV for varying Parameter A

Parameter A	0.020	0.040	0.060	0.080	0.100	0.120	0.140
EDV (mL)	134.04	121.23	113.43	107.75	103.26	99.53	96.34

Parameter A	0.160	0.180	0.200	0.220	0.240	0.260	0.280
EDV (mL)	93.55	91.07	88.84	86.80	84.94	83.22	81.62

Figure 6.14 shows the LV pressure versus volume for the various parameter A within the database. As can be seen, the pressure volume graph (Fig 6.14) is similar in shape to the "period of diastolic filling" of the pressure volume graph in textbook literature Guyton and Hall [20] which is also shown in Figure 6.15. This formed part of the verification process when post-processing the simulation results from SESKA to ensure simulations within the database ran as they were expected to.

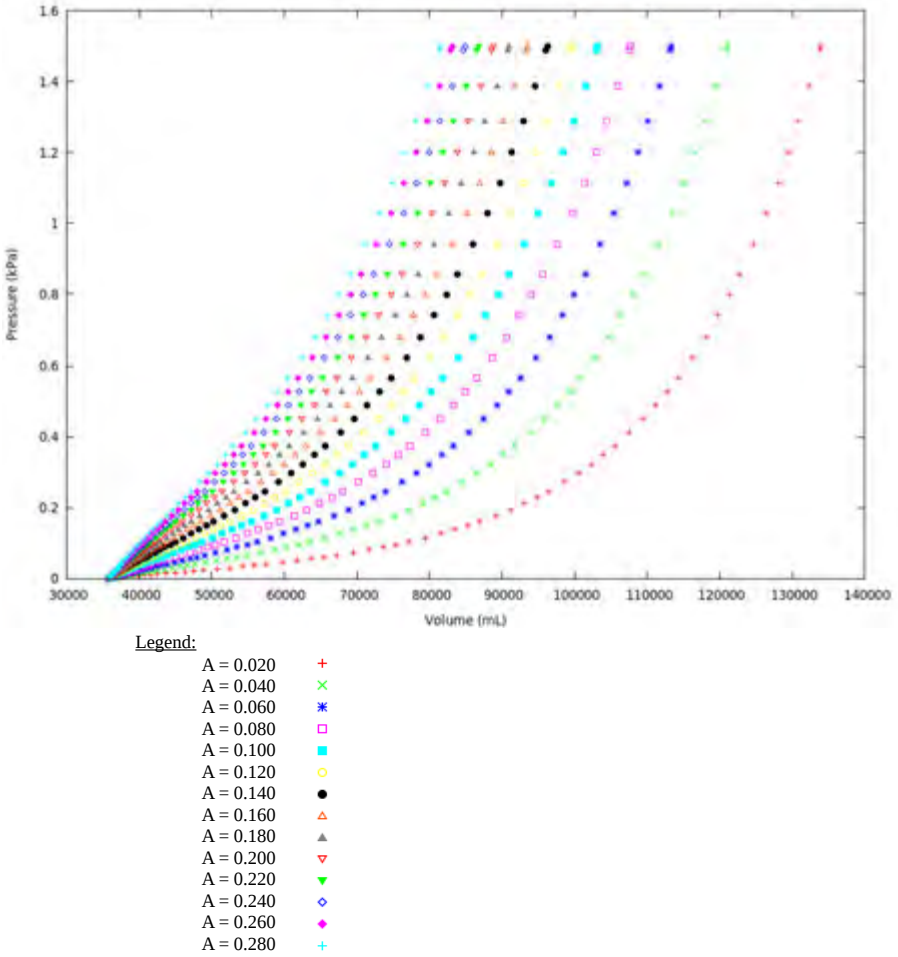

FIGURE 6.14: LV Pressure-volume graphs for each parameter A within the LV database.

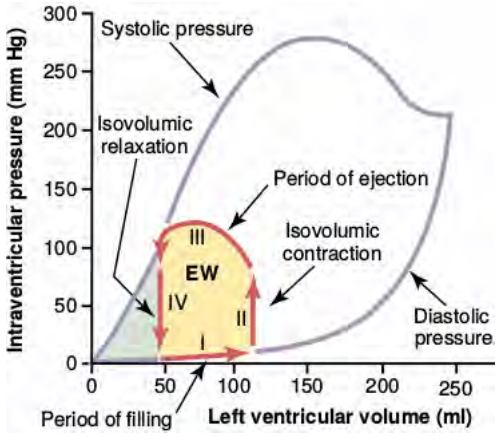

FIGURE 6.15: Pressure-volume graphs adopted from Guyton and Hall [20]

6.5.2 BV database construction

For the BV database construction, a similar process was employed as that of the LV database construction except here the material parameters f_{epi} and f_{endo} were also varied in addition to parameter A. The respective A, f_{epi}

and f_{endo} for the upper and lower bound EDV of the BV are given in Table 6.5. The database was then created by varying each of the three material parameters with each others respective increments such that all possible parameter combinations were achieved. The limiting ranges of A, f_{epi} and f_{endo} and the dataset increments are shown in Table 6.8.

TABLE 6.8: Limiting values and increments for A, f_{epi} and f_{endo}

	Lower bound	Upper bound	Dataset increment
Parameter A	0.040	0.220	0.0225
f_{epi}	-66°	-48°	2.25°
f_{endo}	55°	89°	4.25°

Accordingly, the BV database consisted of 729 datasets. In a similar fashion to the LV, checks were conducted on randomly selected pressure volume graphs for the LV and RV of the simulation datasets within the BV database to verify the shape and trend of the graphs and also to ensure the simulation ran as it was expected to. The sheer scale and total number of dataset combinations make it impractical to include all of these graphs in this work but a randomly selected parameter graph have been shown in Figure 6.16 for the LV and Figure 6.17 for the RV of the BV model.

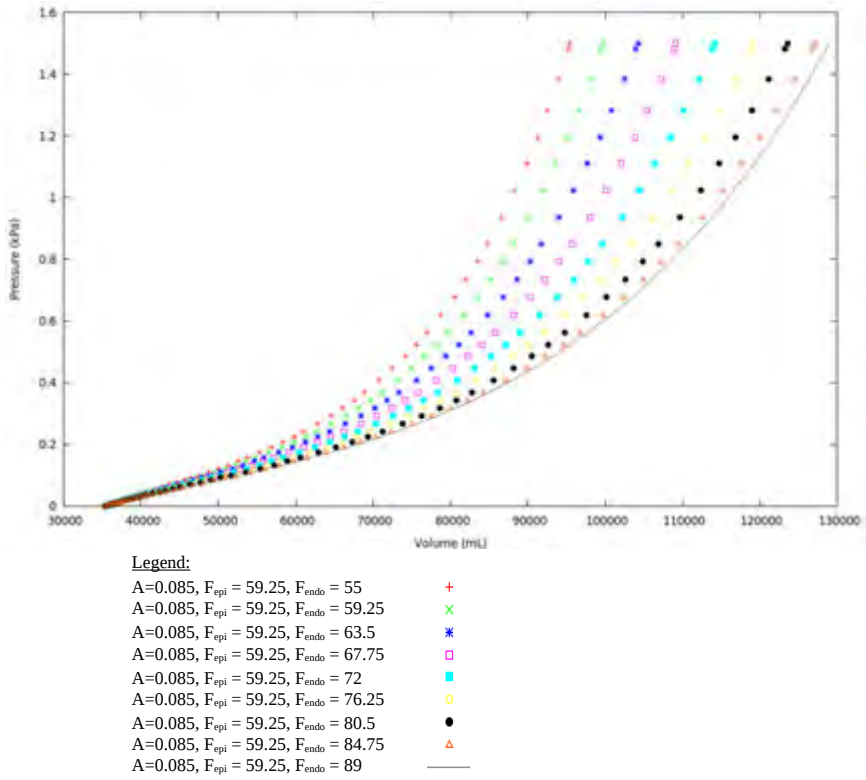

FIGURE 6.16: LV Pressure-volume graphs for A = 0.085, f_{epi} = 59.25 and varying f_{endo} parameter within the BV database.

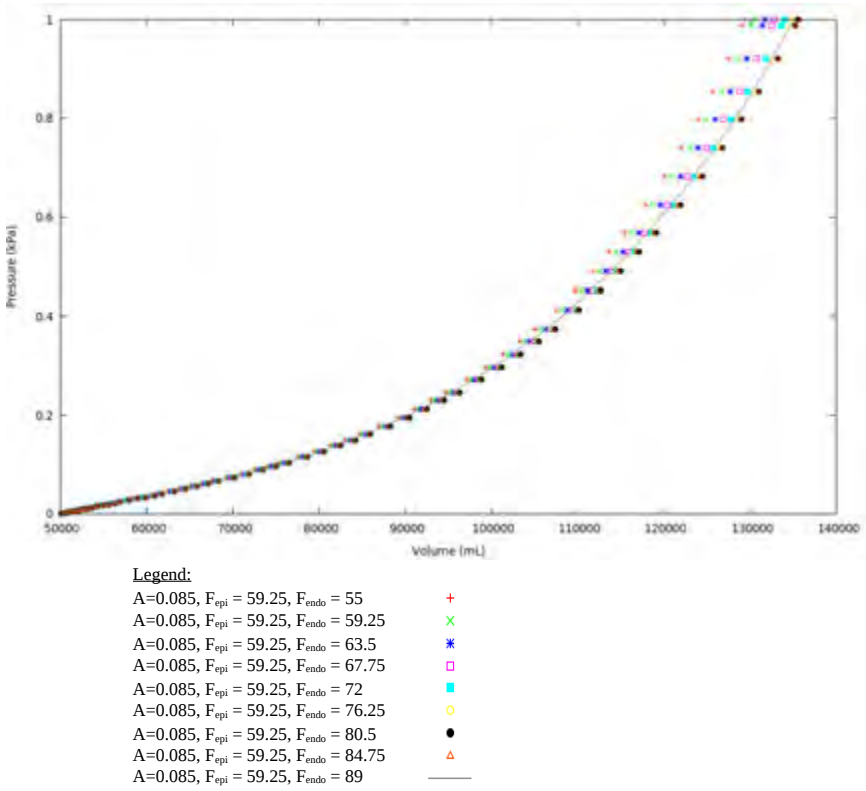

FIGURE 6.17: RV Pressure-volume graphs for A = 0.085, f_{epi} = 59.25 and varying f_{endo} parameter within the BV database.

6.6 Generation of EFG reference solution

The LV and BV models were developed and the database was constructed as described previously in this Chapter. Thereafter, conventional full-scale simulations were run by coupling the in-house Element-free Galerkin-based software called SESKA with a MATLAB-based BLVM algorithm which is based on the Levenberg Marquardt method (see Chapter 5). This full-scale simulation is assumed to be the exact solution.

The LV and BV simulations were both run for a pre-defined end-diastolic target volume of 110ml. The entire BLVM calculation process is driven by the sum of square error (SSE) principle:

$$\text{SSE} = \sum_{i=1}^{n} (\mathbf{x}_i - \mathbf{z})^2 \tag{6.3}$$

where $\mathbf{x}$ is the EDV calculated from SESKA or PODI while $\mathbf{z}$ is the pre-defined end-diastolic target volume of 110ml. The Performance Index is referred to as PI and the PI vector is the accumulation of the SSE.

The following parameters are associated with the convergence and stopping criteria for the BLVM algorithm and were set by the user for the EFG and PODI calculations:

- The maximum number of iterations, k = 500
- Value of PI = 1×10^{-2}, below which the calculation stops.
- The regularization factor, λ = 1. Lambda is also known as the Langrange multiplier.
- The speed at which lambda changes, ν = 2. Nu is a parameter used for scaling.

The BLVM algorithm allows for two strategies of scaling. One is based on the initial point and the other is based on the derivative. Scaling based on the derivative was set by the user.

The LV calculation was started on an initial parameter $A = 0.26$. During the LV calculation, each calculation step involves two simulations. The first is for initial trial parameters while the second is for the parameter perturbation. Each of these simulations ran with 2 CPU cores, in parallel with each other, ie 4 CPU cores are used in total during the EFG calculation.

The BV calculation was started with initial parameters $A = 0.21$, $f_{epi} = -50$ and $f_{endo} = 59$. During the BV calculation, each calculation step involves four simulations. The first is for the initial trial parameters while the next three are for the perturbations of each material parameter. Each of these simulation ran with 2 CPU cores, in parallel with each other, ie 8 CPU cores are used in total during the EFG calculation.

6.7 BLVM-PODI parameter optimization

The BLVM-PODI calculation was run by coupling the in-house PODI-based software ORION with the MATLAB-based BLVM algorithm. The PODI calculation is coupled with the Levenberg-Marquardt algorithm to ensure the closest fit to experimental results were achieved in an iterative process.

As done with the full-scale EFG simulations, the PODI simulations were run for a target EDV of 110mL for both the LV and BV models. The same initial starting parameter values were used, ie $A = 0.26$ for the LV and $A = 0.21$, $f_{epi} = -50$ and $f_{endo} = 59$ for the BV. The PODI calculation steps were run in serial with only one CPU core for both the LV and BV. With

regards to the parameters associated with convergence of the BLVM algorithm, the same was set as that for the full scale EFG calculation (refer to Section 6.6)

With the EFG solution being considered the reference solution, the PODI solution was then compared to the EFG solution. The results of this comparison will be presented in the next chapter.

Chapter 7

Numerical results and discussion

The primary objective of this research is to investigate a Proper Orthogonal Decomposition with Interpolation (PODI) based method for inverse material parameter optimization in the field of cardiac mechanics. This is demonstrated by comparing the material parameter calibration of the PODI-based method against the full-order EFG solution, which is assumed to be the exact solution.

Chapter 6 described the methodology employed in the problem setup for the LV and BV models as well as the creation of the database which is used by the PODI algorithm. The generation of the EFG and PODI solutions were also described in Chapter 6.

This chapter will begin with presenting a deformed configuration of the LV and BV models. Subsections 7.2 and 7.3 will then present the comparisons between the EFG and PODI solutions for the LV and BV models respectively. Pre-processing and post-processing were done using software GID version 12.0.7.

7.1 Displacement configurations

The deformed configurations at the end of the diastolic filling stage are presented in Figure 7.1 and Figure 7.2 for the LV and BV respectively. The LV model is post-processed from the dataset for $A = 0.14$ while the BV model is from the dataset for $A = 0.04$, f_{epi} = 48 and f_{endo} = 55.

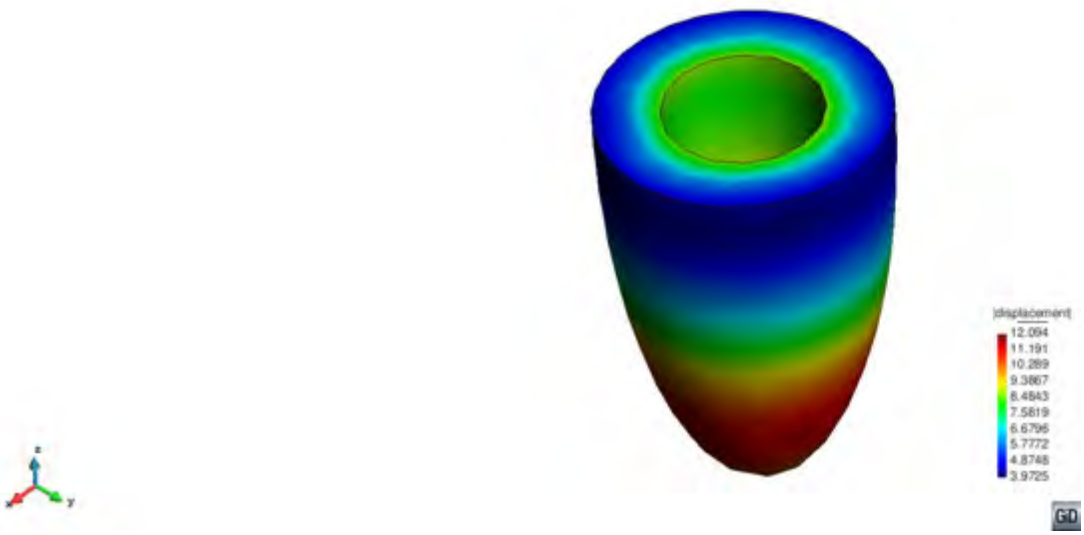

FIGURE 7.1: Displacements for the LV at the end of diastolic filling

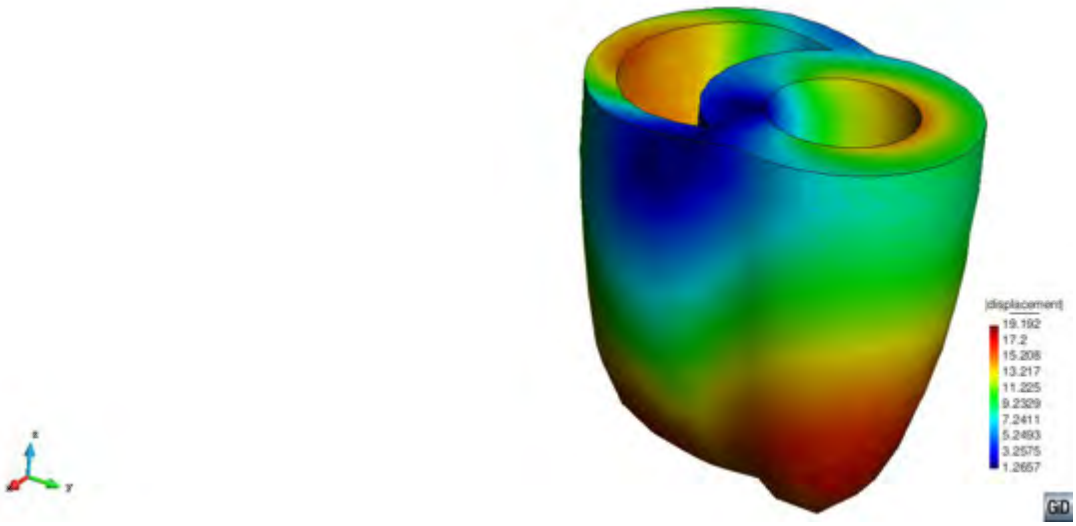

FIGURE 7.2: Displacements for the BV at the end of diastolic filling

The maximum displacement which the LV undergoes is 12.094mm while the BV undergoes 19.192mm. Both of the maximum displacements occur towards the bottom of the ventricle.

7.2 Single parametric PODI calculation for LV model

The single parametric PODI and EFG calculations for the LV involved the calibration of a single material paramater, in this case the parameter A. The PODI-based parameter optimization was completed in 2 minutes and 14 seconds whereas the conventional EFG-based parameter optimization took approximately 2 days and 2 hours while using 4 times the amount of physical cores. This shows PODI as being approximately 1351 times faster than

EFG. Both calculations took 6 iteration steps to converge. This section will present a comparison of the results obtained for the PODI and EFG calculations of the LV.

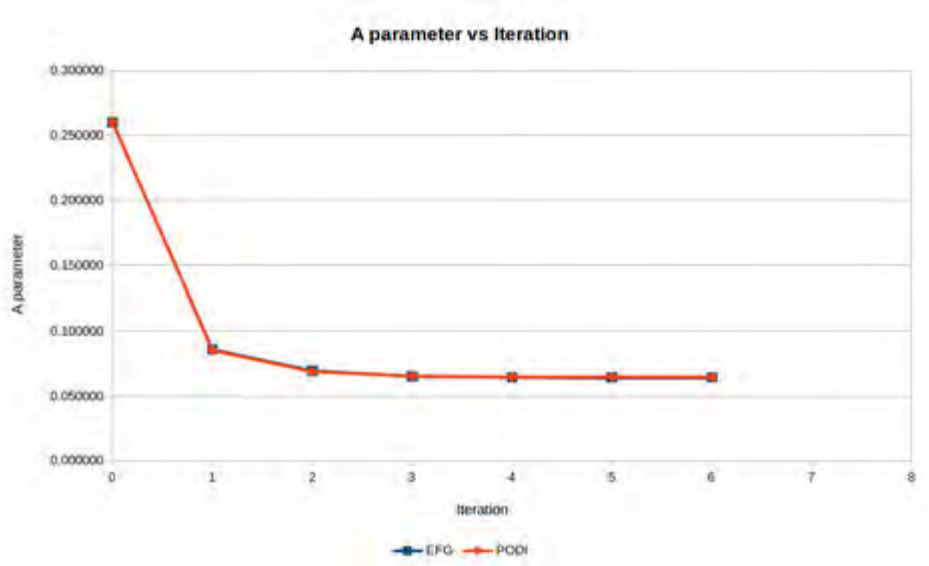

FIGURE 7.3: EFG and PODI calculation results for the LV parameter A versus Iteration step

Figure 7.3 provides a comparison between the parameter A for each iteration step of the PODI and EFG calculations. The results are almost identical with a maximum deviation of only 1% on iteration step 2. The EFG calculation completed with a final parameter $A = 0.064158$ while the PODI finished with parameter $A = 0.064378$. The final PODI parameter A is within 0.4% of the EFG final parameter A, which is considered to be the exact solution.

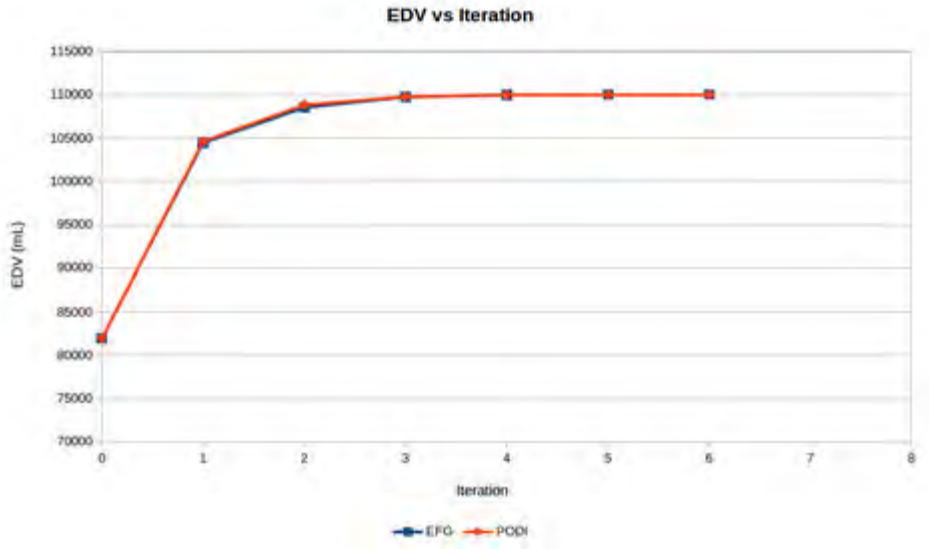

FIGURE 7.4: EFG and PODI calculation results for the LV end diastolic volume (EDV) versus Iteration step

Figure 7.4 provides a comparison between the EDV for each iteration step of the PODI and EFG calculations. The PODI and EFG calculations follow an almost identical path towards the pre-defined end-diastolic target volume of 110ml with a maximum deviation of 0.27%. The EFG calculation completed with a final EDV of 109999.950 ml while the PODI finished with a final EDV of 109998.163 ml. The final EDV for the PODI calculation is within 0.002% of the exact solution.

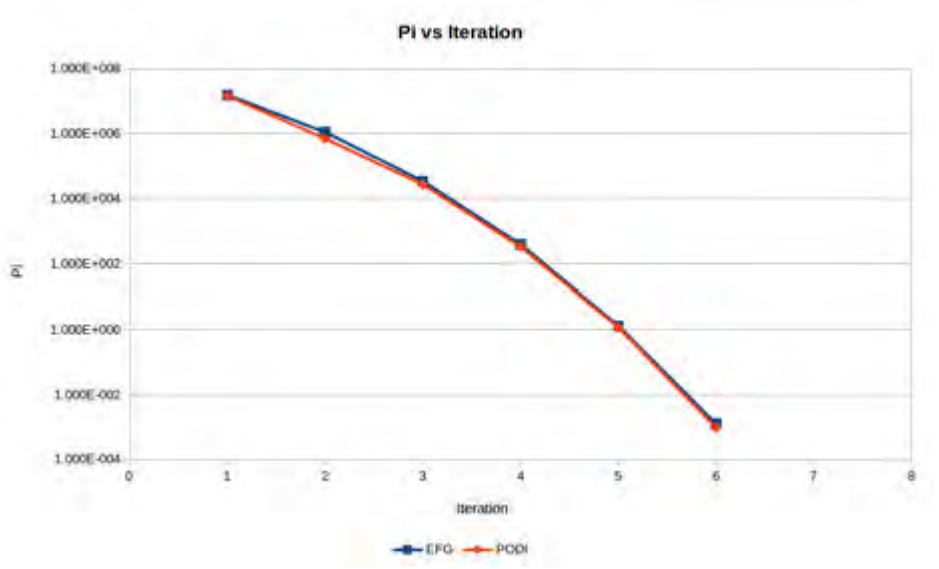

FIGURE 7.5: EFG and PODI calculation results for the LV PI value versus Iteration step

As discussed in Section 6.6, PI is known as the Performance Index and respresents the sum of square error. Figure 7.5 therefore represents the error between the pre-defined end-diastolic target volume of 110ml and the EDV of the respective calculations. The two calculations follow a similar trend with the PODI having a slightly lower PI value on each iteration step as compared to the EFG calculation. The termination criteria, that stops the calibration, is the user set value of PI= 1×10^{-2}. Therefore the calibration terminates when PI goes below 1×10^{-2}. Consequently, the LVM algorithm terminated when the parameters stopped changing significantly.

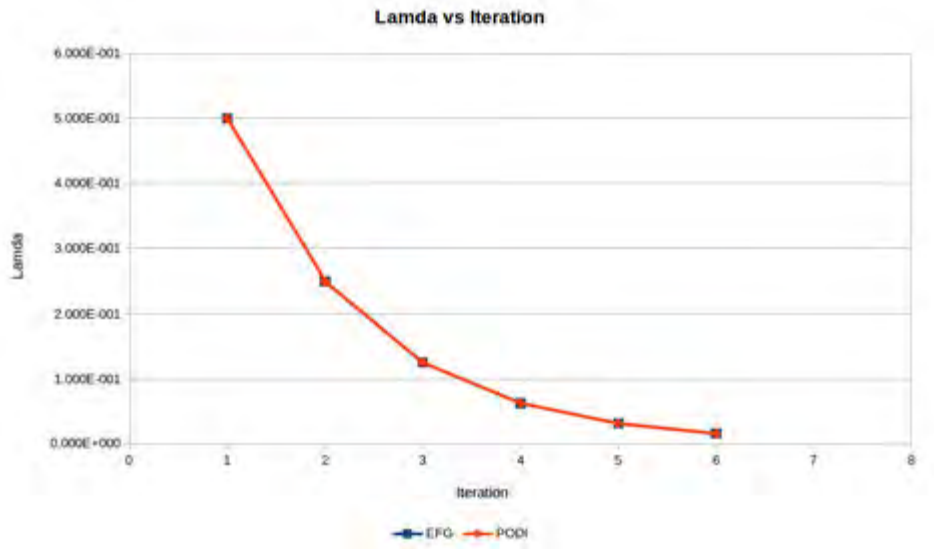

FIGURE 7.6: EFG and PODI calculation results for the LV Lambda versus Iteration step

As mentioned in Section 6.6, lambda is known as the regularization factor or Langrange multiplier. Figure 7.6 provides a comparison between the Lambda for each iteration step of the PODI and EFG calculations. The results are exactly the same and halve with each iteration. This is expected since the speed at which lambda changes, nu, was set 2. It should be noted that during the inital calculation steps,lambda puts emphasis on the Steepest Descent method and this changes to the Gauss-Newton method as lambda tends towards zero.

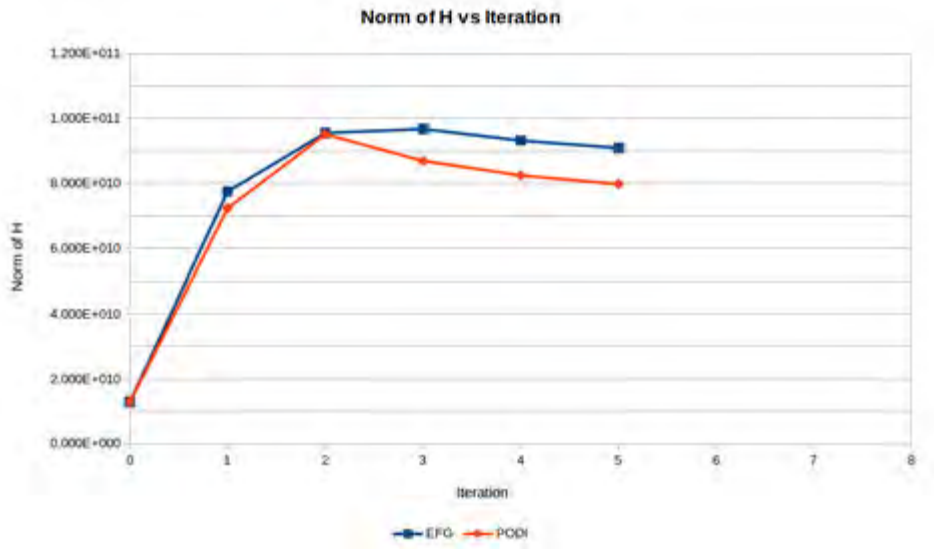

FIGURE 7.7: EFG and PODI calculation results for the LV Norm of H versus Iteration step

The Norm of H is the rate at which the error gradient changes. Figure 7.7 provides a comparison between the Norm of H for the PODI and EFG

calculations. The two graphs were almost identical except for the last 3 steps when the PODI gradient is much lower than that of EFG. This difference may indicate a more smooth error domain which may originate from the MLS interpolation. The PODI has a lower Norm of H on every iteration step as compared to the EFG calculation. Since the Norm of H gives an indication of the gradient of the error between each iteration, this implies that the PODI moves towards the pre-defined EDV at a slower rate than the EFG.

Given that PODI simulations introduce a small deviation in the results when compared to EFG, it is also expected that the end points of the PODI and EFG will be different. It should also be noted that the LVM builds up from results of previous steps, therefore there could be the possibility of the PODI simulation to take a different path compared to that of the EFG. The path of both methods were very similar as shown in Figure 7.3. This observation was confirmed as the PODI deviation of A was always below 1% across all steps. Based on these deviation values, which can be considered to be negligibly small, it can be deduced that the accuracy of the PODI solution for the LV obtained over such a short calculation time is acceptable.

The entire results data for the EFG and PODI calculations of the LV is provided within Appendix C.1.

7.3 Multi-parametric PODI calculation for BV model

For the multi-parametric PODI and EFG calculations, f_{epi} and f_{endo} are also included along with parameter A in the list of parameters to be calibrated. The geometrical complexity is also increased by using a bi-ventricle model which now includes a right ventricle. The PODI-based parameter optimization was completed in 9 minutes and 52 seconds whereas the conventional EFG-based parameter optimization took about 1 day and 16 hours using 8 times the amount of physical cores. This shows PODI as being approximately 248 times faster than EFG. Both calculations took 5 iteration steps to converge. As done with the LV model, this section will compare the results obtained for the PODI and EFG calculations for the BV.

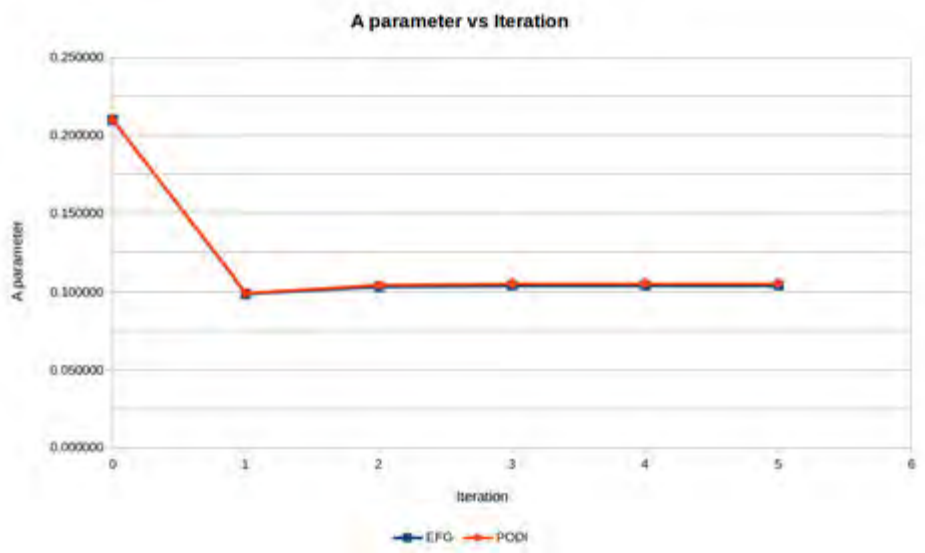

FIGURE 7.8: EFG and PODI calculation results for the BV parameter A versus Iteration step

Figure 7.8 shows a comparison between parameter A for each iteration step of the PODI and EFG calculations. The results between the two methods are very similar with a maximum deviation of only 1.23% on iteration step 5. The EFG calculation completed with a final parameter A = 0.104225 while the PODI finished with A = 0.105503, which is within 1.3% of the EFG final parameter A.

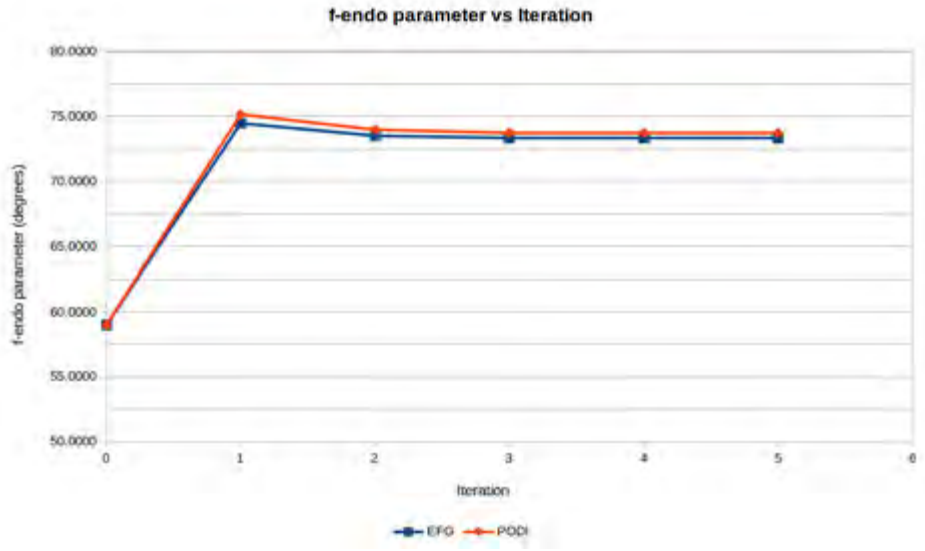

FIGURE 7.9: EFG and PODI calculation results for the BV f_{endo} versus Iteration step

Figure 7.9 provides a comparison between the f_{endo} for each iteration step of the PODI and EFG calculations. The results are again very similar with a maximum deviation of 0.91% on iteration step 2. The EFG calculation

completed with a final parameter value of f_{endo} = 73.3039 while the PODI finished with f_{endo} = 73.7143.

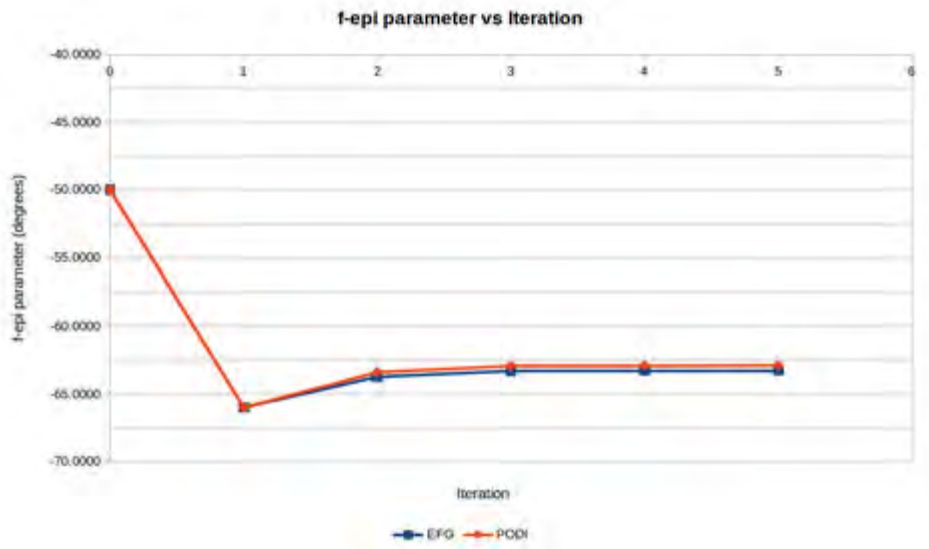

FIGURE 7.10: EFG and PODI calculation results for the BV f_{epi} versus Iteration step

Figure 7.10 provides a comparison between the f_{epi} for each iteration step of the PODI and EFG calculations. The results are almost identical with a maximum deviation of 0.6% on iteration step 4 and 5. The EFG calculation completed with a final parameter value of f_{epi} = -63.2704 while the PODI finished with f_{epi} = -62.8909. It is interesting to note that the deviations of the final PODI values to the exact solution for the fibre distributions, f_{epi} and f_{endo}, were both equal to 0.6%.

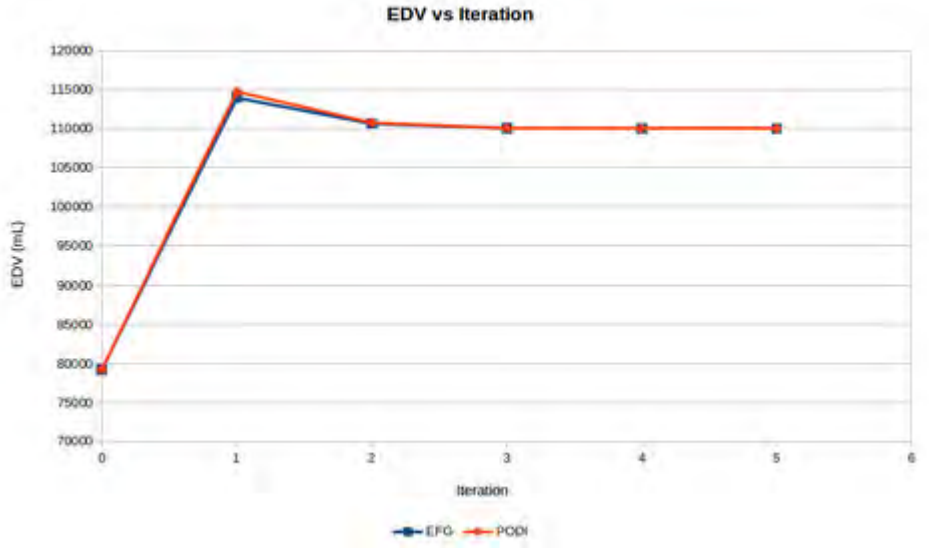

FIGURE 7.11: EFG and PODI calculation results for the BV end diastolic volume (EDV) versus Iteration step

Figure 7.11 provides a comparison between the EDV for each iteration step of the PODI and EFG calculations. The results are similar with a maximum deviation of only 0.69% on iteration step 2. Converse to the LV calculation, the EFG initially starts slightly closer than PODI to the target EDV of 110ml on the first calculation step. The EFG calculation finished with an EDV of 110000.038 ml while the PODI finished with an EDV of 110000.095 ml. These final EDV values can be considered to be equal.

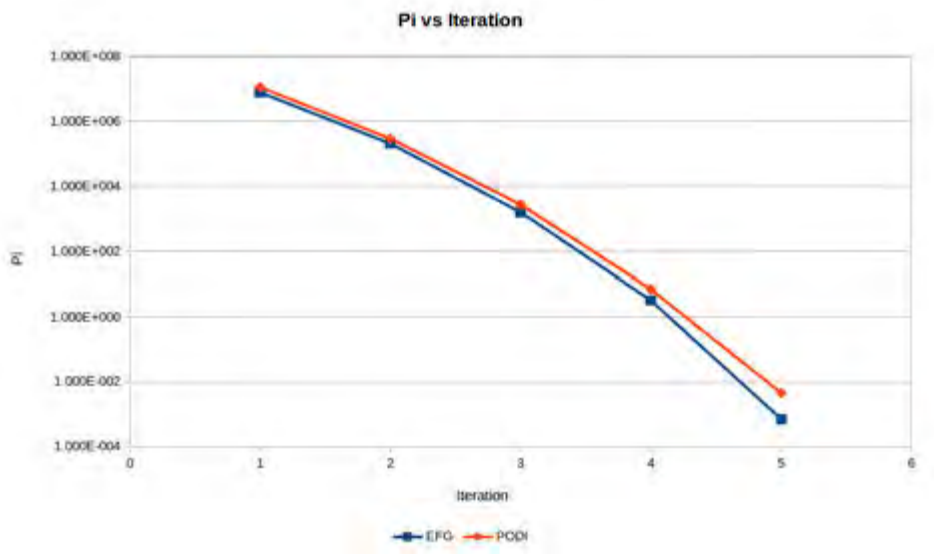

FIGURE 7.12: EFG and PODI calculation results for the BV PI value versus Iteration step

Figure 7.12 provides the error between the pre-defined end-diastolic target volume of 110ml and the EDV of each calculations at each iteration step. The EFG and PODI follow a similar trend with the PODI having a slightly lower PI value on each iteration step as compared to the EFG calculation. As with the LV, the termination criteria, that stops the calibration, is the user set value of PI= 1×10^{-2}. the LVM algorithm terminated when the parameters stopped changing significantly.

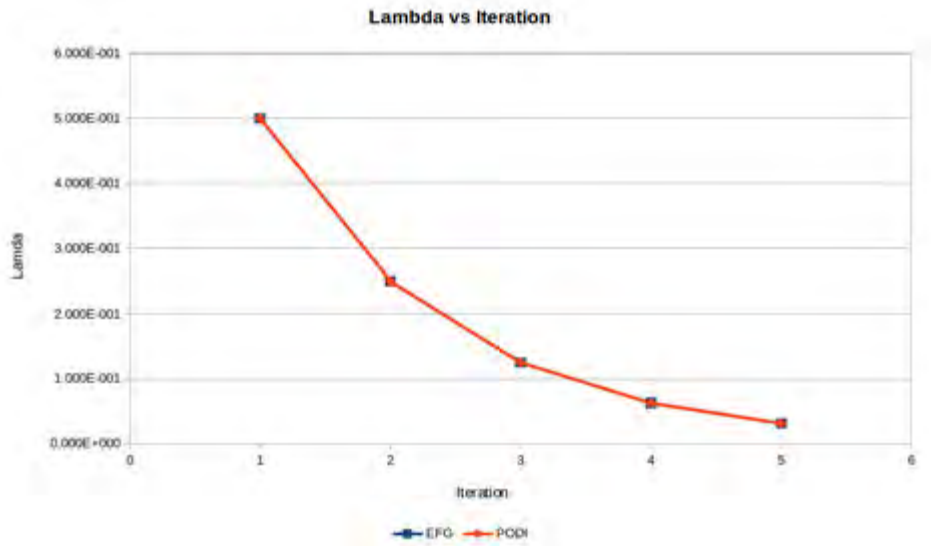

FIGURE 7.13: EFG and PODI calculation results for the BV Lambda versus Iteration step

Figure 7.13 provides a comparison between the Lambda for each iteration step of the PODI and EFG calculations. As with the LV, the results are exactly the same and halve with each iteration. Again, this is expected since the speed at which lambda changes, nu, was set 2.

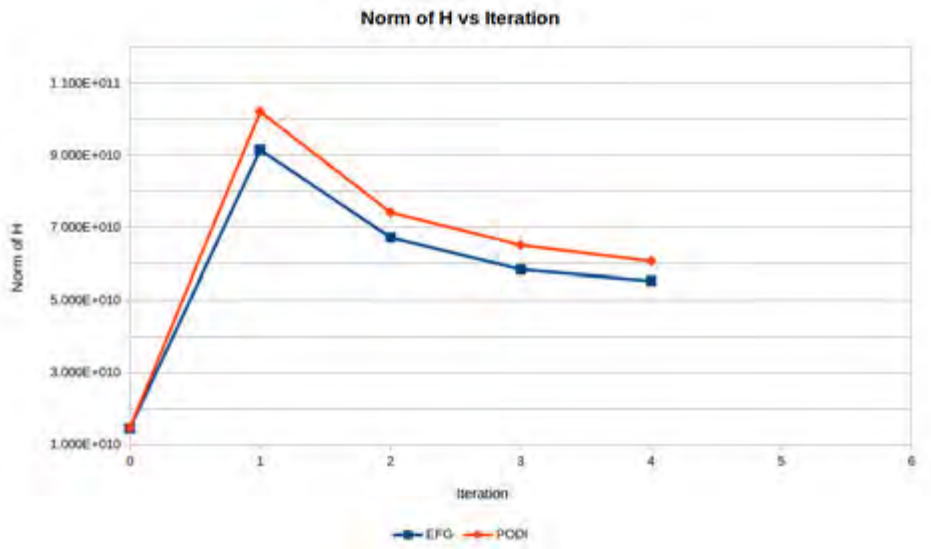

FIGURE 7.14: EFG and PODI calculation results for the BV Norm of H versus Iteration step

Figure 7.14 provides a comparison between the rate of change of the error gradient for the PODI and EFG calculations of the BV. Throughout all the iteration steps, the PODI has a higher Norm of H than EFG with a maximum deviation on iteration step 2. This implies that the PODI moves towards the pre-defined EDV at a faster rate than the EFG. Converse to the

LV calculations, the PODI has a greater PI and Norm of H on each iteration step as compared to the EFG calculation. This change in behaviour could be due to the introduction of the right ventricle within the BV model.

As mentioned previously, the PODI simulations introduce a small deviation in the results when compared to EFG and the LVM builds up from results of previous steps, therefore there could be the possibility of the PODI simulation to take a different path compared to that of the EFG. In the case of the BV calculations, there are three parameters which deviate and each of these have different end points of the PODI and EFG. Overall, the path of both methods were similar for all of the material parameter calibrations as shown in Figures 7.8, 7.9 and 7.10 for A, f_{endo} and f_{epi} respectively. In fact, the PODI deviation was always below 1.3% across all steps for the three material parameter calibrations. Based on these deviation values, which can be considered to be negligibly small, it can be deduced that the accuracy of the PODI solution obtained over such a short calculation time is acceptable.

7.4 Results Summary

Table 7.1 provides a comparison between the time taken for the EFG and PODI calculation of the LV while Table 7.2 provides similar for the BV.

TABLE 7.1: EFG & PODI simulation times for the LV

	EFG	PODI
Time taken (d:hh:mm:ss)	2:02:17:47	0:00:02:14
Time taken (seconds)	181067	134
Number of processors	4	1

TABLE 7.2: EFG & PODI simulation times for the BV

	EFG	PODI
Time taken (d:hh:mm:ss)	1:16:50:25	0:00:09:52
Time taken (seconds)	147025	592
Number of processors	8	1

For the LV, the PODI calculation was completed in 2 minutes and 14 seconds, compared to the EFG simulation which took about 2 days and 2 hours using 4 times the amount of physical cores. For the BV, the PODI calculation was completed in 9 minutes and 52 seconds, compared to the EFG simulation which took about 1 days and 16 hours using 8 times the amount

of physical cores.

TABLE 7.3: PODI deviations for LV and BV

Single parametric calculation (LV)	Deviation
A	0.34%
Multi-parametric calculation (BV)	Deviation
A	1.23%
f_{epi}	0.60%
f_{endo}	0.56%

Table 7.3 summarizes the deviations of the final PODI parameters to that of the exact solution. As can be seen, all deviations were below 1.3%.

The entire results data for the EFG and PODI calculations of the BV is provided in Appendix C.2. The deviation for each calculation step is also provided within the same Appendix.

Chapter 8

Conclusion and future work

The major objective of this research was to investigate a Proper Orthogonal Decomposition with Interpolation (PODI) based method for inverse material parameter optimization in the field of cardiac mechanics. This chapter will summarise the major findings, acknowledge any potential shortcomings and outline the future work for the research.

8.1 Summary and concluding remarks

In this work, the computational cardiac mechanics of the human heart were successfully developed, introducing the kinematics and constitutive laws of the problem description. The initial calibration of anisotropic material parameters was achieved using shear test data from the experimental work by Sommer et al. [67]. A LV and BV model were created which describe the mechanical function of the human heart, together with boundary conditions that simulate the cardiac cycle from the beginning of passive filling to the end of the passive filling stage. The geometry of the left ventricle was approximated using an ellipsoid, with the description of fibre orientation consistent with experimental data. The geometry of the right ventricle was calibrated such that the end diastolic volume was consistent with experimental data by Sandstede et al. [60]. For the purpose of the PODI calculation, a database was constructed for the LV and BV by running full scale simulations on varying material parameters where upper and lower bounds of the database were controlled by the EDV gained from the experimental data by Sandstede et al. [60].

The results achieved in this work show that PODI can provide a significantly faster alternative of computational material parameter optimization to conventional full-scale simulation-based approaches using EFG or FEM. For the LV, the PODI was approximately 1351 times faster than EFG.For the BV, the PODI was approximately 248 times faster than EFG. It should also be pointed out that the EFG calculation ran with 2 CPU cores in parallel while the PODI calculation ran with one CPU core in series. Table 7.3 summarizes the deviations of the final PODI parameters to that of the exact

solution. As can be seen, all deviations were below 1.3%.

The results obtained from this research show that material parameter calibration times for human heart models can be drastically reduced using PODI-based parameter optimization. Even though a small loss of accuracy was noted,resulting in parameter value deviations of about 1%, it is deemed acceptable considering the impressive gain in computation speed for the PODI calculation.

8.2 Future work

Extension of database
Following these encouraging results, the next step would be to extend the PODI method to interpolate datasets of hearts with different geometries and mesh discretisations. This is important, because the structural composition of hearts vary between individuals.

The cardiac cycle
As an initial investigation, the current research presents results up until the end of the passive filling phase only. Due to time constraints, the isovolumetric contraction, ejection and the isovolumetric relaxation phases have been excluded. Initial investigation by the CCM group shows that the PODI is compatible with these other phases of the cardiac cycle.

In future work, the isovolumetric contraction, ejection and the isovolumetric relaxation phases must be included in the analysis. Ideally, multiple cardiac cycles should be run in a continuous computational experiment. The final deformation of the ventricle at the end of one cycle is used as the starting point for the subsequent cycle. In this way, residual stress can be included in the model and a more realistic cardiac cycle can be modelled.

Sensitivity analysis
A sensivity analysis should form part of the next phase of this investigation to check the effects of refining the database. This exercise would involve a refining the database increments, therefore increasing the number of datasets, and then checking the effects this has on the PODI accuracy.

Appendix A

SESKA

SESKA is a C++ code built upon several libraries by Dr S. Skatulla since the start of the 2000s. SESKA based on the element free Galerkin method (EFGM) which uses moving least squares (MLS) approximations of the solution over the domain. For further details on EFGM and MLS methods, the reader is directed to the paper by Belytschko, Lu, and Gu [2]. The preprocessing, calculation process and post processing are all carried out by the code. The geometry definition and 3D solution visualisation are handled by the pre/post processing commercial software package, GiD. Most of SESKA's processes are parallelised using the OpenMPI library, thus allowing large problems to be solved on high performance computers.

The solving process in SESKA is outlined as follows:

1. the construction of shape functions
2. assembly particle contributions to a global stiffness matrix and/or mass matrix (for dynamic problems)
3. solve the set of equations either in a linear or Newton Raphson scheme, depending on the problem description.

The power of the software is its ability to run on large computing clusters, enabling the user to simulate large problems with highly refined particle distributions.

Appendix B

ORION

ORION is a C++ code built upon several libraries by Mr Ritesh Rama. The main software objective is to solve for required datasets between stored datasets of a database using the Proper Orthogonal Decomposition with Interpolation (PODI) method.

The distinctiveness of using the Proper Orthogonal Decomposition-based (POD) software ORION is that it reduces the complexity of a large dataset. It does so by using linear algebraic operations, namely Eigen vectors and their associated Eigenvalues, to project said dataset to a lower order solution space. In this lower order solution space ORION employs an interpolation technique in order to compute effective constitutive material constants. With regard to computational time, it should be noted that ORION could reduce simulation time greatly. The PODI process which PRION employs is illustrated in Figure B.1.

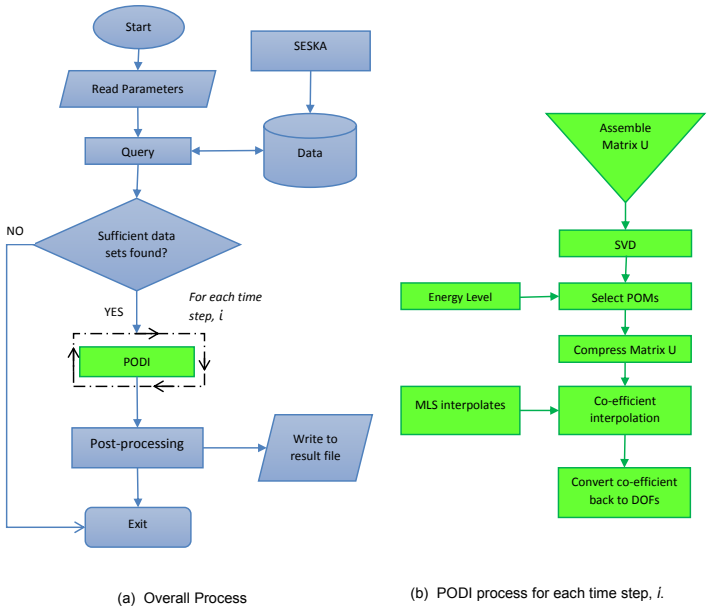

(a) Overall Process

(b) PODI process for each time step, *i*.

FIGURE B.1: Flow chart of simulation program.

Appendix C

Calculation Data

C.1 LV Calculation Data

TABLE C.1: EFG calculation data for the LV

Calculation Step	EFG				
	A value	EDV	Norm of H	PI	Lamda
Starting Parameter	0.260000	81946.404	1.295E+010		
Iteration 1	0.085672	104432.371	7.745E+010	1.550E+007	5.000E-001
Iteration 2	0.069344	108516.042	9.549E+010	1.101E+006	2.500E-001
Iteration 3	0.065049	109737.520	9.671E+010	3.445E+004	1.250E-001
Iteration 4	0.064253	109971.964	9.313E+010	3.930E+002	6.250E-002
Iteration 5	0.064164	109998.389	9.088E+010	1.297E+000	3.125E-002
Iteration 6	0.064158	109999.950		1.256E-003	1.563E-002

TABLE C.2: PODI calculation data for the LV

Calculation Step	PODI				
	A value	EDV	Norm of H	PI	Lamda
Starting Parameter	0.260000	81911.925	1.288E+010		
Iteration 1	0.085004	104613.005	7.231E+010	1.450E+007	5.000E-001
Iteration 2	0.068653	108813.006	9.509E+010	7.022E+005	2.500E-001
Iteration 3	0.065215	109765.172	8.686E+010	2.715E+004	1.250E-001
Iteration 4	0.064470	109972.520	8.240E+010	3.299E+002	6.250E-002
Iteration 5	0.064383	109996.688	7.973E+010	1.158E+000	3.125E-002
Iteration 6	0.064378	109998.163		9.579E-004	1.562E-002

TABLE C.3: Deviation data for the LV

Calculation Step	Deviation				
	A value	EDV	Norm of H	PI	Lamda
Starting Parameter	0.00%	-0.04%	-0.52%		
Iteration 1	-0.78%	0.17%	-6.64%	-6.45%	0.00%
Iteration 2	-1.00%	0.27%	-0.41%	-36.23%	0.00%
Iteration 3	0.26%	0.03%	-10.18%	-21.19%	0.00%
Iteration 4	0.34%	0.00%	-11.53%	-16.06%	0.00%
Iteration 5	0.34%	0.00%	-12.27%	-10.73%	0.00%
Iteration 6	0.34%	0.00%		-23.73%	-0.03%

C.2 BV Calculation Data

TABLE C.4: EFG calculation data for the BV

Calculation Step	EFG						
	A value	Fepi	Fendo	EDV	Norm of H	PI	Lamda
Start	0.210000	-50.0000	59.0000	79252.387	1.454E+010		
Iteration 1	0.098766	-66.0000	74.4660	113952.412	9.146E+010	7.811E+006	5.000E-001
Iteration 2	0.103339	-63.7298	73.5004	110642.154	6.718E+010	2.062E+005	2.500E-001
Iteration 3	0.104148	-63.3108	73.3212	110056.174	5.836E+010	1.578E+003	1.250E-001
Iteration 4	0.104222	-63.2721	73.3047	110002.521	5.533E+010	3.178E+000	6.250E-002
Iteration 5	0.104225	-63.2704	73.3039	110000.038		7.040E-004	3.125E-002

TABLE C.5: PODI calculation data for the BV

Calculation Step	PODI						
	A value	Fepi	Fendo	EDV	Norm of H	PI	Lamda
Start	0.210000	-50.0000	59.0000	79280.449	1.472E+010		
Iteration 1	0.099229	-66.0000	75.1464	114736.238	1.021E+011	1.123E+007	5.000E-001
Iteration 2	0.104420	-63.3975	73.9716	110764.916	7.414E+010	2.925E+005	2.500E-001
Iteration 3	0.105399	-62.9398	73.7390	110073.711	6.509E+010	2.717E+003	1.250E-001
Iteration 4	0.105498	-62.8933	73.7155	110003.738	6.069E+010	6.987E+000	6.250E-002
Iteration 5	0.105503	-62.8909	73.7143	110000.095		4.521E-003	3.125E-002

TABLE C.6: Deviation data for the BV

Calculation Step	Deviation						
	A value	Fepi	Fendo	EDV	Norm of H	PI	Lamda
Start	0.00%	0.00%	0.00%	0.04%	1.21%		
Iteration 1	0.47%	0.00%	0.91%	0.69%	11.58%	43.78%	0.00%
Iteration 2	1.05%	-0.52%	0.64%	0.11%	10.35%	41.87%	0.00%
Iteration 3	1.20%	-0.59%	0.57%	0.02%	11.53%	72.21%	0.00%
Iteration 4	1.22%	-0.60%	0.56%	0.00%	9.68%	119.85%	0.00%
Iteration 5	1.23%	-0.60%	0.56%	0.00%		542.17%	0.00%

Bibliography

[1] S. Avril et al. “Overveiw of identification methods of mechanical parameters based on full-feild measurements”. In: *Experimental Mechanics* 48.4 (2008), pp. 381–402. DOI: 10.1007/s11340-008-9148-y.

[2] T. Belytschko, Y.Y. Lu, and L. Gu. “Element-free galerkin methods”. In: *International Journal for Numerical Methods in Engineering* 37.2 (1994), pp. 229–256. DOI: 10.1002/nme.1620370205.

[3] F.M. Capaldi. *Continuum Mechanics - Constitutive Modelling of Structural and Biological Materials*. First. Cambridge University Press, 2012.

[4] Anindya Chatterjee. “An introduction to the proper orthogonal decomposition”. In: *Current Science* 78.7 (2000), pp. 808–817.

[5] K. D. Costa, J. W. Holmes, and A. D. Mcculloch. “Modelling cardiac mechanical properties in three dimensions”. In: *Philosophical Transactions of the Royal Society A* 359.1783 (2001), 1233âĂŞ1250.

[6] K.D. Costa et al. “Laminar fiber architecture and three-dimensional systolic mechanics in canine ventricular myocardium”. In: *American Journal of Physiology - Heart and Circulatory Physiology* 276.2 (1999), H595–H607.

[7] J.P. Cusumano, M.T. Sharkady, and B.W. Kimble. “Experimental measurements of dimensionality and spatial coherence in the dynamics of a flexible-beam impact oscillator”. In: *Philosophical Transactions of the Royal Society of London, Ser. A* 347 (1994), pp. 421–438.

[8] S. Dokos et al. “Shear properties of passive ventricular myocardium”. In: *Am J Physiol Heart Circ Physiol* (2002), H2650âĂŞH2659. DOI: 10.1152/ajpheart.00111.2002.

[9] P. Druault, P. Guibert, and F. Alizon. “Use of proper orthogonal decomposition for time interpolation from PIV data: Application to the cycle-to-cycle variation analysis of in-cylinder engine flows”. In: *Experiments in Fluids* 39.6 (2005), pp. 1009–1023. DOI: 10.1007/s00348-005-0035-3.

[10] L. Dubuis et al. “Identification of the material parameters of soft tissues in the compressed leg”. In: *Computer Methods in Biomechanics and Biomedical Engineering* 15.1 (2012), pp. 3–11. DOI: 10.1080/10255842.2011.560666.

[11] M Essack. "Material Parameter Identification for Modelling the Left Ventricle in the Healthy State". MA thesis. The University of Cape Town, 2014.

[12] N.J. Falkiewicz and C. E. S. Cesnik. "Proper Orthogonal Decomposition for Reduced-Order Thermal Solution in Hypersonic Aerothermoelastic Simulations". In: *AIAA Journal* 49.5 (2011). DOI: 10.2514/1.J050701.

[13] B.F. Feeny and R. Kappagantu. "On the physical interpretation of proper orthogonal modes in vibrations". In: *Journal of Sound and Vibration* 211.4 (1998), pp. 607–616.

[14] Y.C. Fung. "Biorheology of soft tissues." In: *Biorheology* 10.2 (1973), pp. 139–155.

[15] Y.C. Fung. "Elasticity of soft tissues in simple elongation". In: *Am. J. Physiol* 213.6 (1967), pp. 1532–1544.

[16] H.P. Gavin. "The Levenberg-Marquardt method for nonlinear least squares curve-fitting problems." In: *Department of Civil and Environmental Engineering, Duke University (2011): 1-15.* (2013), pp. 1–15. URL: http://people.duke.edu/~hpgavin/ce281/lm.pdf.

[17] C.W. Groetsch. *Inverse Problems in the Mathematical Sciences*. Friedrich Vieweg & Sohn Verlagsgesellschaft mbh, 1993.

[18] J.M. Guccione, K.D. Costa, and A.D. McCulloch. "Finite element stress analysis of left ventricular mechanics in the beating dog heart". In: *Journal of Biomechanics* 28.10 (1995), pp. 1167–1177. DOI: 10.1016/0021-9290(94)00174-3.

[19] F. Guyon and R.L. Riche. *Least Squares Parameter Estimation and the Levenberg-Marquardt Algorithm: Deterministic Analysis, Sensitivities and Numerical Experiments*. Tech. rep. Technical Report INSA No.: 041/99. Institut national des sciences appliquÃl'es de Rouen, 2000.

[20] Guyton and Hall. *Textbook of Medical Physiology*. Ed. by John Edward Hall. 11th. Elsevier Saunders, 2006.

[21] P. Holmes, J.L Lumley, and G. Berkooz. *Turbulence, Coherent Structures, Dynamical Systems and Symmetry*. Cambridge University Press, 1996.

[22] G. A. Holzapfel and R. W. Ogden. "Constitutive modelling of passive myocardium: a structurally based framework for material characterization". In: *Royal Society of London Philosophical Transactions A: Mathematical, Physical and Engineering Sciences* 367.1902 (2009). DOI: 10.1098/rsta.2009.0091.

[23] L.E. Hudsmith et al. "Normal human left and right ventricular and left atrial dimensions using steady state free precession magnetic resonance imaging." In: *J Cardiovasc Magn Reson.* 7.5 (2005), pp. 775–782.

[24] J.D. Humphrey. *CardiovaCardio Solid Mechanics: Cell, Tissues, Organs*. Springer, 2002. DOI: 10.1115/1.1497492.

[25] J.D. Humphrey. "Review Paper: Continuum biomechanics of soft biological tissues". In: *Proceedings of the Royal Society of London* 459.2029 (2003), pp. 3–46. DOI: 10.1098/rspa.2002.1060.

[26] J.D. Humphrey and F.C.P. Yin. "On constitutive relations and finite deformations of passive cardiac tissue: I. A pseudostrain-energy function". In: *Journal of biomechanical engineering* 109.4 (1987), pp. 298–304. DOI: doi:10.1115/1.3138684.

[27] J.R. Hussan, M.L. Trew, and P.J. Hunter. "A Mean-field Model of Ventricular Muscle Tissue". In: *Journal of Biomechanical Engineering* 134.7 (2012). DOI: 10.1115/1.4006850.

[28] C. Kanzowa, N. Yamashitab, and M. Fukushimab. "LevenbergâĂŞMarquardt methods with strong local convergence properties for solving nonlinear equations with convex constraints". In: *Journal of Computational and Applied Mathematics* 172.2 (2004), pp. 375–397. DOI: 10.1016/j.cam.2004.02.013.

[29] K. Karhunen. "Uber Lineare Methoden in der Wahrscheinlichkeitsrechnung". In: *Annals of Academic Science Fennicae, Series A1 Mathematics and Physics* 37 (1946), pp. 3–79.

[30] A. M. Katz. *Physiology of the Heart*. 5th ed. Lippincott Williams & Wilkins, 2010.

[31] R. Kerckhoffs. "Depolarization wave and mechanics in the paced heart: Model and Experiment". PhD thesis. Technical University of Eindhoven, 2003.

[32] D.D. Kosambi. "Statistics in function space". In: *Journal of Indain Mathematical Society* 7 (1943), pp. 76–88.

[33] M.H. Kural et al. "Planar biaxial characterization of diseased human coronary and carotid arteries for computational modeling". In: *Journal of Biomechanical Engineering* 45.5 (2012), pp. 790–798. DOI: 10.1016/j.jbiomech.2011.11.019.

[34] P. Lafortune et al. "Coupled electromechanical model of the heart: Parallel finite element formulation". In: *International Journal for Numerical Methods in Biomedical Engineering* 28.1 (2012), pp. 72–86. DOI: 10.1002/cnm.1494.

[35] W.M. Lai, D. Rubin, and E. Krempl. *Introduction to Continuum Mechanics*. 4th edition. Elsevier Ltd, 2010.

[36] P. Lancaster and K. Salkauskas. "Surfaces generated by moving least squares methods". In: *Mathematics of Computation* 37.155 (1981), pp. 141–158. URL: http://dx.doi.org/10.1090/S0025-5718-1981-0616367-1.

[37] K. Levenberg. "A method for the solution pf certain non-linear problems in least squares". In: *Quartely of Applied Mathematics* 2 (1944), pp. 164–168.

[38] H. Li, Z. Luo, and J. Chen. "Numerical simulation based on pod for two-dimensional solute transport problems". In: *Applied Mathematical Modelling* 35.5 (2011), 2489âĂŞ2498. DOI: http://dx.doi.org/10.1016/j.apm.2010.11.064.

[39] Y. C. Liang et al. "Proper Orthogonal Decomposition and its Applications - Part I: Theory". In: *Journal of Sound and Vibration* 252.3 (2002), pp. 527–544. DOI: 10.1006/jsvi.2001.4041.

[40] W.Z. Lin, Y.J. Zhang, and E.P. Li. "Proper Orthogonal Decomposition in the Generation of Reduced Order Models for Interconnects". In: *IEEE Transactions on Advanced Packaging* 31.3 (2008), pp. 627 –636. DOI: http://dx.doi.org/10.1109/TADVP.2008.927820.

[41] M. Loeve. "Fonctions Al ÌĄeatoires du Second Ordre". In: *Supplement to Processus stochastiques et mouvement Brownien, P. Levy (ed.), Gauthier-Villars, Paris* (1948).

[42] M.I.A. Lourakis. "A Brief Description of the Levenberg-Marquardt Algorithm Implemened by levmar". In: *Foundation of Research and Technology* 4 (2005), pp. 1–6. URL: http://users.ics.forth.gr/~lourakis/levmar/levmar.pdf.

[43] H.V. Ly and H.T. Tran. "Modeling and control of physical processes using proper orthogonal decomposition". In: *Computation and control VI proceedings of the sixth Bozeman conference* 33.1-3 (2001), pp. 223–236. DOI: http://dx.doi.org/10.1016/S0895-7177(00)00240-5.

[44] D.W. Marquardt. "An Algorithm for Least-Squares Estimation of Nonlinear Parameters". In: *Journal of the Society for Industrial and Applied Mathematics* 11.2 (1963), pp. 431–441. DOI: 10.1137/0111030.

[45] G.T. Mase, R.E. Smelser, and G.E. Mase. *Continuum Mechanics for Engineers*. Ed. by J.N. Reddy. Third Edition. CRC Press Taylor & Francis Group, 2010.

[46] S. Mendis, P. Puska, and B. Norrving. *Global Atlas on Cardiovascular Disease Prevention and Control*. World Health Organization. 2011. URL: http://www.who.int/cardiovascular_diseases/publications/atlas_cvd/en/.

[47] D. Mozaffarian et al. "Heart disease and stroke statisticsâĂŤ2016 update: a report from the American Heart Association". In: *Circulation* 132 (2015). DOI: 10.1161/CIR.0000000000000350.

[48] M. Nichols et al. *European Cardiovascular Disease Statistics 2012*. Tech. rep. European Heart Network, Brussels, European Society of Cardiology, Sophia Antipolis, 2012.

[49] S.A. Niederer and N.P. Smith. "The Role of the FrankâĂŞStarling Law in the Transduction of Cellular Work to Whole Organ Pump Function: A Computational Modeling Analysis". In: *PLOS computational biology* (2009). DOI: 10.1371/journal.pcbi.1000371.

[50] S. Niroomandi et al. "Accounting for Large Deformations in real-Time Simulations of Soft Tissues Based on Reduced Order Models". In: *Computer Methods and Programs in Biomedicine* 105.1 (2012), pp. 1–12. DOI: http://dx.doi.org/10.1016/j.cmpb.2010.06.012.

[51] M.A. Obukhov. "Statistical description of continuous fields". In: *Transactions of the Geophysical International Academy Nauk USSR* 24 (1954), pp. 3–42.

[52] V.S. Pougachev. "General theory of the correlations of random functions". In: *Izvestiya Akademii Nauk USSR* 17 (1953), pp. 1401–1402.

[53] R. Rama, S.Skatulla, and C.Sansour. "Real-time modelling of the heart using the Proper Orthogonal Decomposition with Interpolation". In: *International Journal of Solids and Structures* (2015). In review.

[54] D. Rohmer, M.S.A. Sitek, and G.T. Gullberg. "Reconstruction and Visualization of Fiber and Laminar Structure in the Normal Human Heart from Ex Vivo Diffusion Tensor Magnetic Resonance Imaging (DTMRI) Data". In: *Investigative Radiology* 42.11 (2007), pp. 777–789. DOI: 10.1097/RLI.0b013e3181238330.

[55] S. Roweis. *Levenberg-marquardt optimization*. Notes, University Of Toronto. 1996.

[56] R. Ruotolo and C.J. Surace. "Using SVD to detect damage in structures with different operational conditions". In: *Journal of Sound and Vibration* 226 (1999), pp. 425–439.

[57] K Sack. "Biological tissue mechanics with fibres modelled as one dimensional Cosserat continua. Applications to cardiac tissue in healthy and diseased states." MA thesis. The University of Cape Town, 2014.

[58] M.S. Sacks. "Biaxial Mechanical Evaluation of Planar Biological Materials". In: *Journal of elasticity and the physical science of solids* 61.1 (2000), pp. 199–246.

[59] M.S. Sacks and A.P. Yoganathan. "Heart valve function: a biomechanical perspective". In: *Philosophical Transactions of the Royal Society of London B: Biological Sciences* 362.1484 (2007), pp. 1369–1391. DOI: 10.1098/rstb.2007.2122.

[60] J. Sandstede et al. "Age- and gender-specific differences in left and right ventricular cardiac function and mass determined by cine magnetic resonance imaging". In: *European Radiology* 10.3 (2000), pp. 438–442. DOI: 10.1007/s003300050072.

[61] L.A. Simmons, A.G. Gillin, and R.W. Jeremy. "Structural and functional changes in left ventricle during normotensive and preeclamptic pregnancy". In: *American Journal of Physiology - Heart and Circulatory Physiology* 283.4 (2002), H1627âĂŞH1633.

[62] L. Sirovich. "Turbulence and the dynamics of coherent structures. Part I: Coherent structures." In: *Quarterly of applied mathematics* 45.3 (1987), pp. 561–571.

[63] Lawrence Sirovich. "Analysis of turbulent flows by means of the empirical eigenfunctions". In: *Fluid Dynamics Research* 8.1âĂŞ4 (1991), pp. 85 –100. ISSN: 0169-5983. DOI: http://dx.doi.org/10.1016/0169-5983(91)90033-F. URL: http://www.sciencedirect.com/science/article/pii/016959839190033F.

[64] S. Skatulla. "Computational aspects of generalized continua based on moving least square approximations". PhD thesis. The University of Adelaide, 2006.

[65] S. Skatulla and C. Sansour. "Essential boundary conditions in meshfree methods via modified variational principle. Applications to shell computations." In: *Computer Assisted Mechanics and Engineering Sciences* 15.2 (2008), pp. 123–142.

[66] N.P. Smith et al. "Multiscale computational modelling of the heart". In: *Acta Numerica* 13.1 (2004), pp. 371–431. DOI: http://dx.doi.org/10.1017/S0962492904000200.

[67] G. Sommer et al. "Biomechanical properties and microstructure of human ventricular myocardium". In: *Acta Biomaterialia* (2015). DOI: http://dx.doi.org/10.1016/j.actbio.2015.06.031.

[68] Hawken S Commerford P Onen C Damasceno A Ounpuu S Yusuf S. Steyn K Sliwa K. "Risk Factors Associated With Myocardial Infarction in Africa: The INTERHEART Africa Study". In: *Circulation* 112.23 (2005).

[69] P. Stolzmann et al. "Left Ventricular and Left Atrial Dimensions and Volumes Comparison Between Dual-Source CT and Echocardiography". In: *Investigative Radiology* 43.5 (2008), 284 âĂŞ289. DOI: 10.1097/RLI.0b013e3181626853.

[70] W. Sun et al. "Biaxial mechanical response of bioprosthetic heart valve biomaterials to high in-plane shear." In: *Journal of Biomechanical Engineering* 125.3 (2003), pp. 372–380.

[71] B.T. Tan, K. Willcox, and M. Damodaran. *Applications of proper orthogonal decomposition for inviscid transonic aerodynamics*. Tech. rep. Singapore-MIT Alliance, 2003. URL: http://dspace.mit.edu/bitstream/handle/1721.1/3694/HPCES002.pdf?sequence=2.

[72] M.K. Transtrum and J.P. Sethna. "Improvements to the Levenberg-Marquardt algorithm for nonlinear least-squares minimization". In: *ArXiv e-prints* (2012). URL: http://arxiv.org/abs/1201.5885.

[73] D. Tsegay and A. Mebrahtu. "Multidimensional and Multi-Parameter Fortran-Based Curve Fitting Tools". In: *Daniel & Alem (MEJS)* 1.1 (2009), pp. 95–112.

[74] T.P. Usyk, I.J. LeGrice, and A.D. McCulloch. "Computational model of three-dimensional cardiac electromechanics". In: *Computing and Visualization in Science* 4.4 (2002), pp. 249–257. DOI: 10.1007/s00791-002-0081-9.

[75] T.P. Usyk and A.D. McCulloch. *Computational methods for soft tissue biomechanics*. 2002. URL: http://cmrg.ucsd.edu/Continuity/Documentation/Theory?action=AttachFile&do=get&target=Usyk2003.pdf.

[76] Gerhard Venter. "Review of Optimization Techniques". In: *Encyclopedia of Aerospace Engineering*. John Wiley & Sons, Ltd, 2010. ISBN: 9780470686652. DOI: 10.1002/9780470686652.eae495. URL: http://dx.doi.org/10.1002/9780470686652.eae495.

[77] Jonathan F Wenk et al. "A method for automatically optimizing medical devices for treating heart failure: designing polymeric injection patterns". In: *Journal of biomechanical engineering* 131.12 (2009), pp. 121011–121011–7.

[78] J. Wong and E. Kuhl. "Generating fibre orientation maps in human heart models using poisson interpolation." In: *Computer Methods in* 17.11 (2014), pp. 1217–1226.

[79] P. Wriggers. *Nonlinear finite element methods*. Springer Science, 2008.

[80] C.G. Wu et al. "A note on equivalence of proper orthogonal decomposition methods". In: *Journal of Sound and Vibration* 265 (2003), pp. 1103–1110. DOI: 10.1016/S0022-460X(03)00032-4.

[81] Z.C. Xia and J.W. Hutchinson. "Crack tip fields in strain gradient plasticity". In: *Journal of the Mechanics and Physics of Solids* 44.10 (1996), pp. 1621–1648. DOI: 10.1016/0022-5096(96)00035-X.

[82] S.F. Yiu et al. "Determinants of the Degree of Functional Mitral Regurgitation in Patients With Systolic Left Ventricular Dysfunction: A Quantitative Clinical Study". In: *Circulation* 102.12 (2000), pp. 1400–1406. DOI: 10.1161/01.CIR.102.12.1400.